博士論文

Studies of atmospheric waves on Venus using continuous cloud images (連続雲画像解析による金星の大気波動の研究)

奈良　佑亮

要旨

金星は地球と似た大きさ、質量を持つ惑星だが大気環境は大きく異なっている。金星の高度 70 km 付近ではスーパーローテーションと呼ばれる最大で 100 m s^{-1} を超える西向きの風が常に全球的に吹いており、いまだその形成メカニズムは解明されていない。大気を持つ地球型惑星では金星のように自転に対して速い循環と地球のように遅い循環する大気に大別することができ、それぞれの大気の性質を明らかにし、惑星という枠組みの中における地球の位置づけを知ることで、地球の理解をさらに深めることができる。

大気中を伝播する波動は運動量輸送を伴い、大気の加速減速に寄与するため、スーパーローテーションの形成メカニズムの候補として挙げられており、大気波動の性質を明らかにすることは大気循環の理解につながる。本論文では金星における大気波動の役割を明らかにするため、大気波動と平均風による紫外画像における惑星規模模様の形成過程、大気波動による中層大気と上層大気の結合、新規雲追跡手法による惑星規模波動の全球的な運動量輸送に関する研究を行った。

金星は全球を厚さ 20 km 以上の雲に覆われており、太陽光の約 8 割がこの雲によって反射される。雲頂高度にあたる高度約 70 km で紫外から可視波長域にかけて広く強い吸収があり、金星の高度約 70km における太陽散乱光を捉える紫外画像には空間的に不均一な吸収があることが知られていて、3 割程度のコントラストがある。このため太陽光による大気加熱の分布に大きな影響を与えていると考えられる。この紫外画像のコントラストには特徴的な空間構造があり、アルファベットの Y を横倒しにしたような惑星規模の模様が変動性を持って頻繁に現れることが知られているが、そういった雲の模様の形成過程は未解明である。第二章では欧州の金星探査機ヴィーナスエクスプレスに搭載されていた撮像装置 VMC の紫外画像を用いて、金星の紫外画像で観察される惑星規模の模様とその高度における風速場を比較し、模様の形成メカニズムを考察した。2007 年 7 月から 8 月の惑星規模の模様が顕著に観察される時期に紫外画像の輝度変化と風速変動を周期解析することで、赤道域に約 4 日、中緯度に約 5 日の周期性が検出され、それぞれケルビン波、ロスビー波と呼ばれる惑星規模の大気波動に起因することが分かった。解析結果から以下のような、惑星規模波動による惑星規模の模様の形成過程に関する仮説を立てた。紫外線を吸

収する物質は雲頂より下層に多く存在すると考えられており、赤道域で上方への物質輸送を担うケルビン波によって雲頂付近へ輸送される。そして、極向きの平均風と水平面内を振動するロスビー波の極向きの流れによって暗い物質が極向きに輸送され、高緯度において、高緯度ほど角速度の大きくなる西向きの風により暗い物質が東西に引き延ばされ、筋模様を形成するというものである。数値計算により、現実的な平均風と大気波動が存在する状況で吸収物質を模擬した受動的な物体を移流させることで、模様の形成仮説の検証を行ったところ、形成された模様とその時間発展が観測される模様に類似することが確かめられた。

第三章では、大気波動による雲層高度と上層大気の結合に関する研究を 2017 年 6 月に金星探査機あかつきと宇宙望遠鏡ひさきが同時に金星の朝側を観測した時のデータセットを用いて行った。用いたデータはあかつきに搭載されている撮像装置 UVI の紫外画像と、ひさきに搭載されている極端紫外線分光撮像装置 EXCEED の分光データで、あかつきの紫外画像から推定した高度約 70 km の風速場とひさきが捉えた高度約 130 km 以上の酸素原子のコラム密度を反映する酸素原子の発光強度の比較をした。その結果、両者に共通する 3.6 日周期の変動が検出され、高度 70 km の変動は惑星規模の大気波動のケルビン波であることが変動の空間構造や平均風との比較で示唆された。大気波動と熱圏の変動の関連を調べるため、1 次元の線形波動の鉛直伝播を数値計算によって解いたところ、ケルビン波は放射減衰により熱圏まで鉛直伝播できないことが示された。また、このモデルにより、水平波長が 1000 km 程度の小さいスケールの重力波は朝側で熱圏まで伝播でき、夕側では熱圏まで伝播するまでに減衰してしまうことが分かった。朝夕の非対称性は熱圏における背景風速が朝側と夕側で異なっていることに起因する。高度 70 km のケルビン波による風速や温度場の振動が小さいスケールの重力波の伝搬性を変調させることにより、熱圏への伝播が周期的に起こり発光強度の変動を引き起こしていると考えられる。次に、熱圏の大気波動によって引き起こされる乱流や大規模な循環に対する大気発光強度の応答を調べ、以上の仮説を検証するため 1 次元の光化学モデルを構築した。酸素原子の主要な生成消滅過程である二酸化炭素の光解離による生成、酸素原子の再結合による消滅を考慮し、酸素原子密度の時間発展を解いた。その結果、大気波動の砕波により周期的に変動する拡散係数の振幅が約 300 $m^2\ s^{-1}$ の時、観測された熱圏の発光強度の変動を説明できることが示された。

第四章では、金星の紫外画像の高緯度に頻繁に観察されるような筋模様が卓越する領域において信頼性のある雲追跡手法を開発した。画像内に筋模様が存在すると、筋模様の向きに沿った変位がわからないため、従来は雲追跡が困難であった。画像内の筋模様は筋に沿った明るさの変化が小さいため、筋模様に沿った向きに画像を微分することで明るさの変化の小さい筋模様を低減させることでこの問題を解決した。この手法をあかつきの紫外画像に適用し風速場の推定を行い、得られた風速場の時系列データに周期解析を適用することで、2017 年 7 月に赤道域の東西風、中緯度の南北風に 4.9 日の周期性が検出された。検出された 4.9 日周期の変動の空間構造を再現したところ、金星に存在すると考えられている惑星規模波動であるロスビー波と整合し、赤道向きにスーパーローテーションを加速させる向きの運動量輸送を伴うことが分かった。提案手法により初めて金星におけるロスビー波の全体像が捉えられ、スーパーローテーションの加速に寄与していることが分かった。

Table of Contents

Chapter 1: General introduction

The atmospheric environment of Venus is quite different from that of Earth, although the mass and the size are similar. Venus has a dense atmosphere composed mainly of CO_2 (96%) and because of its greenhouse effect, the surface temperature reaches 730 K. Venus is covered with clouds at altitudes between 40 to 70 km and the clouds reflect ~80% of sunlight to space. Figure 1 shows the wavelength dependence of the sunlight reflectivity on Venus. Broad and strong absorption occurs in the ultraviolet wavelengths. Figure 2 shows an ultraviolet image taken by Venus orbiter Akatsuki, whose contrast reflects the spatial distributions of unidentified ultraviolet absorbers at the cloud top altitude of ~70 km. Because the UV absorption is inhomogeneous and has a contrast of ~30% across the disk, it determines the spatial distributions of solar heating. In UV images, various patterns are seen and one of the significant features is the dark horizontal Y feature (e.g. Rossow et al., 1980), which often shows equatorially-symmetric dark pattern with a zonal wavenumber of unity accompanying tilted dark mid-latitude bands extending from the equator to high latitudes and a dark equatorial band at the root of the Y (Figure 3). Though the Y feature is frequently observed with some variability in the structure, its generation mechanism has been unclear. The formation of this planetary-scale feature will be studied in Chapter 2.

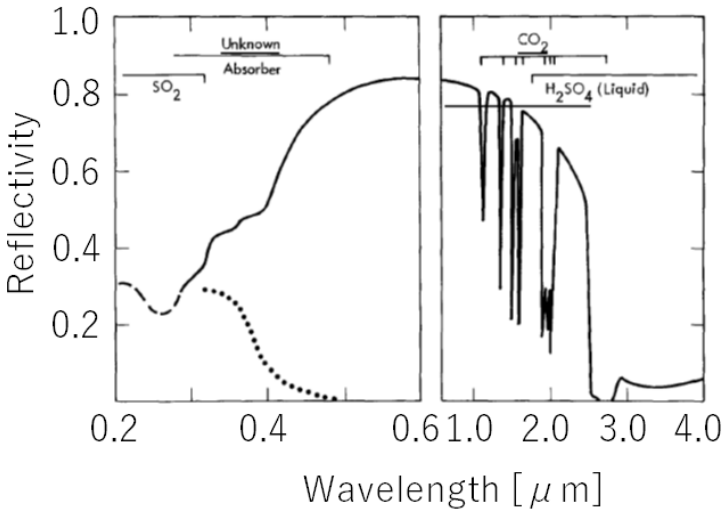

Figure 1. Wavelength dependence of sunlight reflectivity of Venus (Moroz et al., 1985).

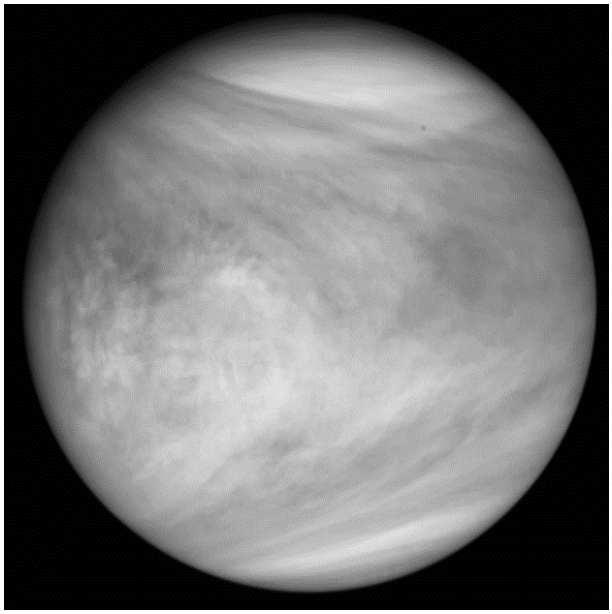

Figure 2. An image of Venus taken by 365-nm channel of Ultraviolet Imager (UVI) on board Akatsuki spacecraft.

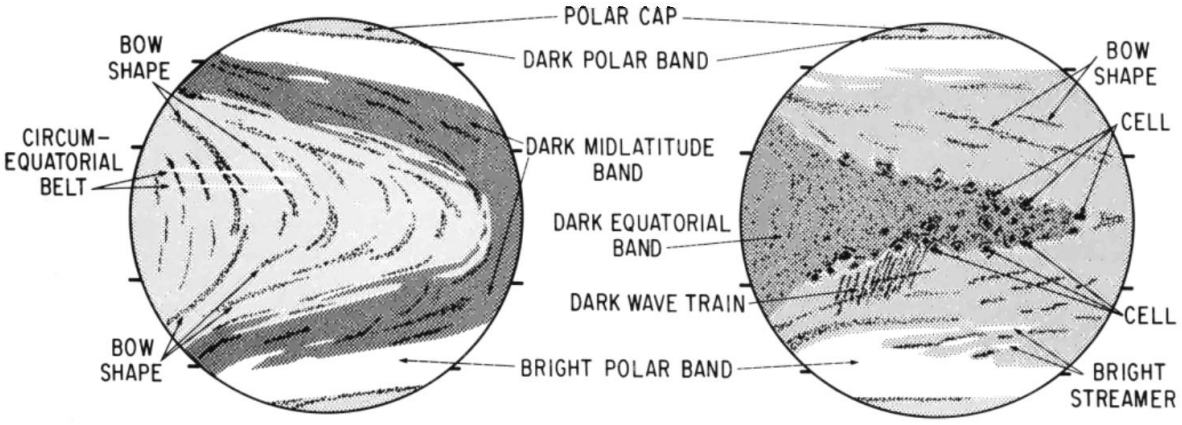

Figure 3. A schematic view of cloud features seen in Venusian UV images (Rossow et al., 1980).

Figure 4 shows the vertical profile of the zonal wind of Venus. The westward wind speed increase with height from 0 m s^{-1} at the surface to ~100 m s^{-1} at ~70 km altitude. This westward wind blows almost everywhere and is ~60 times faster than the planetary rotation. This atmospheric circulation is called superrotation. The mechanism of the generation and the maintenance of the superrotation is still unclear. Lee

et al. (2019) discovered the anti-correlation between UV planetary albedo and the zonal wind speed with long term data analysis; when the planetary albedo is lower, the westward zonal velocity tends to be faster. The lower planetary albedo leads to stronger solar heating, implying the solar heating may play an important role in the acceleration of superrotation. To reveal the mechanism of the superrotation, the relationship between the planetary albedo and the wind velocity should be understood and the close comparison between them should be conducted.

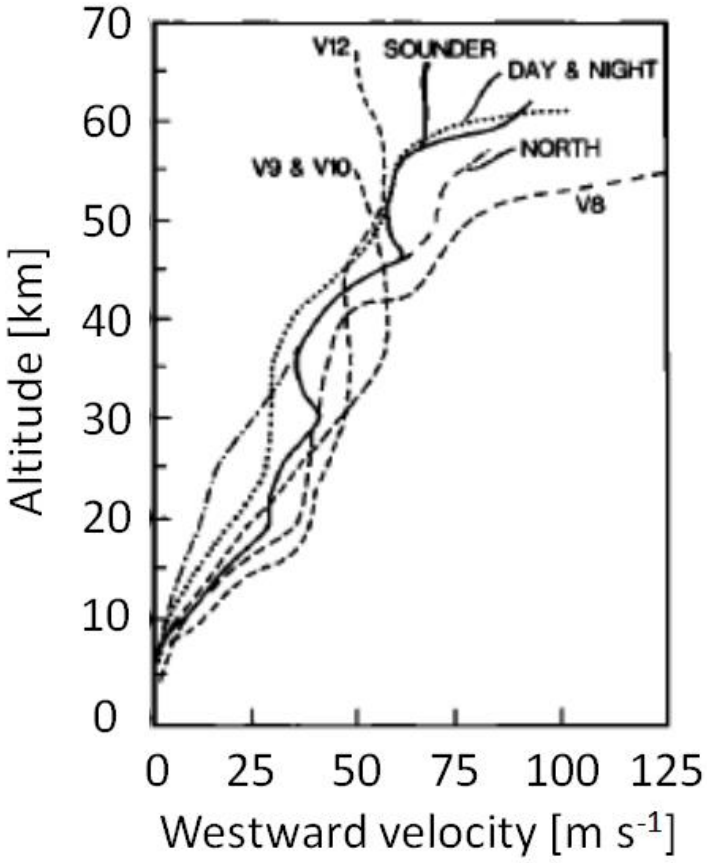

Figure 4. Vertical profiles of zonal wind speed measured directly by sounding probes of Venera missions and Pioneer Venus mission (Schubert et al., 1980).

Among the solar system, Venus, Earth, Mars, and Titan, which is one of satellites of Saturn, have rocky surfaces and atmospheres. Titan's atmosphere is also superrotating like Venus and the atmospheric circulation of Mars' is moderate like Earth as shown in Figure 5 (Dias Pinto & Mitchell, 2014). The tendency that the atmosphere is superrotating when the planetary rotation is slow can be found. In addition to the zonal circulation, a meridional circulation is formed by the meridional temperature gradient. As for the planets

with fast planetary rotation, the meridional circulation cannot reach the high latitude because of the Coriolis force.

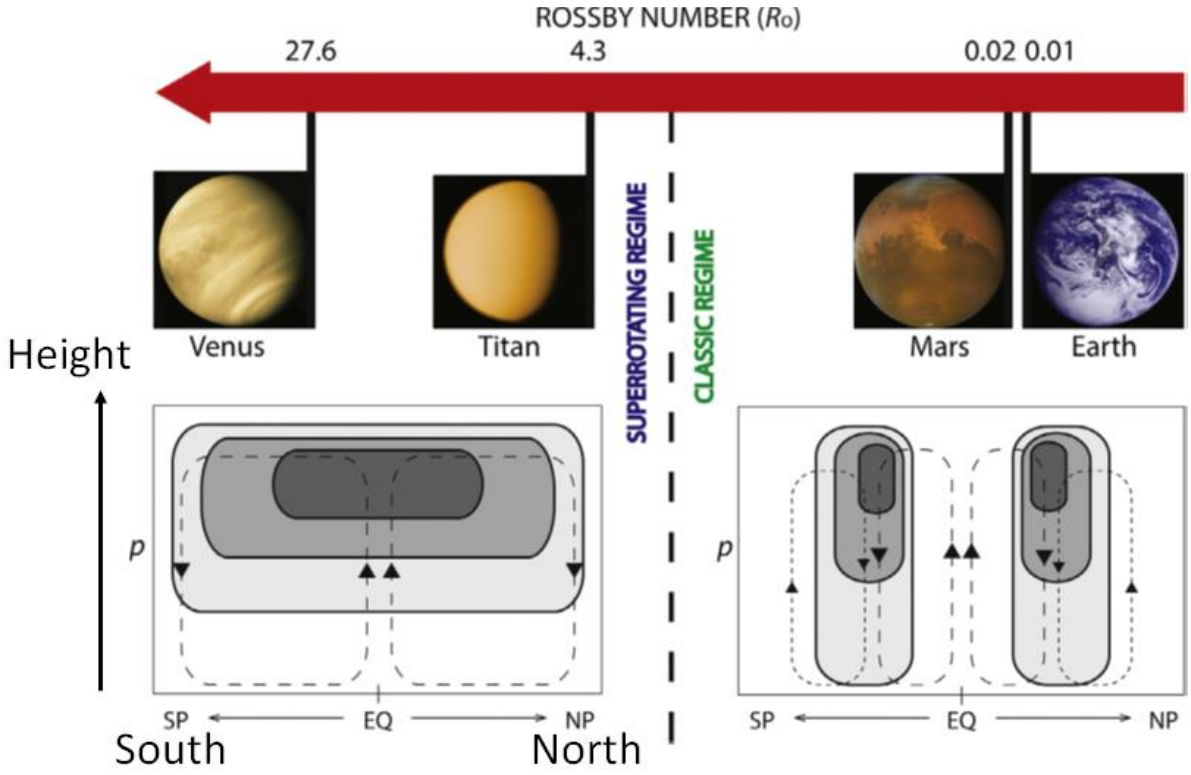

Figure 5. Schematic view of atmospheric circulations with different Rossby numbers (Dias Pinto & Mitchell, 2014). Rossby number ($R_o = U/2\Omega a$) is proportional to a typical horizontal wind velocity U to planetary rotation speed, where Ω is the planetary rotation rate and a the planetary radius.

On the planets with slow planetary rotation, meridional rotation can reach high latitudes. Because the distance between the atmosphere and the rotation axis is shorter in higher latitudes, the angular velocity of the air parcel transported to the high latitudes becomes faster and then mid-latitude jets are formed. Because the jets are dynamically unstable, the instabilities glow and atmospheric waves can be excited. It is thought that such atmospheric waves transport momentum equatorward and contribute to the acceleration of the atmosphere, forming the superrotation (e.g., Gierasch, 1975). However, this kind of instabilities and the atmospheric waves that transport momentum equatorward are yet to be observed. Atmospheric waves propagate in the atmosphere and buoyancy and/or meridional gradient of Coriolis force act as their restoring force.

Figure 6 shows the periodograms of wind velocities at ~70 km altitude obtained from the continuous UV images of Venus obtained by the Venus Monitoring Camera (VMC) onboard ESA's spacecraft Venus Express in different two seasons (Kouyama et al., 2015). In Figure 6a, significant periodicity of 4 days, which is shorter than the rotation period of the mean zonal velocity, was detected. By comparing with theoretical wave modes, this variation was identified as an equatorially trapped Kelvin wave which has an oscillation of the zonal wind as shown in Figure 7a. As shown in Figure 6b, the same periodicity was detected in the equatorial zonal velocity and mid-latitudinal meridional velocity, with a phase velocity slower than the background zonal wind speed. This variation was also identified as a Rossby wave which has a vortex structure as shown in Figure 7b.

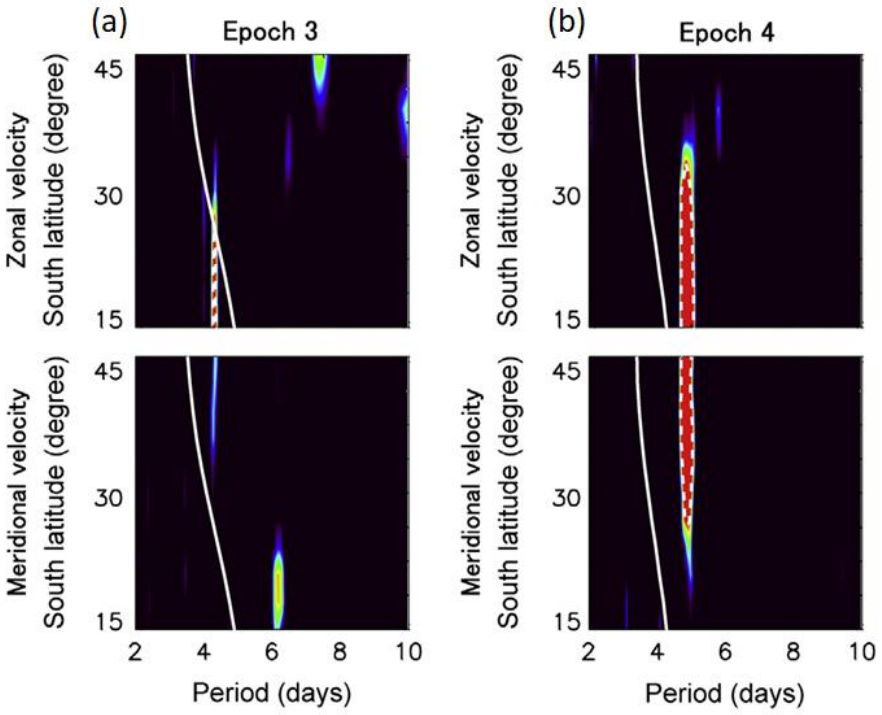

Figure 6. Periodograms of wind velocities (Kouyama et al., 2015). White curves indicate the rotation period corresponding to the mean zonal velocity. White dashed contour represents the 90% statistically significant level.

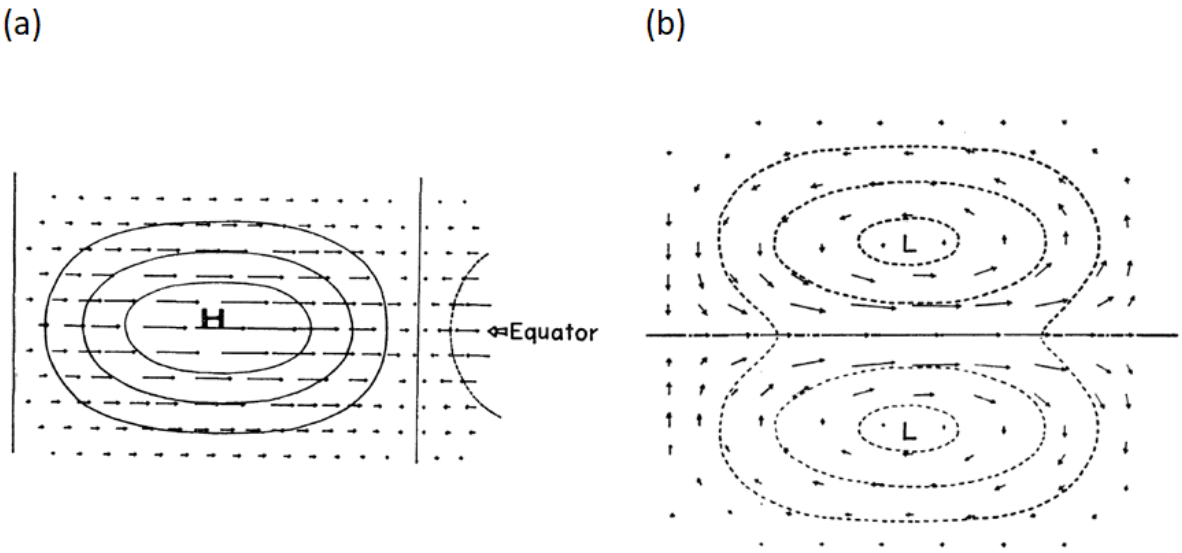

Figure 7. Solutions of planetary-scale wave modes from linear wave theory (Matsuno, 1966). (a) Kelvin wave and (b) hemispherically-symmetric Rossby wave.

Above 70 km altitudes, the superrotation becomes weak with increasing altitude and the circulation directing from the sub-solar point to the anti-solar point becomes dominant in the thermosphere above 100 km altitude because of the large temperature gradient associated with the long Venusian solar day of ~117 Earth days: the wind flows westward on the dawn side and eastward on the dusk side as shown in Figure 8 (Alexander, 1992). Mayr et al. (1985) pointed out that the sub-solar to anti-solar flow would exceed 300 m s^{-1} at the maximum in the absence of drag. On the other hand, ground-based Doppler wind measurements using sub-millimeter CO absorption lines showed that the thermospheric wind velocity is ~200 m s^{-1} with significant variability (Clancy el al., 2012); it is believed that breaking of gravity waves generated in the lower atmosphere reach the thermosphere and effectively decelerate the thermospheric wind to the observed values. Gravity waves have been observed at the cloud top and in the middle atmosphere above clouds (e.g., Sánchez-Lavega et al., 2017) but there is no evidence that gravity waves propagate from the lower atmosphere to the thermosphere. The interaction between these two altitude regions will be investigated in Chapter 3.

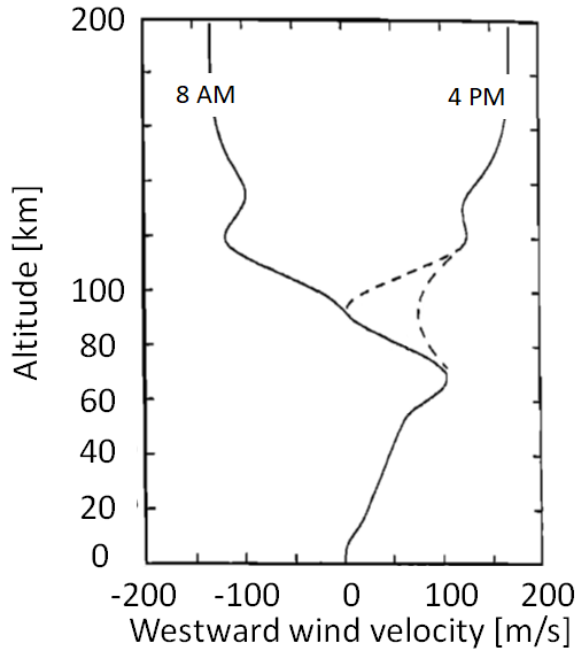

Figure 8. Vertical profile of zonal wind speed (Alexander, 1992).

To estimate wind fields, cloud tracking has been widely used. By calculating cross-correlation between small areas of images obtained successively, the displacement within the time interval is estimated. Figure 9c shows an example of the cross-correlation surface obtained from a pair of images with a time interval of 2 hours (Figure 9a, b). The template is a small area in the first image where the velocity is estimated. The search region is an area in the second image where displacements of the template is searched. The point of maximum correlation is regarded as the displacement of the cloud feature. However, cloud tracking has been difficult in the high latitude of Venus because streak features are dominant in these regions (Figure 2). Figure 10 shows a schematic view of the motion of a streak; the displacement along the streak features cannot be identified. The difficulty prevents examination of the possible mechanisms of the superrotation. The development of a new cloud tracking method which can be applied to the high latitude of Venus UV images will be described in Chapter 4.

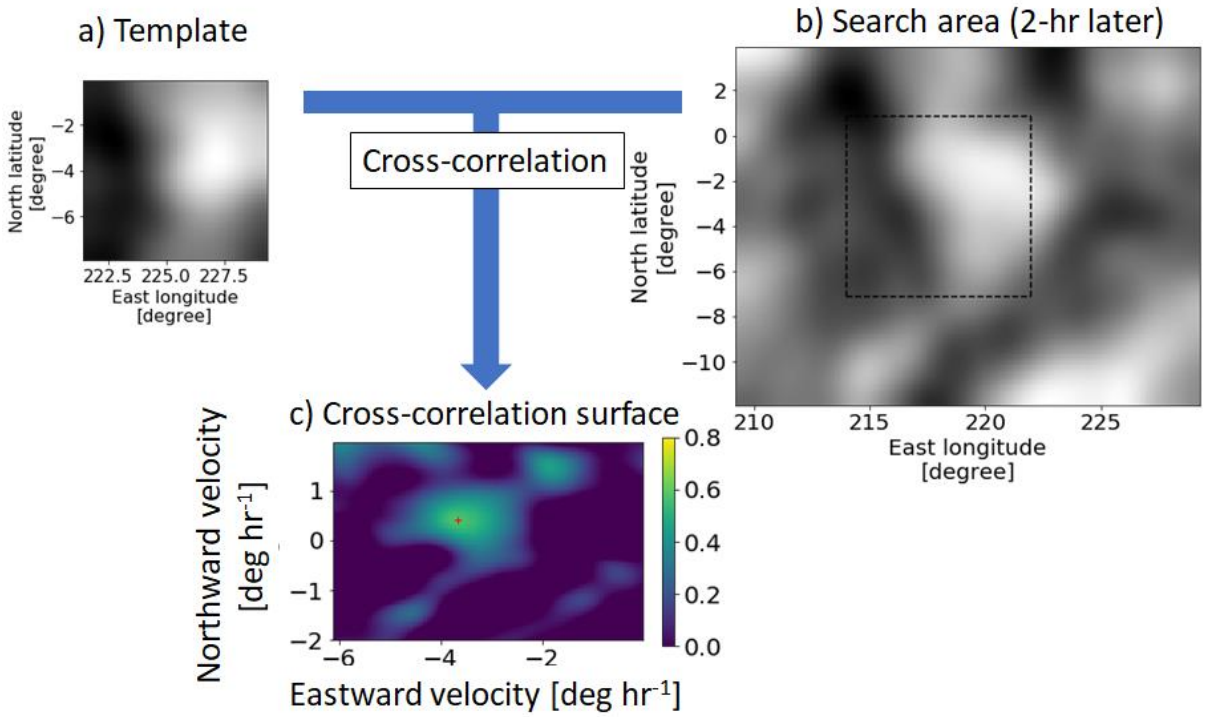

Figure 9. An example of cross-correlation method. (c) Cross-correlation surface is obtained by calculating cross-correlation between (a) the template and (b) the search region. The red cross indicates the point of the maximum correlation and the dashed square is the area where the template is most likely to be displaced.

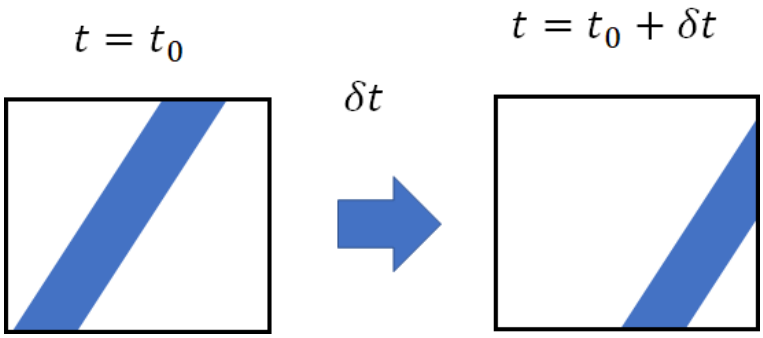

Figure 10. A schematic view of the displacement of streak features within the time interval of δt.

This thesis consists of three studies on the roles of the atmospheric waves in the Venusian atmosphere. A formation mechanism of the planetary-scale cloud pattern by planetary-scale atmospheric waves and the mean circulation is discussed in Chapter 2, dynamical links between the cloud-level atmosphere and the thermosphere by atmospheric waves are investigated in Chapter 3, and a new cloud tracking method which

can be applied to streaky cloud patterns like these seen in the high latitude of Venus is developed, and horizontal structures of planetary-scale waves are described in Chapter 4. Chapter 5 gives conclusions.

Chapter 2: Formation of the Y feature at the Venusian cloud top by planetary-scale waves and the mean circulation

2.1. Introduction

Ultraviolet (UV) images of Venusian cloud top exhibit various planetary-scale features because of the presence of unidentified UV absorbers (Mills et al., 2007; Moroz et al., 1985). One of the significant features is the dark horizontal Y feature (e.g. Rossow et al., 1980), which often shows equatorially-symmetric dark pattern with a zonal wavenumber of unity accompanying tilted dark mid-latitude bands extending from the equator to high latitudes and a dark equatorial band at the root of the Y. Though the Y feature is frequently observed with some variability in the structure, its generation mechanism has been unclear for more than 40 years since its discovery (Boyer & Guérin, 1969). The phase-angle dependence of the UV contrast suggests that the absorbers are deep in the cloud (Esposito, 1980) and the tendency of decreased albedo near the subsolar suggests the supply of absorbers by upwelling or the evaporation of the upper haze (Titov et al., 2012). Therefore, the formation of the Y feature should be strongly related to the transport of materials absorbing sunlight, and thus its understanding would provide clues to the mechanism determining the planetary albedo and the solar heating in the cloud layer.

Smith & Gierasch (1996) argued that the horizontal stretching and advection of cloud parcels by the combination of the mean zonal wind, Hadley circulation and thermal tides produce streak structures and that thermal tides are responsible for the local time dependence of the streak orientation. Though their model

seems to explain the characteristics of small-scale streaks, the formation process of the tilted dark bands composing the Y feature is not addressed.

Del Genio & Rossow (1990) showed that the propagation of the equatorial UV contrast with a zonal wavenumber of unity tends to be faster than the mean zonal velocity based on the analysis of the cloud-tracked wind speed and the periodicity of the brightness, although the faster propagation than the mean flow is not very clear due to the large dispersion of cloud-tracked velocities. This suggests that planetary-scale waves propagating relative to the background wind are responsible for the Y feature. Analysis of wind fields deduced by cloud tracking indeed showed existence of planetary-scale waves that are interpreted as Kelvin waves, Rossby waves, and thermal tides (Kouyama et al., 2015; Kouyama et al., 2013; Limaye, 1988; Limaye & Suomi, 1977; Rossow et al., 1990). Covey & Schubert (1981) and Smith et al. (1993) argued that the Kelvin wave might be a preferred global mode of the Venus atmosphere and can be generated by random forcing somewhere below the cloud top. Covey & Schubert (1981) and Yamamoto & Tanaka (1997) suggested that the superposition of a Kelvin wave and a hemispherically-symmetric Rossby wave can explain the Y feature, although the mechanism of the transport of UV absorber along the tilted dark bands is not studied. Sugimoto et al. (2014) pointed out that the observed hemispherically-symmetric Rossby waves could be explained by baroclinic waves generated at cloud heights and that their horizontal structures are reminiscent of the Y feature. Peralta et al. (2015) argued that the Y feature could be produced by the vertical transport of absorbers by a Kelvin wave distorted in the sheared flow and the subsequent zonal advection by the background wind; since the zonal advection continues to distort the pattern, the mechanism for the long-lasting feature needs to be studied.

To understand the role of spatially and temporally varying winds in the formation of the Y feature, comparison between the cloud morphology and the wind field is essential. Patsaeva et al. (2015) studied the relationship between the cloud motion vectors and the cloud morphology using Venus Express Venus Monitoring Camera (VMC) images and suggested that the deflection of the wind orientation from latitude circles in the mid-latitude depends on the presence of dark streaks. However, the mechanism of the formation of dark streaks and the cause of the varying mid-latitude wind field are still unclear.

In this study, I analyze the relationship between the periodical variations of the cloud-top wind field and the planetary-scale UV pattern to propose a new hypothesis about the formation of the Y feature, in which advection of the absorbing material by planetary-scale waves plays an important role. The data used are the

cloud images taken by VMC on ESA's Venus Express spacecraft, which accumulated a great number of images during its 8 years of observation (Markiewicz, Titov, Limaye, et al., 2007; Svedhem et al., 2007). Section 2.2 describes the data set, Section 2.3 gives the details of the analysis procedures, Section 2.4 shows the results, Section 2.5 discusses the generation mechanism of the planetary-scale streak feature, and Section 2.6 presents a simple numerical simulation which demonstrates the transport of an unidentified absorber leading to a Y feature-like pattern. Section 2.7 gives conclusions.

2.2. Dataset

UV images obtained by VMC on Venus Express were used in this study. Venus Express observed Venus from April 2006 until December 2014 in a polar orbit having a period of 24 hours, the apocenter located at 66,000 km altitude above the South pole, and the pericenter located at 250-400 km altitudes above the North pole. Among the four wavelength channels of VMC with the center wavelengths of 365, 513, 965 and 1010 nm, I analyzed the 365 nm channel, in which absorption by unidentified materials dominates (Moroz et al., 1985). The pixel format of the CCD detector is 512 × 512 pixels and the field of view is 17.5° × 17.5°. Images that contain the entire Venus disk were used in this study; such images were acquired when the spacecraft altitude was higher than about 30,000 km, and mostly the southern hemisphere were covered from such high altitudes because of the orbit shape. The pixel resolution of the images analyzed in this study ranges between 30 km and 50 km at the sub-spacecraft point. The details of Venus Express are given in Svedhem et al. (2007) and the specifications of VMC are given in Markiewicz et al. (2007).

Before analysis, the original image data are processed with the procedure described in the next section, and then projected onto longitude-latitude maps. Radiance values are given on the dayside only. During the projection the pointing direction is corrected by a limb fitting method proposed by Ogohara et al. (2012) and the optical distortion is corrected by the method of Kouyama, Yamazaki et al. (2013), although Limaye et al. (2015) proposed another image correction scheme. The grid interval of the longitude-latitude maps is 0.25° both in latitude and longitude. The details of the overall data processing pipeline are given in Ogohara et al. (2017). The data I used were obtained in orbits 436-490 (July 1, 2007-August 23, 2007), 659-710 (February 8, 2008-March 30, 2008) and 883-938 (September 19, 2008-November 14, 2008).

2.3. Analysis method

2.3.1. Photometric correction and noise reduction

To observe variations of the UV reflectivity, I first applied Minnaert's law, which relates the observed brightness I and the brightness at zero incident angle and zero emission angle I_0, as

$$I = I_0 \cdot \mu^{k-1}\mu_0^k, \tag{1}$$

where μ is the cosine of the emission angle and μ_0 is the cosine of the incidence angle (Minnaert, 1941). This photometric correction has been widely used for images of the planets covered with thick clouds including Venus (Lee et al., 2015; Titov et al., 2012). The parameter k was estimated by fitting pairs of $\ln(\mu\mu_0)$ and $\ln(\mu I)$ in each image to a linear function; the slope of the fitted line gives k. Since fitting becomes worse for emission or incidence angles near 90°, I restricted the analysis to regions where both the emission and the incidence angles are less than 80°. An example of the photometric correction is shown in Figure 1.

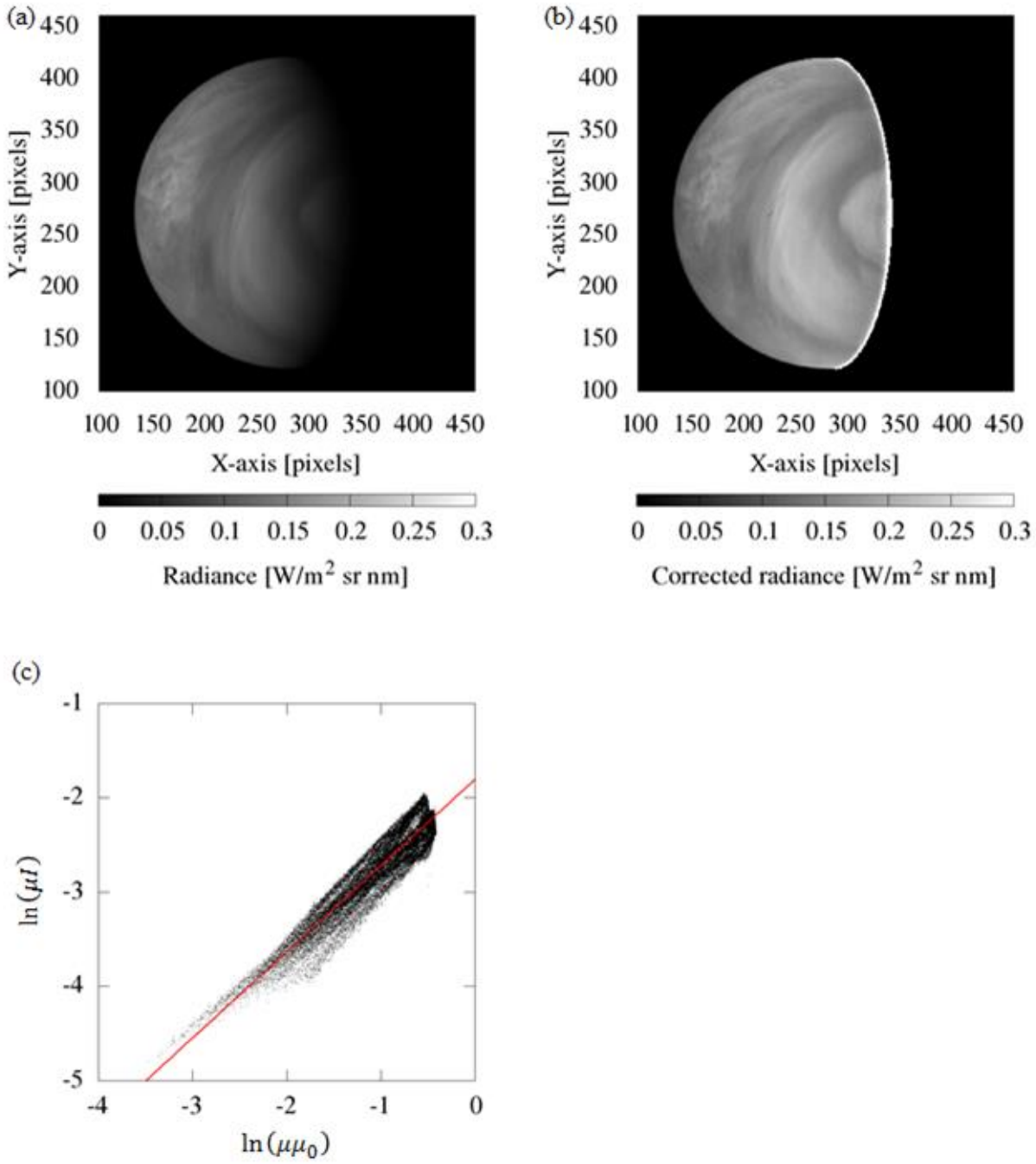

Figure 1. An example of photometric correction using Minnaert's law. (a) Original image, (b) corrected image, and (c) scatter plot of ln($\mu\mu_0$) and ln(μI). The data was taken from orbit 458. In (c), the red line shows the result of fitting; the slope of this line gives k.

The images contain streaky noise along one dimension of the detector, which is created during charge transfer in the CCD as reported in VMC Calibration Report (VMC-MPAE-RP-SS011-001, 2008). For images to be used for cloud tracking, the streaky noise was reduced by differentiating the brightness along the axis

of the charge transfer. This procedure at the same time enhances small-scale cloud patterns. Then, the entire area in each image was smoothed by a 5 × 5-pixels moving average to suppress high-frequency noises emphasized by the differentiation. After these corrections the images were projected onto the longitude-latitude coordinate.

2.3.2. Cloud tracking

To deduce velocity fields, I used a cloud tracking method based on cross correlation as given below. First, a pair of images observed at different times is prepared. A square area with a particular dimension called a template is selected in the first image. By assuming possible maximum displacements along the longitude and the latitude during the time interval between the two images, an area called a search region is determined. Then, the correlations between the template and areas with the size same as the template in the search region are calculated, composing a cross-correlation surface. The point of maximum correlation in the cross-correlation surface is regarded as the location to which the air parcel was displaced during the time interval. In this study, the size of the template was set to 10° × 10° and the search region was determined by assuming that the westward velocity is between 0 and 150 m s^{-1} and the northward velocity is between -50 and 50 m s^{-1}. Kouyama, Imamura, et al. (2013) systematically investigated the template size dependence of cloud-tracked velocities using VMC dataset. The zonal velocities deduced from template sizes of 2-10 degrees do not show significant differences while the standard deviation becomes larger and the correlation coefficients tend to be lower for smaller template sizes. I have deduced velocities every 5° in both longitude and latitude.

To reduce erroneous determinations of the displacement caused by multiple peaks that frequently appear in cross-correlation surfaces, I have applied the method of averaging cross-correlation surfaces proposed by Ikegawa & Horinouchi (2016). In this method, three or more images are prepared, and cross-correlation surfaces between multiple combinations with different time intervals are calculated and averaged on the coordinates of the longitudinal and latitudinal velocities. In this study, three images obtained sequentially were used to prepare two pairs of images; one pair is composed of the first image and the second image, and the other is composed of the first image and the third image.

Correlation surfaces sometimes have elongated peaks due to streak features and/or rather featureless structures. To exclude velocity vectors obtained from such correlation surfaces, I adopted the following criteria for acceptable vectors: on the cross-correlation surface, a sub-region of 1° × 1° size in longitude and

latitude is placed centered at the correlation peak, and the fractional area in the sub-region where the difference in the correlation coefficient from the peak value is less than 0.05 is evaluated; the fractional area should be smaller than 80%.

2.4. Results

2.4.1. Periodicities in the radiance

Figure 2a shows the temporal variation of the radiance after photometric correction at 10°S averaged for the local solar time of 11:00-13:00 during orbits 436-490. Figure 2b shows its periodogram obtained by Lomb-Scargle method (Scargle, 1982), which can be applied to unevenly sampled data. Periodicities of 4 and 5 Earth days, exceeding the statistical significance of 99%, are identified. Figure 3 shows the latitudinal profiles of the Lomb-Scargle periodogram obtained for three different periods; the first period, orbits 436-490, shows the most coherent periodicity of ~4 Earth days from the equator to mid-latitudes. The second period, orbits 659-710, shows a distinct periodicity of ~5 Earth days in the middle latitude and weak periodicities of ~4 Earth days near the equator. The third period, orbits 883-938, exhibits a periodicity of ~4.5 Earth days in the low latitude and marginally significant periodicities over wide frequencies. Though Lomb-Scargle periodograms can be contaminated by erroneous peaks caused by periodical data gaps (e.g., Kouyama, Imamura, et al., 2013), the dataset used in this study does not have such data gaps, and thus the obtained periodograms should be free from such erroneous peaks. Figure 4 shows examples of the mosaic images created from data obtained every 24 hours for the three periods. The longitudinal shifts between images are determined by the background flow velocity on the equator obtained by cloud tracking later in Section 2.4.2. I consider that the period of orbits 436-490 shows the most coherent periodicity and the most distinct, tilted dark band representative of the Y feature; I focus on this period in later analysis.

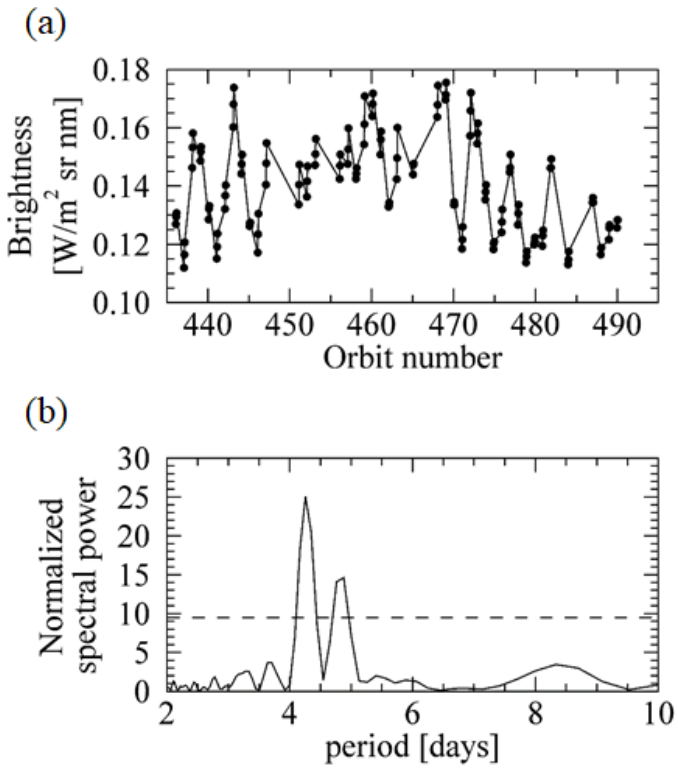

Figure 2. (a) Temporal variation of the radiance at 10°S averaged over the local solar time of 11:00-13:00. (b) Lomb-Scargle periodogram of the variation of the radiance. The dashed line shows the 99% statistically significant level.

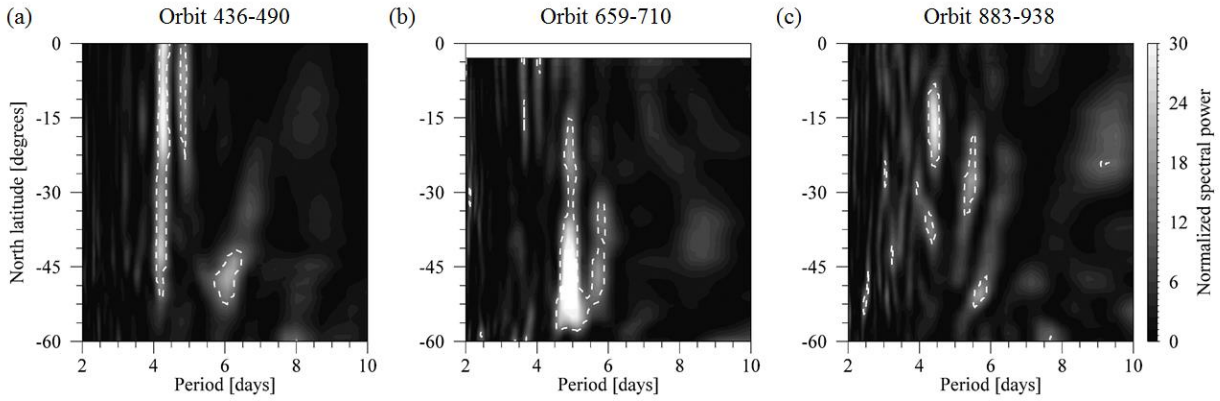

Figure 3. Latitudinal profiles of the Lomb-Scargle periodogram of the radiance for different periods. (a) Orbits 436-490, (b) orbits 659-710, and (c) orbits 883-938. Dashed contours show the 99% statistically significant level.

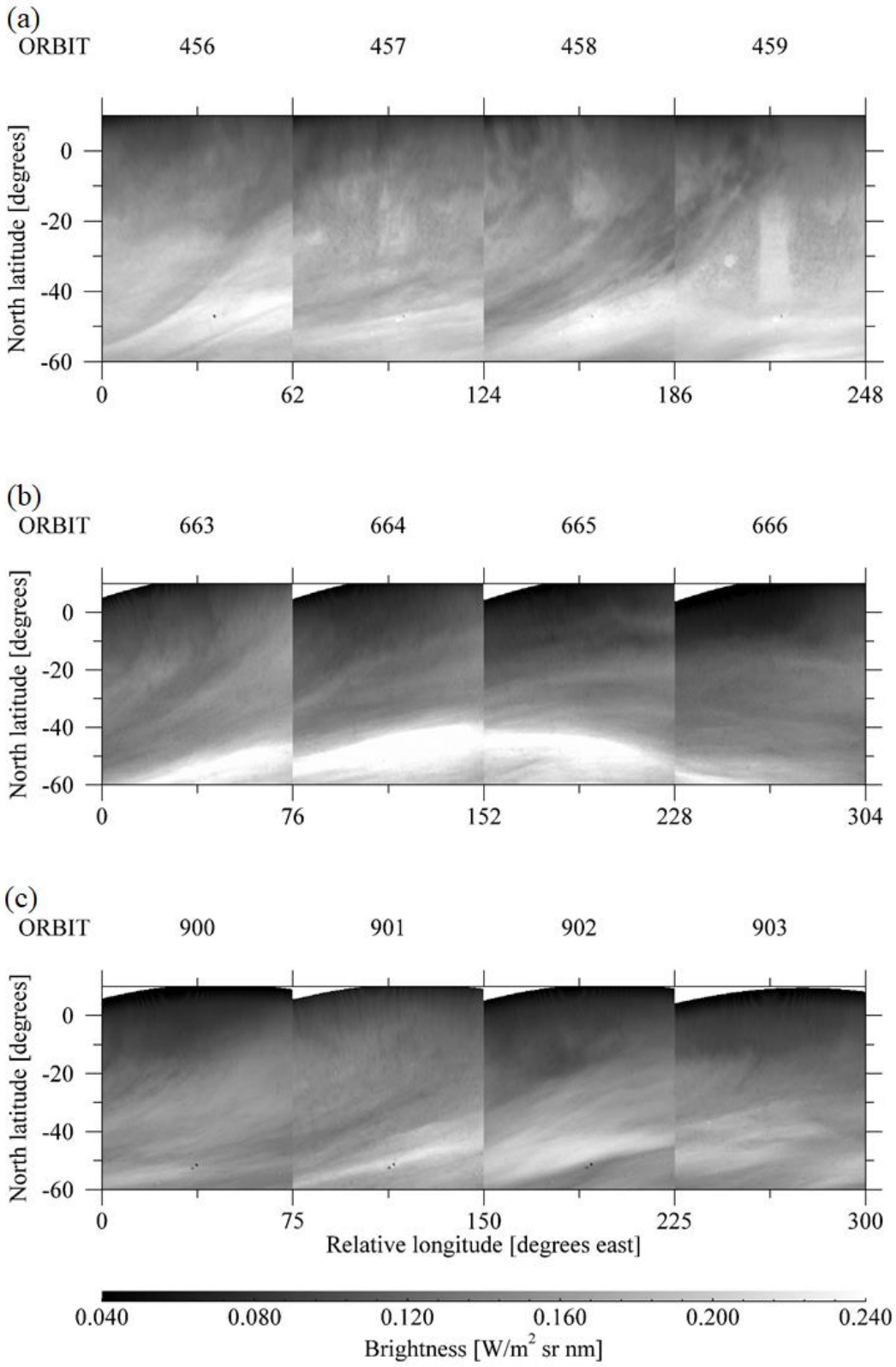

Figure 4. Examples of the mosaic images. Images taken with a time interval of about 24 hours are shifted by (a) 62°, (b) 76°, and (c) 75° in longitude on the assumption that the UV contrasts are advected westward with a rotational period of (a) 5.4, (b) 4.7, and (c) 4.8 Earth days, respectively. These periods

correspond to the recurrence periods of the background flow obtained by cloud tracking.

2.4.2. Velocity fields

Figure 5 shows a typical example of the deduced velocity field superimposed on the corresponding image. The background zonal velocity in solid body rotation corresponding to the dayside-mean angular velocity at the equator was subtracted from each vector. Comparison of the velocity field with the brightness distribution suggests that poleward flow is enhanced around the boundary between the tilted dark band on the west side and the white band on the east side, both of which extend in the northeast-southwest direction. Such a tendency has already been suggested by Patsaeva et al. (2015).

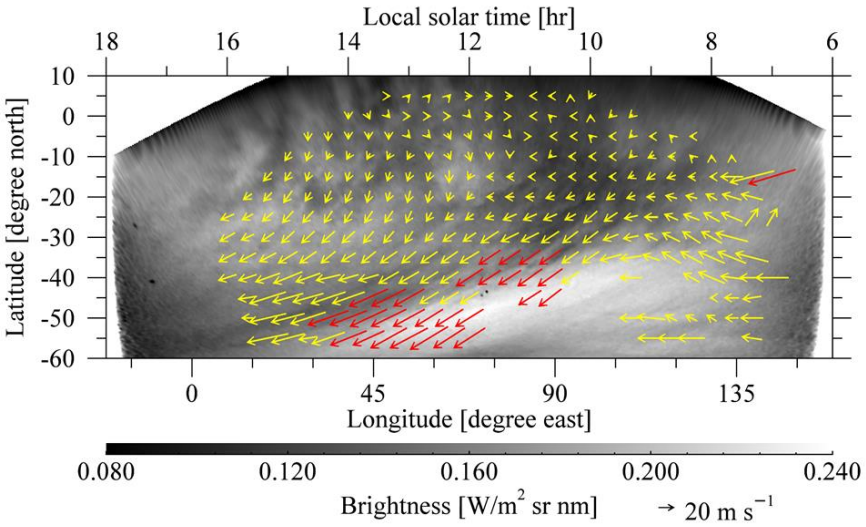

Figure 5. An example of the velocity field obtained from images taken in orbit 458 superimposed on the UV image. The background zonal velocity in solid body rotation corresponding to the dayside-mean angular velocity at the equator was subtracted from each vector. The vectors whose meridional components exceed 15 m s^{-1} are shown in red.

The latitudinal profiles of the dayside-mean zonal velocity and the rotation period of the atmosphere for orbit 436-490 are shown in Figure 6. This mean velocity, obtained by averaging cloud-tracked velocities on the dayside, is different from the zonal-mean velocity, which is the velocity averaged over the whole latitudinal circle, because of the existence of local time-dependent structures including the thermal tides. The

dayside-mean zonal velocity has a maximum of 96 m s^{-1} at the latitude of 45°S, which is known as the mid-latitude jet. The mean rotation period is ~5.4 Earth days around the equator and decreases to ~2.7 Earth days at 60°S; the period is shorter than the period of the brightness variation (~4 Earth days) on the south of 30°S and longer on the north of 30°S. The dayside-mean zonal velocity obtained in this study are almost consistent with those obtained by other studies including the existence of mid-latitude jets (Hueso et al., 2015; Khatuntsev et al., 2013; Rossow et al., 1990).

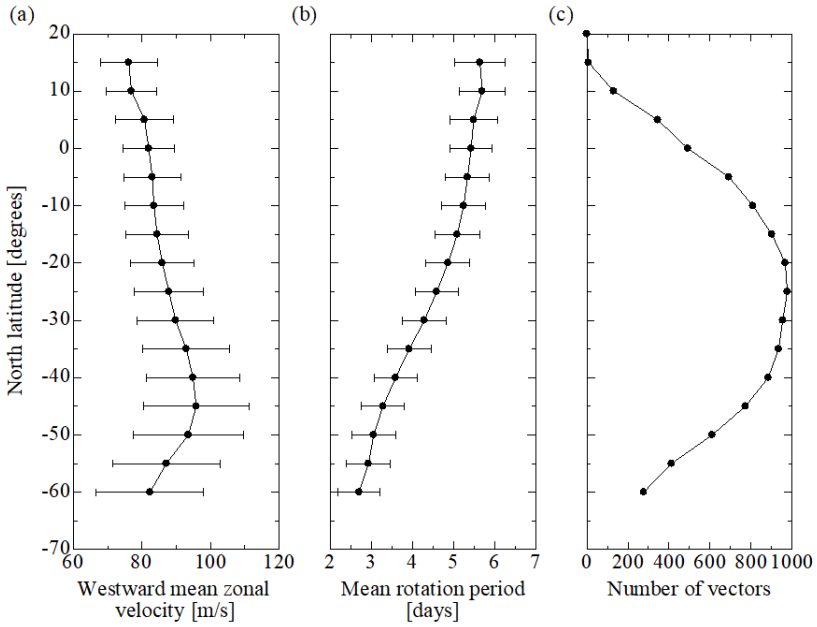

Figure 6. Latitudinal variations of (a) the dayside-mean zonal velocity, (b) the atmospheric rotation period and (c) the number of averaged vectors. Data from orbits 436-490 are used. Horizontal bars show standard deviations.

2.4.3. Periodicities in the velocity

Velocity fields were deduced at an interval of about 1 Earth day. Here I apply periodicity analysis to the velocity time series at the local solar time of 12:00. First, the obtained velocity vectors were averaged on the coordinates fixed to the latitude and the local time (Figure 7). In this local time-dependent component, poleward divergent flows are significant in the afternoon region, being consistent with Patsaeva et al. (2015). Next, the local time-dependent component was subtracted from all velocity vectors; the resultant velocity field mostly contains components propagating with respect to the local time. Then, to utilize all velocity

measurements including those at local solar times other than 12:00, the time when the atmospheric region corresponding to each velocity vector has passed 12:00 was calculated on the assumption that the velocity field is advected at the dayside-mean zonal velocity, and this "corresponding time" was assigned to each velocity vector. Mathematically, letting the time when the velocity was measured be t, the local solar time of the measurement be l, the background zonal wind be $\bar{u}$, the radius of Venus be R_V and the latitude be ϕ, the corresponding time is calculated as $t + (12 - l)/24 \times 2\pi R_V \cos\phi\,/\bar{u}$. Similar analyses were conducted by previous studies (Limaye & Suomi, 1981).

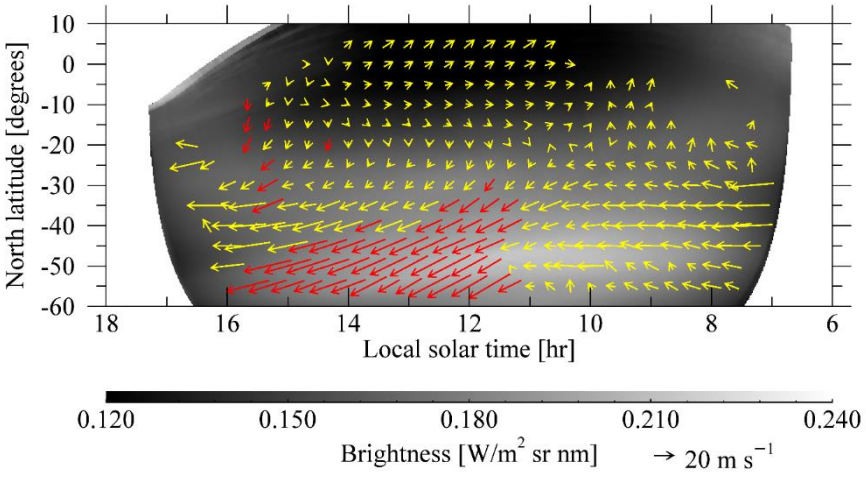

Figure 7. Brightness distribution and the velocity field averaged on the coordinates fixed to the local solar time in orbits 436-490. The vectors whose poleward components are larger than 15 m s^{-1} are shown in red. The background zonal velocity in solid body rotation corresponding to the dayside-mean angular velocity at the equator was subtracted from each vector.

Left panels of Figure 8 show the zonal and meridional velocity time series at 10°S obtained with the procedure above, and the right panels show the Lomb-Scargle periodograms. The analyzed period is orbits 436-465, in which the periodicity around 4 Earth days is most prominent. A measure of the errors in the cloud-tracked velocity when the correlation peak is precisely identified is given by one grid interval divided by the time interval, and is estimated to be 3.7 m s^{-1} at 10°S and 2.8 m s^{-1} at 40°S for the zonal velocity and 3.7 m s^{-1} for the meridional velocity. The uncertainty of the periodogram that originates from this measurement error is much smaller (< 5%) than the power of the spectral peak at ~4 Earth days and does not

influence the detection of the peak.

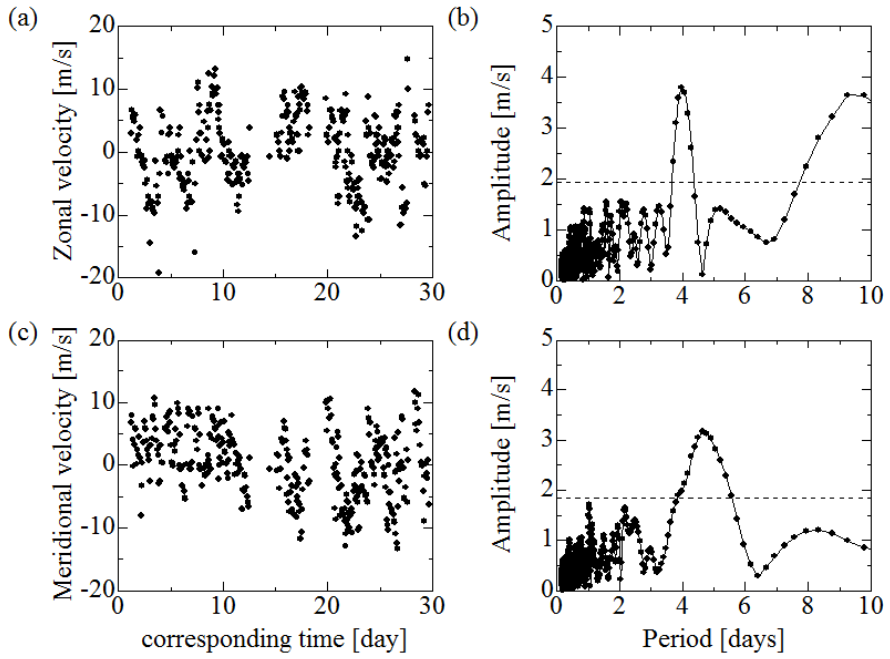

Figure 8. Temporal variations of the (a) zonal and (c) meridional velocities at 10°S in orbits 436-465 after subtracting the solar-fixed component, and (b) (d) their Lomb-Scargle periodograms. The dashed lines show the 99% statistically significant level.

The latitudinal dependences of the periodicities are shown in Figure 9. Dominant periods of ~4 and ~5 Earth days are found both in the zonal and meridional velocities. The dayside-mean zonal velocity is ~82 m s^{-1} near the equator and ~84 m s^{-1} at 15°S, corresponding to the mean rotation period of 5.4 Earth days and 5.1 Earth days, respectively (Figure 6a; b). The mean rotation period is shorter than 5.1 Earth days poleward of 15°S. The 4-day oscillation is attributed to a Kelvin wave because the propagation speed is faster than the dayside-mean zonal velocity if the zonal wavenumber is assumed to be one, the velocity oscillation is predominantly zonal, and the amplitude is large in the low latitude. The 5-day oscillation is prominent in the meridional velocity poleward of 15°S, where the dayside-mean zonal velocity has shorter rotation periods; this feature can be attributed to a Rossby wave. The dayside-mean velocity deduced from the dayside images can be different from the zonal-mean velocity because of the presence of the thermal tide; however, given the amplitude of the thermal tide of ~10 m s^{-1} (Newman & Leovy, 1992; Takagi et al., 2018), the sign of the

intrinsic phase velocities with respect to the zonal-mean zonal velocity would not change even if such a difference is considered, although the amplitude of the thermal tide shows variability (Limaye, 1988). Considering the hemispherically symmetric nature of the mid-latitude oscillation seen in the UV contrast observed by Pioneer Venus (Del Genio & Rossow, 1990), the observed oscillation might represent hemispherically-symmetric Rossby waves. The latitudinally-broad structures are consistent with the linear theories (Imamura, 2006; Kouyama et al., 2015). The periodograms deduced from the same dataset by Kouyama, Imamura, et al. (2013) also show a 4-day periodicity in the zonal velocity and a 5-day periodicity in the meridional velocity, although the peak for the 5-day period does not reach the statistically significant level; the difference is attributed to a smaller number of velocity vectors in Kouyama, Imamura, et al. (2013), where data at a specific local time were used.

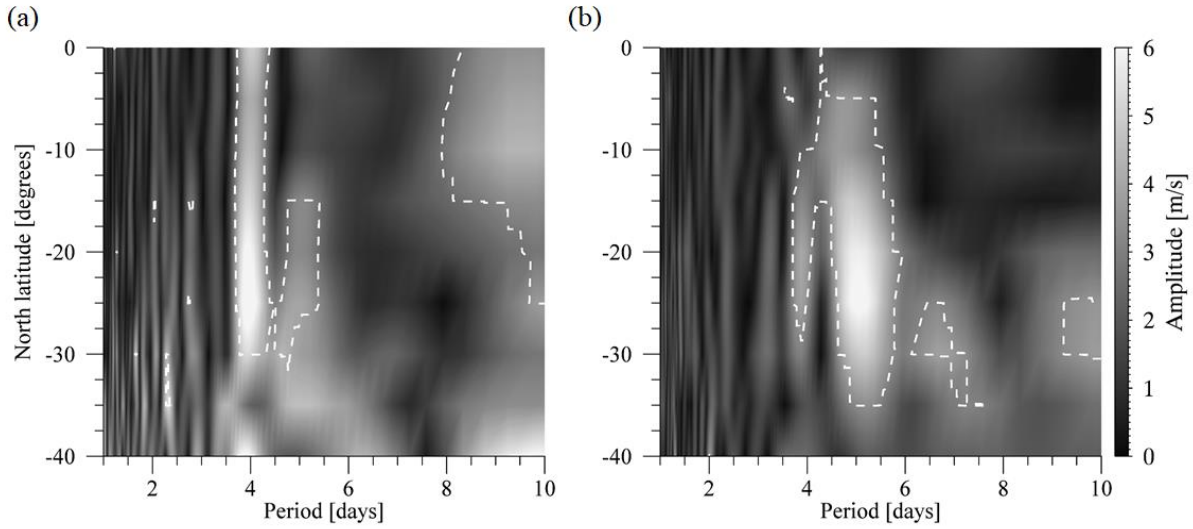

Figure 9. Latitudinal profiles of the periodograms of the (a) zonal and (b) meridional velocities in orbits 436-465 after subtracting the solar-fixed component. Dashed contours represent the 99% statistical significance.

2.5. A scenario for the formation of the Y feature

The temporally- and zonally-oscillating meridional wind can play an important role in distributing the UV absorber. The amplitude of the meridional displacement associated with the 5-day (Rossby) wave is given by

$$\hat{\eta} = \frac{\hat{v}T^*}{2\pi}, \tag{2}$$

where $\hat{v}$ is the amplitude of the meridional velocity and T^* is the intrinsic period. The amplitude of the meridional velocity is estimated to be $\hat{v} = 4.2 \pm 0.3$ m s^{-1} at 30°S by fitting a sinusoidal function to the data. The intrinsic period is given by $(1/T_b - 1/T_w)^{-1} = 24 \pm 7$ Earth days at 30°S, where $T_b = 4.3 \pm 0.1$ Earth days is the period of the background velocity at 30°S and $T_w = 5.2 \pm 0.4$ Earth days is the period of the oscillation. The error in T_b is given by the standard deviation (Figure 6) divided by the square root of the number of the averaged vectors. The half width at half maximum of the periodogram of the meridional velocity gives the error in T_w. Substituting these into (2), I obtain $\hat{\eta} = (1.4 \pm 0.5) \times 10^3$ km or $13 \pm 4°$ in latitude. The total displacement caused by the wave is twice this amplitude, i.e., $27 \pm 8°$ in latitude. This is comparable to the latitudinal extent of the observed dark bands at the cloud top. The occurrence of the strong poleward flow near the prominent streak feature (Figure 5) also implies transport of dark material by the oscillating wind.

As shown in Figure 7, the wind field fixed to the local solar time also shows strong poleward flow in the afternoon region because of the superposition of the thermal tide, whose velocity amplitude is typically ~10 m s^{-1} (Newman & Leovy, 1992; Rossow et al., 1990), on the mean meridional circulation. However, because the thermal tide has a relatively short intrinsic period that is close to the rotation period of the mean zonal wind (typically 4-5 Earth days), the associated meridional displacement is around 2×10 (m s^{-1}) $\times$ 4.5 (Earth days)/2π ~ 1200 km ~ 11°, which is half of that by the 5-day wave. Furthermore, the thermal tide cannot form patterns that propagate at a velocity faster than the super-rotation.

Based on the estimates above, I propose the following scenario. The region of upward flow associated with the Kelvin wave moves westward at a speed slightly faster than the background wind, and the upward wind transports dark material to the equatorial cloud top from below (Del Genio & Rossow, 1990). Then the combination of the mean meridional circulation and the hemispherically-symmetric Rossby wave transports the dark material poleward in both hemispheres. Once the dark material reaches the mid-latitude, the meridional shear of the zonal wind associated with the mid-latitude jet stretches the dark feature in the northeast-southwest (northwest-southeast) direction in the southern (northern) hemisphere, forming the Y shape. Since the meridional velocity amplitude of the Rossby wave is comparable to the mean meridional velocity, which is estimated to be 1-5 m s^{-1} (e.g., Lee et al., 2015; Rossow et al., 1990; Takagi et al., 2018),

the poleward flow undergoes large oscillation, thereby creating the undulation of the boundary between the dark region on the low-latitude side and the bright region on the high-latitude side (Figure 4). Furthermore, since the velocity of the poleward advection of the dark material is variable depending on the phase relationship between the Kelvin wave and the Rossby wave, the slope of the tilted dark band becomes variable as seen in the mosaic images given by Del Genio & Rossow (1982). The periodicity of the radiance in the mid-latitude is determined mostly by the supply of the dark material to the cloud top by the Kelvin wave; though the Rossby wave modulates the efficiency of the poleward transport, it does not seem to change the dominant period (Figure 3).

2.6. Numerical modeling of material transport

The scenario described in the previous section is examined using a two-dimensional transport model on a Cartesian coordinate for the cloud-top atmosphere. The influence of the vertical shear of the mean zonal wind is not taken into account since the mean zonal velocity has a maximum in this height region. Passive tracers representing the dark material are placed artificially near the equator and the subsequent horizontal transport by the mean circulation, the Rossby wave, and the Kelvin wave is modeled. The Rossby wave field is represented by a simple stream function. Since the physical processes are considered to be symmetric about the equator, the model domain includes the southern hemisphere only. Letting x be the westward distance and y be the southward distance with the origin at the equator, the total wind vector (u, v) is a combination of the Rossby wave field (u', v') and the background circulation ($\bar{u}$, $\bar{v}$):

$$u = \bar{u} + u', \tag{3}$$

$$v = \bar{v} + v', \tag{4}$$

$$\bar{u} = u_0 + \left(\frac{y}{L_y}\right)^2 u_1, \tag{5}$$

$$\bar{v} = v_0 \sin(ly), \tag{6}$$

$$u' = \hat{u}_R \sin(kx - \omega_R t) \sin\left(ly + \frac{\pi}{2}\right) + \hat{u}_K \sin(kx - \omega_K t) \exp\left\{-\left(\frac{y}{y_{e-\text{fold}}}\right)^2\right\}, \tag{7}$$

$$v' = \hat{v}_R \cos(kx - \omega_R t) \cos\left(ly + \frac{\pi}{2}\right), \tag{8}$$

where t is the time, $u_0 = 100$ m s^{-1} is the mean zonal wind at the equator corresponding to the rotation period of 4.5 Earth days, $L_x = 3.8 \times 10^4$ km is the zonal span of the model domain corresponding to 360°

on the equator, $L_y = 6.4 \times 10^3$ km is the meridional span of the model domain corresponding to 60° in latitude, and $u_1 = 50$ m s^{-1} is the velocity of the mid-latitude jet at $y = L_y$ corresponding to the rotation period of 3.0 Earth days. The latitudinal profile of the rotation period of the background atmosphere is taken from the mean zonal velocity deduced by cloud tracking in the 6 years of observations by VMC (Sánchez-Lavega et al., 2017) because the relatively short period of my analysis might include notable uncertainty in the mean circulation. $k = 2\pi/L_x$ and $l = \pi/L_y$ are the wavenumbers in the zonal and meridional direction, respectively, $v_0 = 2$ m s^{-1} is the peak velocity of the mean meridional circulation, $\hat{u}_R = 12$ m s^{-1} and $\hat{v}_R = 4$ m s^{-1} are the velocity amplitudes of the Rossby wave, $\omega_R = 2\pi/5.0$ days^{-1} is the frequency of the Rossby wave, $\hat{u}_K = 10$ m s^{-1} is the zonal velocity amplitude of the Kelvin wave, $\omega_K = 2\pi/4.0$ days^{-1} is the frequency of the Kelvin wave, and $y_{e-\mathrm{fold}}$ is the *e*-folding distance corresponding to the latitudinal distance of 25°, which is comparable to the value estimated by Kouyama et al., (2012). The model domain is restricted to equatorward of 60°S, where major dark features exist (e.g., Peralta et al., 2007).

Passive tracers represented by particles are placed every 24 hours at intervals of 10° in longitude and latitude in a rectangular region near the equator (5-25°S) with a longitudinal span of 40° that moves westward at a velocity corresponding to the rotation period of the Kelvin wave (4.0 Earth days), which is expected to supply the dark material to the cloud top. The region where the tracers are supplied is located at the phase of the maximum divergence of the zonal velocity associated with the Kelvin wave, i.e. the phase of the maximum upward displacement. The latitudinal width of the rectangular region is taken from the half width of the Kelvin wave. To visualize stretching of air parcels, the tracers are connected in the north-south direction by thin lines when they are first placed. The dark material seems to have a lifetime on the same order of magnitude as the timescale of the meridional advection because the dark air supplied in the equatorial region becomes brighter during poleward advection and creates the bright polar band around 60° latitude (Figure 4). Considering the timescale of the meridional advection of $L_y/v_0 \sim 37$ Earth days in the model, the color of the tracers is changed to lighter colors every 10 Earth days and the tracers are removed from the system when 30 Earth days has passed since their supply to the equatorial region. A test run without the Rossby wave was also conducted to examine the role of the wave.

Figure 10 shows snapshots of the calculation spanning 20 Earth days where the periodical variation has reached a quasi-steady state; because of the 4-day and 5-day period forcing, the overall variation is repeated every 20 Earth days. The tracers placed near the equator are transported poleward and westward to form a

band structure resembling the observed tilted dark bands. The thin lines connecting the tracers are aligned in the northeast-southwest direction, suggesting that air parcels are stretched in this direction; this feature is consistent with the observed small-scale streaks along the dark bands (Figure 4). Prominent poleward extension of the band structure occurs at the poleward wind phase of the Rossby wave, while the tracers are confined to the equatorial region at the equatorward wind phase of the Rossby wave. The eastern edge of the tracers confined in the equatorial region is stretched zonally by the eastward wind component of the Rossby wave, creating the root of the Y feature. At the leading (western) edge of the Y feature near the equator, the eastward wind component of the Rossby wave pushes the tracers eastward to shape the bow-like structure. Since the phase relationship between the Rossby wave and the equatorial source of the tracers is variable, the overall structure is not steady. Such a variability in the tracer transport leads to the variation of the tilt angle of the dark bands (Del Genio & Rossow, 1982). It should be noted that the magnitude of the mean meridional circulation and the lifetime of the UV absorber are rather uncertain. To examine the sensitivity to these parameters, test runs were performed with the maximum value of the mean meridional circulation of 1-4 m s^{-1} (2 m s^{-1} in the nominal run), and the tracer lifetime of 15-60 Earth days (30 Earth days in the nominal run). The characteristics of the tracer distribution resembling the Y feature were largely unchanged from the nominal run (not shown here).

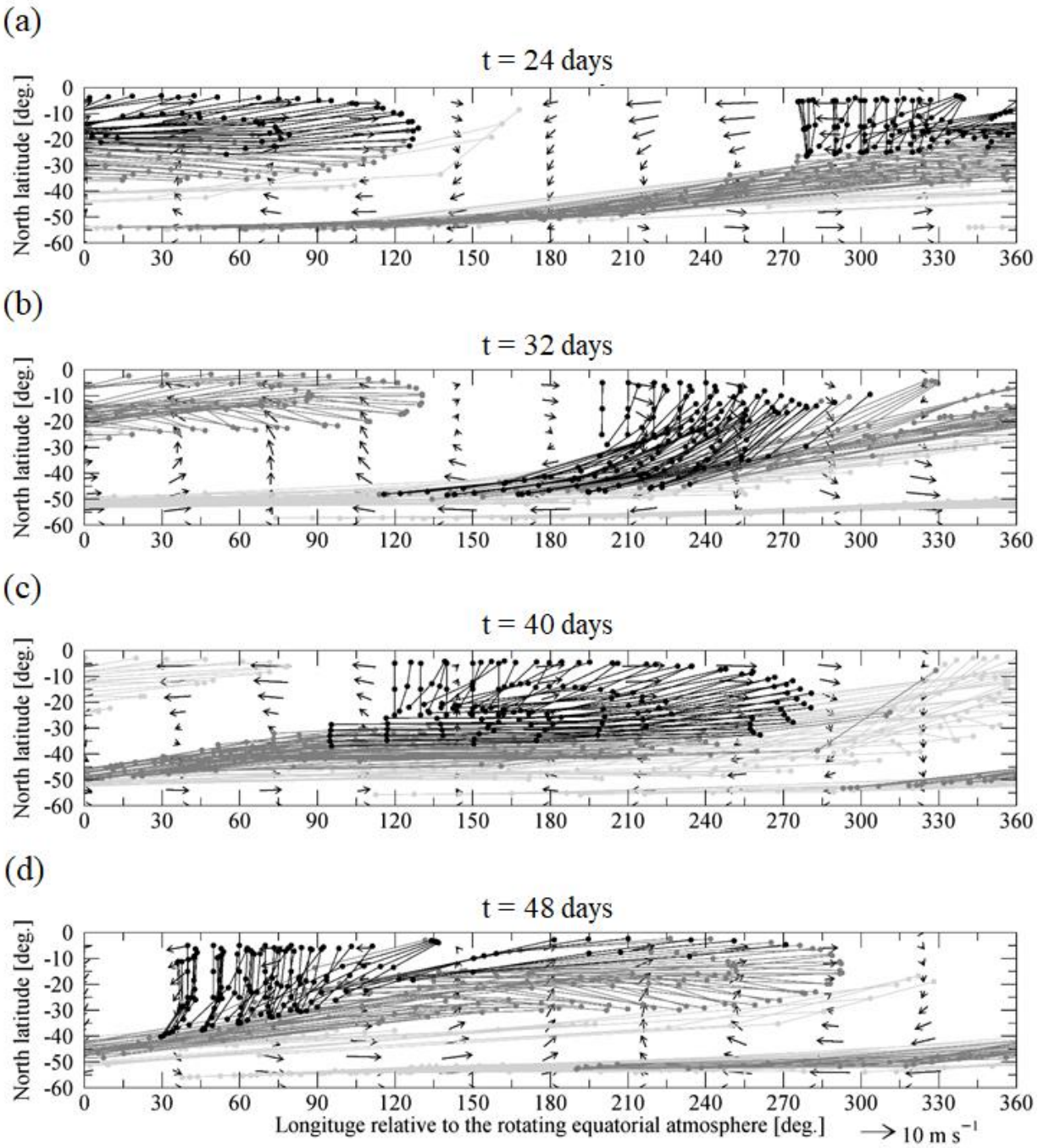

Figure 10. Result of the modeling of tracer transport. Black dots are the tracers within 10 Earth days after supply, gray dots are within 10-20 Earth days, and light gray dots are within 20-30 Earth days. The dots connected by thin lines were aligned in the north-south direction when they were first placed near the equator. The arrows indicate the velocity vectors of the Rossby wave.

Figure 11 shows snapshots of the test run without the Rossby wave. In this case, the tracers supplied near

the equator are transported poleward and westward solely by the mean circulation. Though a dark band is created also in this run, the band is tilted in the northeast-southwest direction only in the mid-latitude poleward of ~35°, where the latitudinal shear of the zonal wind is large. The root of the Y feature in the equatorial region is not created. The orientation of the dark bands is stable with time. The difference between the nominal case and the test run suggests the key role of the Rossby wave in the formation of the Y feature.

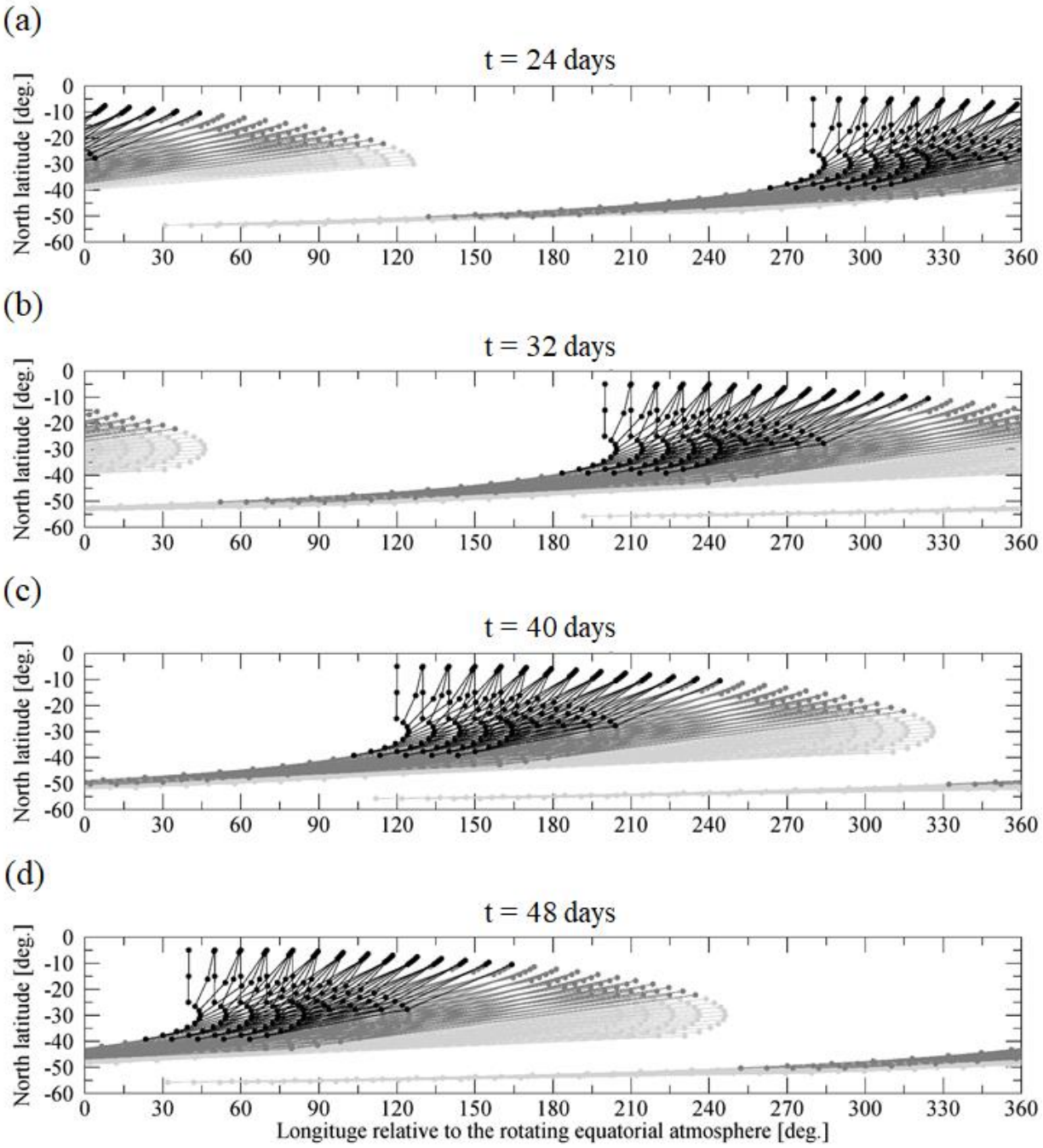

Figure 11. Same as Figure 10 but in the absence of the Rossby wave.

2.7. Summary

I investigated the role of planetary-scale waves and the mean circulation in the formation of the Y feature based on a comparison between the velocity field deduced by cloud tracking and the brightness distribution using 365 nm images obtained by VMC on Venus Express spacecraft. Brightness variations with periods of 4-5 Earth days that are thought to be related to the Y feature are observed most of the time. I focused on orbit 436-490, in which the tilted dark band was clearly observed and the brightness variation had a coherent periodicity of ~4 Earth days independent of the latitude. Spectral analyses of the cloud-tracked velocities revealed existence of ~4 and ~5 Earth day periodicities. The 4-day oscillation was attributed to a Kelvin wave because the phase speed is faster than the background zonal wind, the amplitude is large in the low latitude, and the velocity oscillation is predominantly zonal. The 5-day oscillation was attributed to a Rossby wave because the phase speed is slower than the background zonal wind and the amplitude of the meridional velocity is large in the middle latitude. The meridional displacement of air parcels associated with the Rossby wave was found to be comparable to the latitudinal extent of the Y feature, suggesting a significant contribution.

Based on the observations above, a scenario for the formation of the Y feature is suggested. Dark materials are first supplied to the cloud top by the vertical wind associated with the Kelvin wave from below. The materials are subsequently transported poleward by the combination of the mean meridional circulation and the Rossby wave, and then stretched to the northeast-southwest (northwest-southeast) direction in the southern (northern) hemisphere by the mid-latitude jet, forming the tilted dark bands that constitute the Y feature. Because of the contribution of the oscillating winds to the transport, the tilt of the dark bands becomes variable. A simplified two-dimensional numerical simulation was conducted to examine the transport of passive tracers by the mean meridional circulation, the mid-latitude jet, and the Rossby wave; a tilted band structure resembling the observed Y feature was created, suggesting the validity of the proposed scenario.

In this study, the analysis of the observational data was restricted to the southern hemisphere because of the orbital configuration of Venus Express. The use of images obtained by JAXA's Akatsuki (Nakamura et al., 2016), which is observing both hemispheres of Venus from an equatorial orbit from December 2015,

would allow investigation of the formation of the whole structure of the Y feature. Since multiple wavelength channels in addition to UV are available simultaneously, more detailed analysis of the wave field should be possible. Three-dimensional modeling of tracer transport using Venus GCMs is also needed for comprehensive understanding of the role of atmospheric dynamics in the formation of the planetary-scale brightness contrast. Petrova et al. (2015) pointed out, based on an analysis of UV and near-IR images taken by VMC, that submicron particles also contribute to the formation of the UV contrast; the role of photochemistry and cloud microphysics is left for future studies.

Chapter 3: Vertical coupling between the cloud-level atmosphere and the thermosphere of Venus inferred from the simultaneous observations by Hisaki and Akatsuki

3.1. Introduction

In the thermosphere of Venus, flows direct from the sub-solar to the anti-solar (SS-AS) point are thought to be dominant because of the large temperature gradient associated with the long Venusian solar day of ~117 Earth days. Mayr et al. (1985) pointed out that the SS-AS flow would exceed 300 m s^{-1} at the maximum in the absence of a drag. On the other hand, ground-based Doppler wind measurements using sub-millimeter CO absorption lines showed that the thermospheric wind velocity is ~200 m s^{-1} with significant variability (Clancy el al., 2012); it is believed that breaking of gravity waves generated in the lower atmosphere reach the thermosphere and effectively decelerate the thermospheric wind to the observed values. Gravity waves have been observed at the cloud top and in the middle atmosphere above clouds (e.g., Sánchez-Lavega et al., 2017). Zhang et al. (1996) developed a Venus thermosphere general circulation model taking into account the gravity wave-drag and reproduced a thermospheric circulation with eastward velocity of 140 m s^{-1} at the morning terminator and westward velocity of 265 m s^{-1} at the evening terminator. Gilli et al. (2017) also reproduced the realistic zonal wind profile in the thermosphere of Venus in the presence of wave drag. However, there is no evidence that waves generated in the lower thermosphere are responsible for the drag.

Hoshino et al. (2012) examined vertical propagation of various planetary-scale waves using a general

circulation model and showed that Kelvin and Rossby waves can propagate to the thermosphere without notable attenuation. However, the atmosphere at rest at the lower boundary (80 km) and a symmetric SS-AS flow develops above; this background wind field is not realistic because zonal superrotation dominates below ~ 90 km altitude (Alexander, 1992). Kouyama et al. (2015) showed, using a linear model for the vertical propagation of planetary-scale waves in the cloud-level atmosphere (60-80 km), that Kelvin waves cannot reach >75 km while the vertical propagation of Rossby waves highly depends on the vertical profile of the mean zonal wind.

Masunaga et al. (2015; 2017) analyzed variations of the oxygen atom (O) dayglow intensity of the Venusian thermosphere on both dawn and dusk side using spectroscopic data obtained by the Extreme Ultraviolet Spectroscope for Exospheric Dynamics (EXCEED) on-board the Hisaki spacecraft (Yoshikawa et al., 2014). They detected a periodicity of ~4 Earth days in the dayglow intensity exclusively on the dawn side and pointed out that planetary-scale waves might be responsible for the periodic variations, although the existence of planetary-scale waves at thermospheric heights was not confirmed.

In this study, I investigate the vertical coupling between the cloud-level atmosphere and the thermosphere of Venus via atmospheric waves using data obtained simultaneously by Hisaki and the Venus orbiter Akatsuki (Nakamura et al., 2007) on the dawn side of Venus in June 2017. Hisaki and Akatsuki can obtain information on the Venusian thermosphere and the middle atmosphere, respectively. The rest of this chapter consists of 5 main sections. Section 3.2 describes the dataset, Section 3.3 gives the details of developed models of vertical propagation of atmospheric waves, Section 3.4 discusses the variations of the thermospheric oxygen density with one dimensional photochemical model, and Section 3.5 discusses a possible mechanism for the vertical coupling between the cloud-level atmosphere and the thermosphere and its timescale. Finally, Section 3.6 gives conclusions.

3.2. Observations

The two instruments, EXCEED on Hisaki and UVI on Akatsuki, observed Venus almost simultaneously in June 2017. The period of the EXCEED data used is from 10 June 2017 to 24 June 2017, and that of UVI data is from 1 June 2017 to 31 June 2017. The methods of data processing are given below.

3.2.1. Hisaki data analysis

3.2.1.1. Dataset

EXCEED on board the Hisaki spacecraft, which is orbiting around Earth, has measured extreme ultraviolet spectra of several planets with a temporal resolution of 1 min. EXCEED is a spectro-imager that consists of an entrance mirror, slits of different widths and shapes, a grating, and a microchannel plate detector. Among the slits installed in EXCEED, a dumbbell like shape was used in the observation on June 2017. The width of the wide portion of the slit, which the Venus disk is allocated inside, is 140-arcsec. The spectrograph covers the wavelength region 52-148 nm with a dispersion of 0.1 nm per pixel. For the present observation, the dumbbell-shaped slit was used with a spectral resolution of ~1.5 nm. However, because the apparent diameter of Venus disk seen from the Earth is smaller than the slit width, the effective spectral resolution is determined by the apparent diameter of Venus disk. Details of the instrument and the performance are given by Yoshioka et al. (2013) and Yoshikawa et al. (2014). Among the emissions which EXCEED can detect, the O 135.6 nm emission, which is excited by photoelectron impact, was analyzed in this study because it is sensitive to the thermospheric O density.

3.2.1.2. Analysis method

The apparent diameter of Venus disk seen from the Earth changed from 30 to 20 arcsec during the observation and was smaller than the wide portion of the slit width of 140 arcsec. Figure 1 shows the spectra of Venus across the slit length (Y-axis) integrated over the entire 15 days period. Because the Hisaki orbits around the Earth, the spectrum includes not only the Venusian airglow but also contributions from the geocorona, which is the emission from Earth's exosphere above ~1000 km altitude. The dumbbell-shaped emission at 130.4 nm originates from the geocorona. The trajectory of Venus inside the slit is elliptic because of the pointing error caused by the orbital motion of Hisaki spacecraft (Yamazaki et al., 2014) with its Y-position centered at ~580 pixels. Due to this motion, the Venus disk was sometimes out of the slit.

To retrieve the airglow intensity of Venus with high accuracy, I have developed a method to determine the position of the center of Venus disk as shown in Figure 2. The main panel in Figure 2 shows an example of the spectrum of 1-min integration. The rectangle area surrounded by yellow dotted lines shows the upper part of the dumbbell slit determined by the O 130.4 nm geocoronal emission as shown in Figure 1. By fitting a Gaussian function to the spectrum averaged along Y-axis within the slit, the X-position of Venus disk was

determined (the right panel in Figure 2). The Y-position is obtained similarly by averaging the spectrum along X-axis and fitting a Gaussian function to it (the top panel in Figure 2). Then, the data in which the Venus disk was not inside the slit were removed from the analysis. The position of O 135.6 nm was 46 pixels (corresponds to ~ 5 nm) from that of 130.4 nm. The intensity of the O 135.6 nm emission is derived by integrating the counts within ±5 pixels from the center. To eliminate the contamination from the geocorona, I subtracted the counts 50 pixels away from the Venus disk on the other side of the dumbbell similarly to the method adopted by Nara et al. (2018).

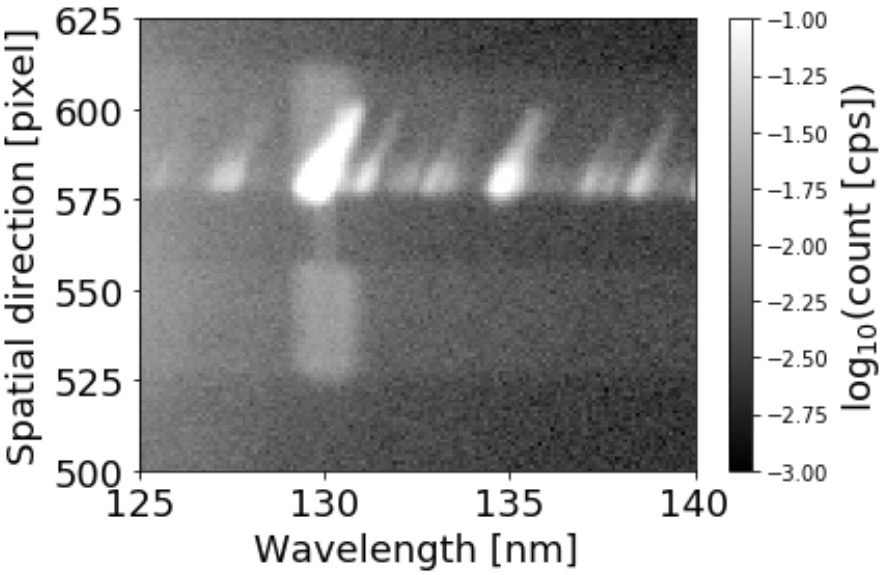

Figure 1. Spectrum integrated for 10-24 June 2017 obtained by EXCEED. The dumbbell-shaped frame seen at around 130 nm is the O geocoronal emission. Venusian emissions are located at a spatial direction of ~580 pixels. The position of Venus disk relative to the slit is variable due to the pointing error of Hisaki spacecraft.

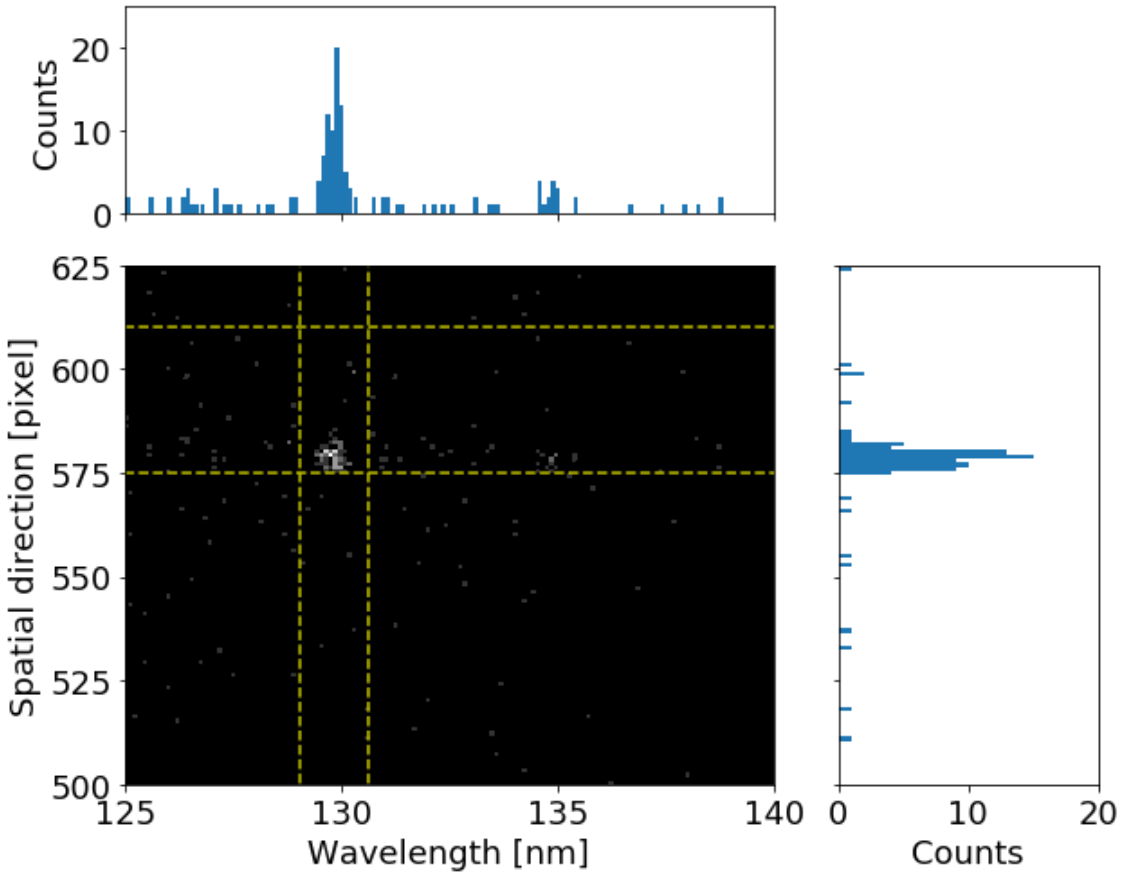

Figure 2. An example of the determination of Venus disk position for O 130.4 nm emission. Upper panel shows the sum of the counts between the horizontal dashed lines for each wavelength and is used to determine the x-position of the Venus disk. Right panel shows the sum of counts between the vertical lines for each spatial distance and is used to determine the y-position of the Venus disk.

3.2.1.3. Periodicity in airglow intensity

Figure 3a shows the temporal variation of the O 135.6 nm dayglow intensity on the dawn side. The averaged intensity is ~400 Rayleigh in this period, although ~1000 Rayleigh on June 2015 (Masunaga et al., 2017). This difference can be understood with variations of the solar UV intensity. The monthly averaged F10.7 indices were 133 on June 2015 and 77 on June 2017 (https://www.spaceweather.gc.ca/solarflux/sx-5-mavg-en.php). The difference in the airglow intensity between the periods is attributed to the difference in the solar activity, which should control the density of photoelectrons that excite oxygen atoms. Figure 3b shows its periodogram obtained by Lomb-Scargle method (Scargle, 1982), which can be applied to unevenly sampled data. A periodicity of 3.6 ± 0.2 Earth days, which exceeds the statistical significance of 99%, is

identified. This variation can be attributed to the O atom column density above 130 km, where the optical depth of CO_2 is unity at a wavelength of ~136 nm (Von Zahn et al., 1980). The amplitude of the ~3.6-day variation is 29±4 Rayleigh which is ~4% of the background value, implying ~4% variation also in the O atom column density.

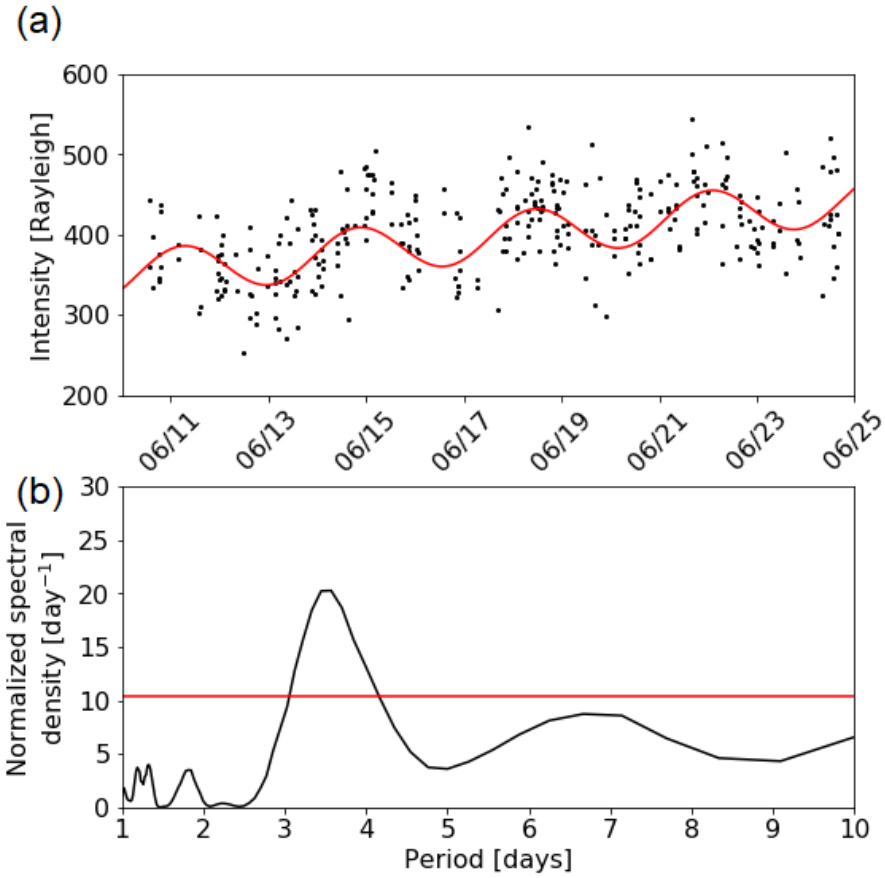

Figure 3. (a) Temporal variation of O 135.6 nm intensity and (b) its Lomb-Scargle periodogram. The red curve in (a) shows a sinusoidal function with a period of 3.6 days and a linear function fitted to the data. The red line in (b) shows the 99% statistical significance level of the periodogram.

3.2.2. Akatsuki data analysis

3.2.2.1. Dataset

I used 365-nm UV images of UVI, which are sensitive to the absorption by unidentified materials that absorb solar radiation at wavelengths from ultraviolet to violet (Moroz et al., 1985). UVI has the field of view is 12° × 12° and takes images of 1024 × 1024 pixels. The pixel resolution of UVI at the sub-spacecraft point is ~80 km at the pericenter. The details of Akatsuki are given in Nakamura et al. (2016) and the

specifications of UVI are given in Yamazaki et al. (2018).

As a preprocessing, the original image data were converted to Akatsuki's Level-3 (L3) data format, in which images are projected onto longitude-latitude maps with the method described in Ogohara et al. (2017). During the projection the pointing direction was corrected by a limb fitting method proposed by Ogohara et al. (2012) and the optical distortion was corrected by the method of Kouyama et al. (2013). The grid interval of the L3 data is 0.125° both in latitude and longitude.

3.2.2.2. Analysis method

To retrieve variations of the UV brightness, I first applied Minnaert's law, which relates the observed brightness I to the photometrically corrected brightness I_0:

$$I = I_0 \mu^{k-1} \mu_0^k, \quad (1)$$

where μ is the cosine of the emission angle, μ_0 is the cosine of the incidence angle, and k is a parameter to be determined by least-squares fitting (Minnaert, 1941). This photometric correction has widely been used for images of the planets covered with thick clouds including Venus (Lee et al., 2015; Titov et al., 2012). I calculated I_0 over the area with emission and incidence angle less than 80° (Nara et al., 2019).

The dependence on the scattering phase angle still remains after the photometric correction (Lee et al., 2017; Markiewicz et al., 2014). To eliminate this dependence, polynomial functions were fitted to the whole data by least-squares method (Figure 4). Figure 4 shows the phase angle dependence of the UV albedo calculated from I_0 and a function fitted to the data. The albedo is defined as $r = \pi I_0 d_v^2 / \Phi_0(365\ \mathrm{nm})$, where $\Phi_0(365\ \mathrm{nm}) = 1.085\ \mathrm{W\ m^{-2}\ sr^{-1}\ nm^{-1}}$ is the solar irradiance at 365 nm at 1 AU and d_v is the Sun-Venus distance in unit of AU. As the fitting function, polynomials of 2-6th degree are found to yield similar results, and I adopted a quartic function. By dividing I_0 by the fitted function, the apparent large excursions synchronized with the phase angle change were successfully removed (Figure 5). Therefore, this phase angle corrected I_0 was used in this study.

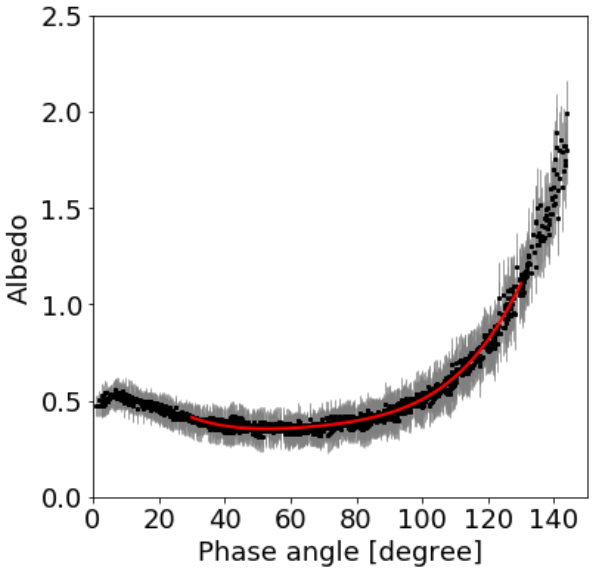

Figure 4. Phase angle dependence of the global mean UV albedo (black dots) and fitted quartic function (red curve).

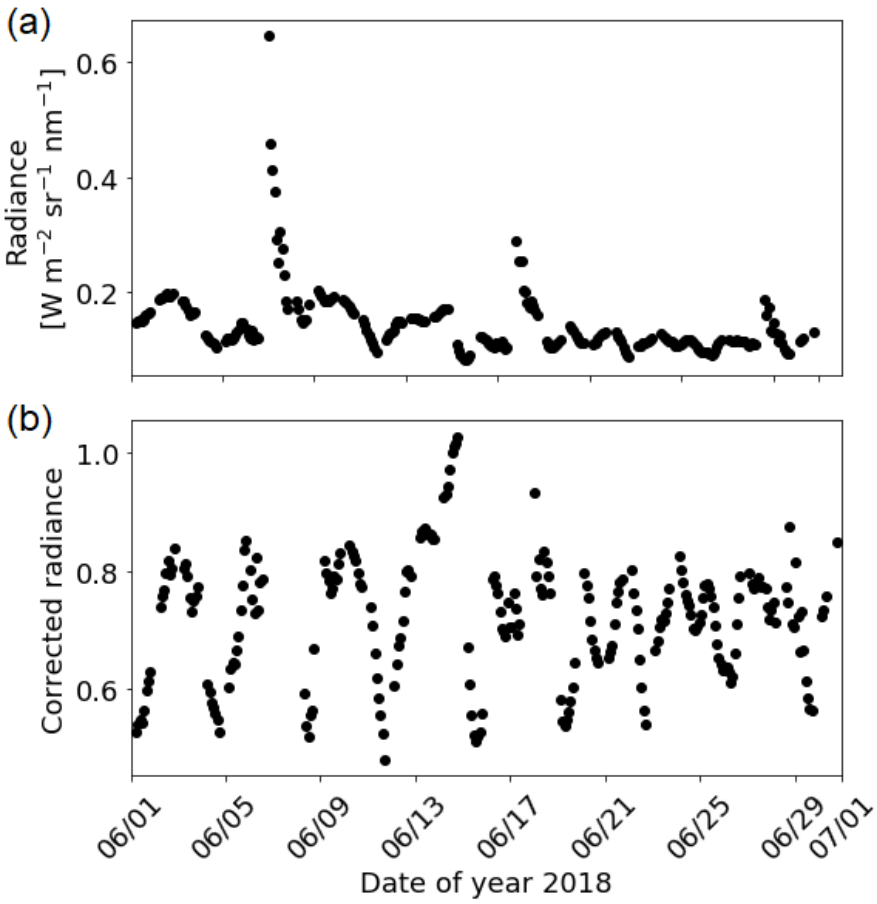

Figure 5. Time series of the UV brightness at the equator averaged over local solar time of 11:00-13:00 (a) without and (b) with the correction of the phase angle dependence.

3.2.2.3. Periodicity in the UV brightness and the velocity at the cloud top

Figure 6 shows the periodogram of the UV contrast from which the phase angle dependence was removed. Periodicities of 3.6 ± 0.1 Earth days are seen around the equator and 4.0 ± 0.1 Earth days in the middle latitude of both hemispheres. The period of 3.6 days is identical to that detected in the O dayglow intensity (Section 3.2.1.3).

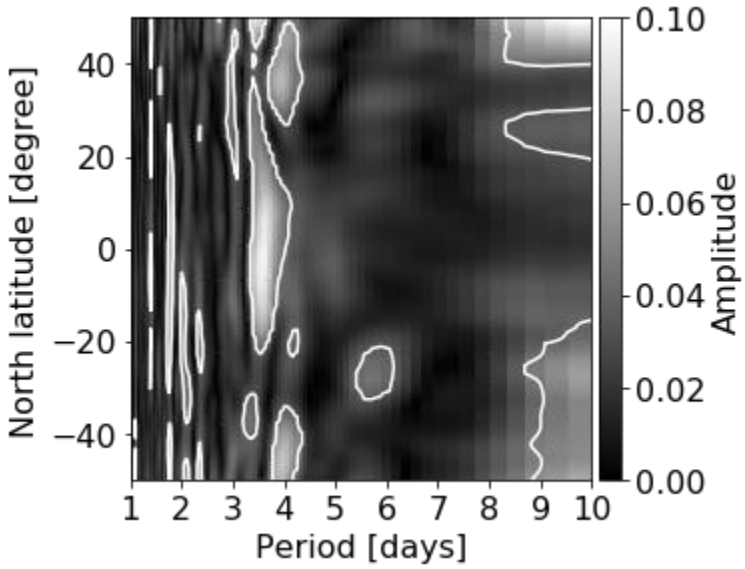

Figure 6. Latitudinal variation of the Lomb-Scargle periodogram of the phase angle corrected I_0 averaged over local solar time of 11:00-13:00. White contours show the 99% statistically significant level.

I also deduced velocity fields at the cloud top with cloud tracking from the same dataset using the method developed in Chapter 2, although some settings were different; the size of the template was set to 8° × 8° and the search region was determined assuming that the westward velocity is between 0 and 150 m s^{-1} and the meridional velocity is between -50 and 50 m s^{-1}. Velocities were obtained every 4° in both longitude and latitude. Figure 7 shows the latitudinal distribution of the dayside-mean zonal velocity deduced by cloud tracking and the corresponding rotation period.

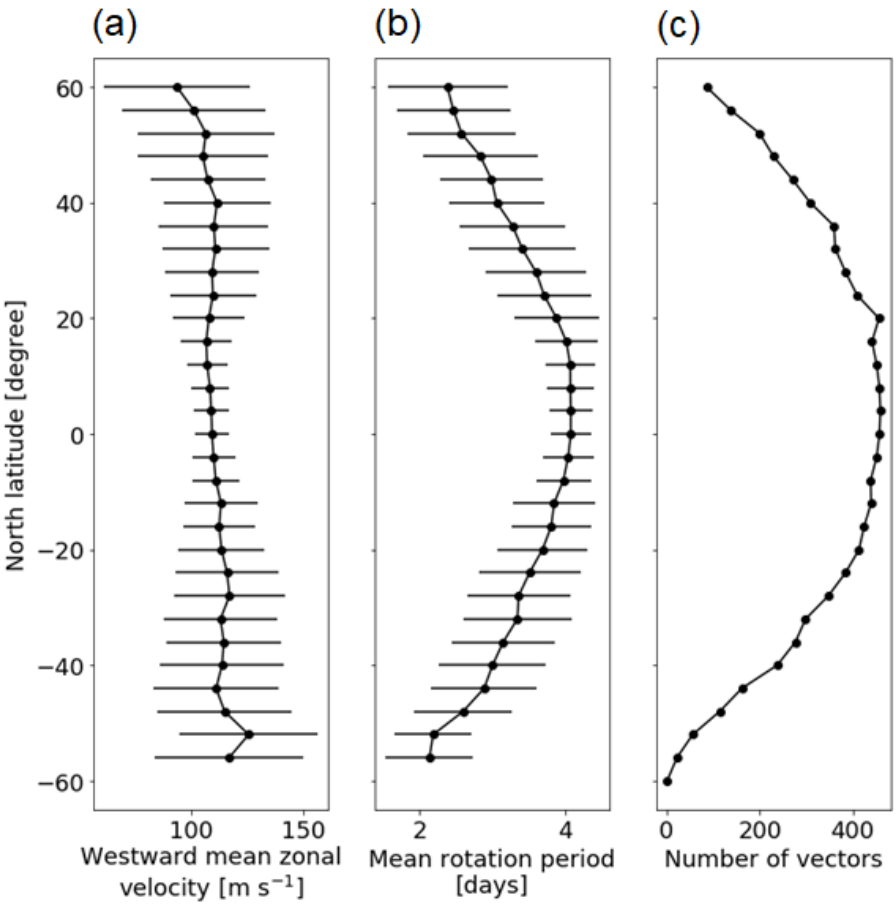

Figure 7. Latitudinal variations of (a) the dayside-mean zonal velocity, (b) the atmospheric rotation period and (c) the number of averaged vectors. Horizontal bars show standard deviations.

Figure 8 shows the temporal variation of the deviation of the zonal velocity from the mean velocity obtained above on the equator and its periodogram obtained by Lomb-Scargle method. Latitudinal variations of the periodograms of the zonal and meridional velocities are shown in Figure 9. A periodicity of 3.6 ± 0.1 days is seen in the zonal velocity in the low latitude; this variation can be attributed to a Kelvin wave because the westward phase velocity is faster than the mean zonal velocity near the equator if the zonal wavenumber is assumed to be one as suggested by previous studies (e.g., Kouyama et al., 2015). The larger amplitude in the low latitude than in the high latitude and the predominantly zonal oscillation are also consistent with a Kelvin wave. The 3.6-day variation found in the meridional velocity peaking at around 30°S cannot be attributed to a Kelvin wave because its propagation speed is slower than the dayside-mean zonal velocity poleward of 20°S. Occurrence of a Rossby–Kelvin mode due to shear instability (Iga & Matsuda, 2005) might explain the same periodicity for the equatorial and the mid-latitude modes. There also exists a distinct

5-day periodicity in the zonal and meridional velocities, which is considered as a Rossby wave because of its slow propagation relative to the background wind. This component is, however, almost absent in the periodogram of the brightness (Figure 6). The discrepancy was explained by Nara et al. (2019): the Kelvin wave with a period of ~3.6 days supplies dark materials from below to the cloud top by vertical wind oscillation to create a periodical variation of the brightness, while a Rossby wave with a period of ~5 days has a minor effect on the brightness oscillation because of its negligible vertical wind oscillation. Imai et al. (2019) also detected a ~4-day periodicity both in the brightness and the velocity and a ~5-day periodicity in the velocity in the same dataset.

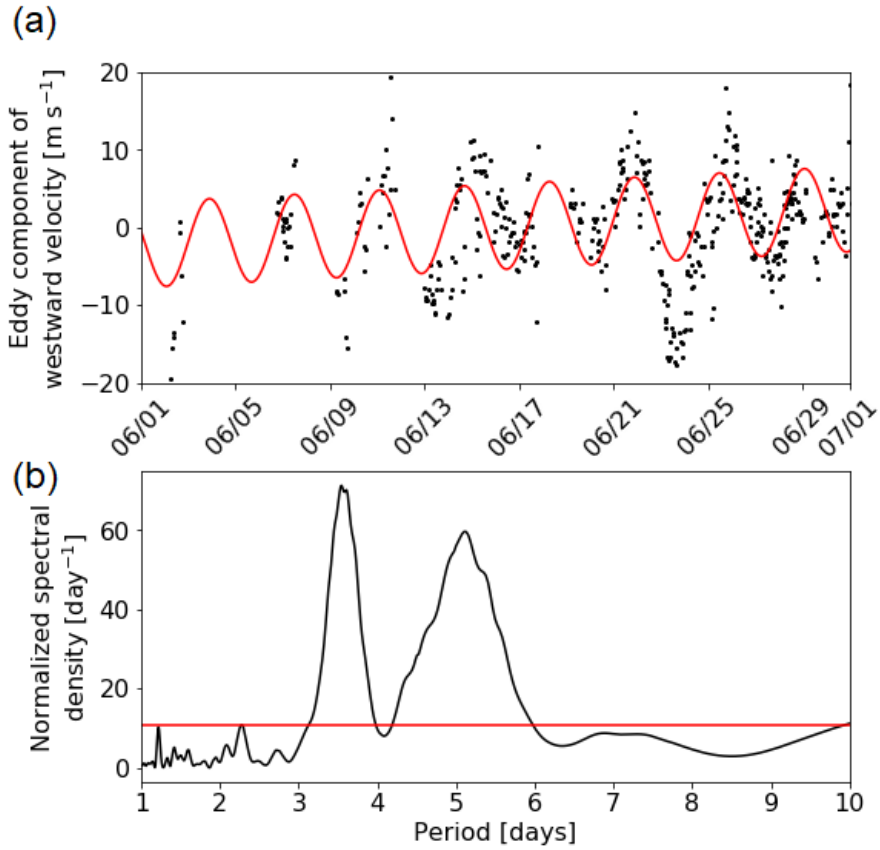

Figure 8. (a) Temporal variation of the eddy component of the westward velocity and (b) its Lomb-Scargle periodogram. The red curve in (a) shows the sum of a sinusoidal function with a period of 3.6 days and a linear function fitted to the data. The red line in (b) shows the 99% statistical significance level of the periodogram.

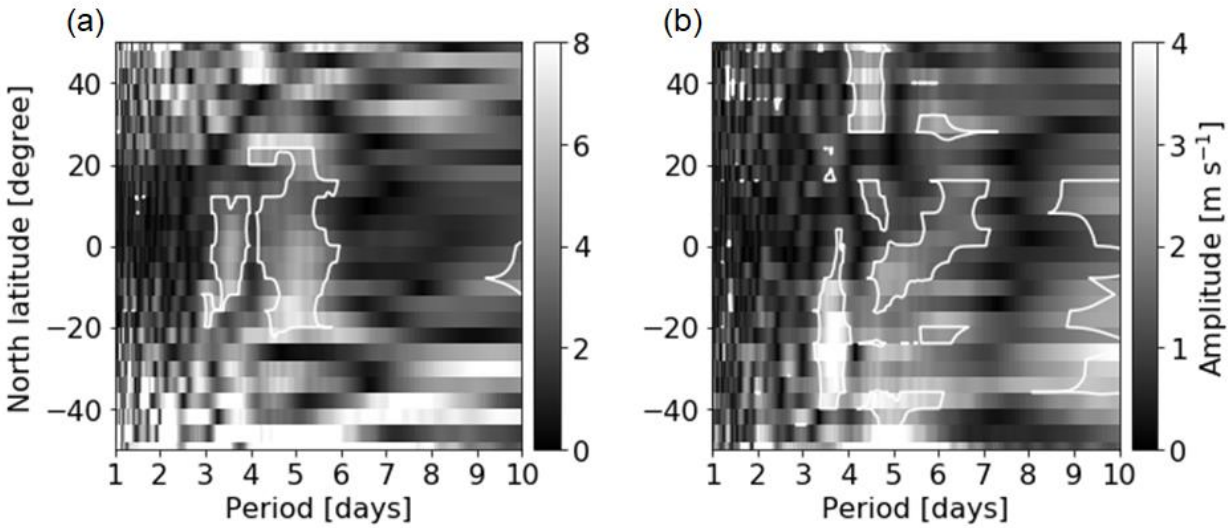

Figure 9. Latitudinal profiles of the periodograms of the (a) zonal and (b) meridional velocities. White contours represent the 99% statistical significance.

3.2.3. Comparison of the periodicities between the thermosphere and the cloud top

Periodicities of 3.6 ± 0.2 days, 3.6 ± 0.1 days, and 3.6 ± 0.1 days were detected in the thermospheric O airglow intensity, the cloud-top UV brightness, and the cloud-top zonal velocity, respectively. In the estimate of the error in the period, I first calculate the standard deviation σ of the spectral density outside of the spectral peaks and regard this quantity as the uncertainty in the spectral density and also in the spectral peaks. Then, the possible range of the peak period is defined by the period bins where the spectral density is higher than P_0 - σ, where the P_0 is the spectral density at the peak period. The agreement between the periods in the thermosphere and the cloud level suggests that the variation in the thermosphere is controlled by the variation in the cloud-level atmosphere. The phase difference between airglow intensity and the westward velocity is small such that the maximum (minimum) velocity precedes the maximum (minimum) airglow intensity by 4±2 hours. In the following sections, I investigate the vertical propagation of Kelvin and small-scale gravity waves in the presence of radiative damping and the response of the thermospheric O atom density to vertical mixings, which may be responsible for the variation of the airglow intensity.

3.3. Vertical propagation of gravity waves

3.3.1. Model description

I examine the vertical propagation of a Kelvin wave and a small-scale gravity wave from the cloud level to the thermosphere as possible mechanisms for the vertical coupling, using a one-dimensional gravity-wave model (Eckermann et al., 2011). The Kelvin wave is modeled as a long gravity wave because the longitude-height structure of a Kelvin wave is identical to a gravity wave having the same wavelength and the period. The small-scale gravity wave is assumed to be generated by convection in the cloud (Imamura et al., 2014; Lefèvre et al., 2017) and have a phase velocity close to the cloud-level mean velocity.

The wave damping is represented by the imaginary part of the complex vertical wavenumber: $M = m + im_i$ such that

$$m_i = \frac{1}{\tau c_{gz}}, \tag{2}$$

where c_{gz} is the vertical group velocity and τ is the damping time. Neglecting the Coriolis force and assuming that the wave propagates predominantly in zonal direction, c_{gz} is given by

$$c_{gz} = \frac{-\omega^*}{k^2 + m^2 + \alpha^2}, \tag{3}$$

where $\omega^* = k\left(c - u_0(z_0)\right)$ is the intrinsic frequency with c being the horizontal phase velocity and u_0 the background zonal velocity as a function of the altitude z, k is the horizontal wavenumber, and $\alpha^2 = 1/4H_\rho^2$, with H_ρ being the density scale height. The real part of the vertical wave number is calculated by the dispersion relationship:

$$m^2 = \frac{k^2\left(N^2 - \omega^{*2}\right)}{\omega^{*2}} - \alpha^2 \tag{4}$$

where N is buoyancy frequency.

The major damping process is radiative damping due to CO_2 15-μm absorption band below the thermosphere and molecular diffusion in the thermosphere (Hinson & Jenkins, 1995). The model adopts a constant radiative damping time τ_r of 1 days, which is comparable to those given in Crisp (1989). Test runs with τ_r = 1 and 2 days confirmed that the result is not sensitive to this parameter. The molecular viscous coefficient is represented as Banks & Kockarts (1973);

$$\mu = \sum_i \frac{\mu_i}{\frac{1}{N_i}\sum_j N_j \phi_{ij}}, \tag{5}$$

$$\phi_{ij} = \frac{\left\{1 + \left(\frac{\mu_i}{\mu_j}\right)^{\frac{1}{2}} \left(\frac{M_j}{M_i}\right)^{\frac{1}{4}}\right\}^2}{2\sqrt{2}\left(1 + \frac{M_i}{M_j}\right)^{\frac{1}{2}}}, \quad (6)$$

where i (or j) = 1, 2 and 3 denotes O, CO, and CO_2, respectively, N_i is the number density of the i-th species and M_i is the mass of the i-th species. The viscous coefficients of each species are given by Chapman & Cowling (1970) and Banks & Kockarts (1973): $\mu_1 = 3.90\times10^{-7}T^{0.69}$, $\mu_2 = 1.635\times10^{-5}(T/273)^{0.734}$, and $\mu_3 = 1.380\times10^{-5}(T/273)^{0.933}$ kg m^{-1} s^{-1}. The damping rate due to molecular diffusion τ_v^{-1} and the total damping rate τ^{-1} are expressed as

$$\tau_v^{-1} = \mu(k^2 + m^2 + \alpha^2)\rho^{-1}, \quad (7)$$

$$\tau^{-1} = \tau_r^{-1} + \frac{1}{2}(1 + p_r)\tau_v^{-1}, \quad (8)$$

where p_r represents the Prandtl number. p_r was set to 0.8 which is appropriate for the CO_2 atmosphere (Eckermann et al., 2011). Wave-induced shear and convective instabilities are not included because these processes depend on the absolute value of the amplitude which is not calculated in the model. Though these processes can suppress the wave amplitude, the wave is not totally destroyed unless it encounters a critical level. Critical level absorption may prevent vertical propagation on the dusk side where the background wind at upper levels is close to the superrotational wind at the cloud level; this effect does not influence the conclusion on the dawn-dusk contrast (Section 3.3.2).

The vertical profile of the momentum flux is calculated as

$$F(z) = F(z_b)\exp\left[-2\int_{z_b}^{z} m_i(z')dz'\right], \quad (9)$$

where z is the altitude and z_b is the bottom of the model where the momentum flux is specified as the boundary condition. The model extends from 70 km to 150 km altitude with a grid interval of 0.1 km. The profiles of the atmospheric temperature and the densities of CO_2, CO and O are taken from the Venus International Reference Atmosphere (VIRA) (Seiff et al. 1985; Keating et al. 1985). Two types of the zonal wind profile u_0 which lead to different intrinsic frequency ω^* are adopted; one is for the dawn side where the wind direction changes at high altitude and the other is for the dusk side where a westward wind extends to the thermosphere (Alexander, 1992; Clancy et al., 2015). The adopted wind profiles (Figure 10) are much simpler than the observed ones because the difference in the intrinsic phase velocity between dawn and dusk

side is the most important and detailed structures do not influence the conclusions. These profiles are shown in Figure 10.

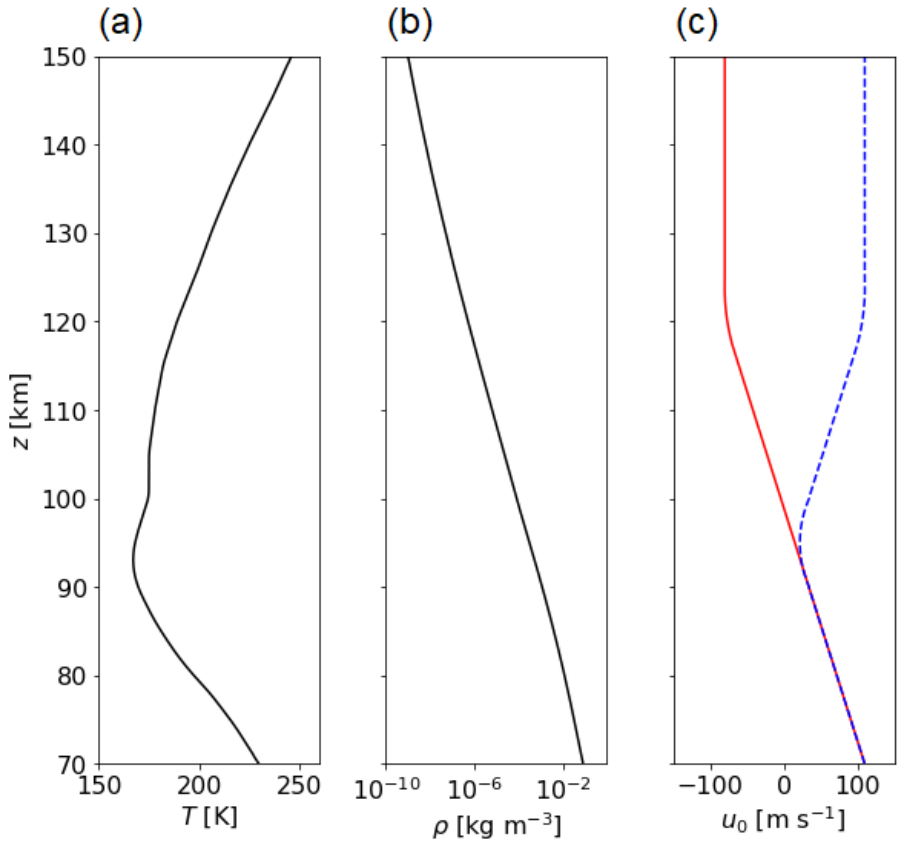

Figure 10. Vertical profiles of (a) the temperature, (b) the total density, and (c) the zonal velocity used in the model. The temperature and the density are taken from VIRA (Keating et al., 1985; Seiff et al., 1985). The red solid line of the zonal velocity represents the velocity on the dawn side and the blue dashed line represents that on the dusk side.

3.3.2. Results

I modeled a gravity wave with a zonal wavenumber of unity and a period of 3.6 Earth days. The wave corresponds to the Kelvin wave observed at the cloud top and has a horizontal phase velocity of 124 m s^{-1}, which is slightly faster than the background zonal velocity at 70 km altitude.

Figure 11 shows vertical profiles of the damping time τ for the two u_0 profiles given in Figure 10c, the corresponding momentum fluxes and the amplitudes normalized by their bottom values. Radiative damping is the dominant damping process below 110 km altitude, while molecular diffusion becomes predominant

above. The result shows that the Kelvin wave is efficiently attenuated in the first scale height by radiative damping and cannot propagate to the thermosphere in both of the u_0 profiles. This is because the wave's vertical group velocity of ~2 km day^{-1} is too slow for the wave to propagate through the altitude region with a damping time of ~1 day.

Next, I calculated the vertical structure of a gravity wave with a horizontal wavelength of 1000 km and a phase velocity of 115 m s^{-1}, which is also slightly faster than the background zonal wind at 70 km altitude. Though waves with phase velocity less than the background wind should also be generated in the cloud, such waves encounter critical levels just above the cloud top, and thus they are not considered in this study. The result (Figure 12) shows that the wave reaches the bottom of the thermosphere (~110 km altitude) in both of the u_0 profiles. This is because the wave's vertical group velocity of ~30 km day^{-1} is fast enough for the wave to propagate through the altitude region with a damping time of ~1 day. Above this height the wave propagates further upward on the dawn side (negative u_0 at high altitudes), while it is rapidly attenuated on the dusk side (positive u_0 at high altitudes). This is because the intrinsic frequency ω^* becomes large at high altitudes on the dawn side, thereby reducing m and increasing τ and c_{gz}. The results are qualitatively the same for horizontal wavelengths of 500-2000 km and phase velocities of 112-120 m s^{-1} as shown in Figure 13; I set the phase velocity at >110 m s^{-1} so that critical levels do not exist near the lower boundary.

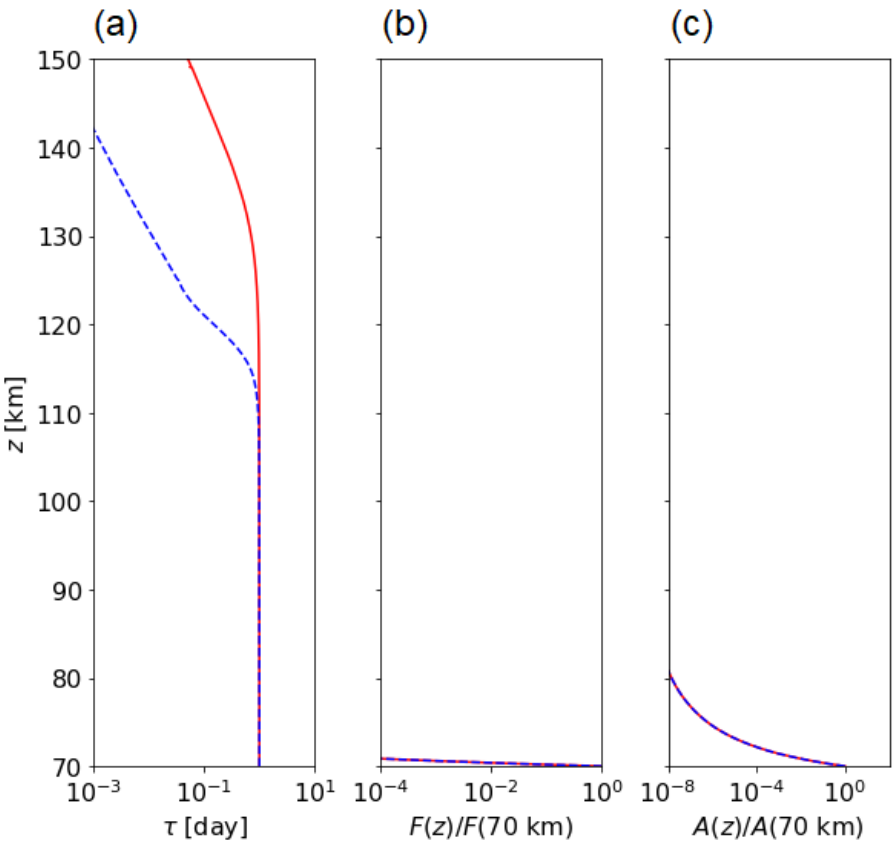

Figure 11. Vertical profiles of (a) the damping time, (b) the wave momentum flux relative to those at 70 km altitude, and (c) the wave amplitudes relative to those at 70 km altitude for a Kelvin wave in the presence of the background wind representing the dawn side (red solid lines) and the dusk side (blue dashed lines). The wavelength and the phase velocity of the wave are 3.8×10^4 km and 124 m s^{-1}, respectively.

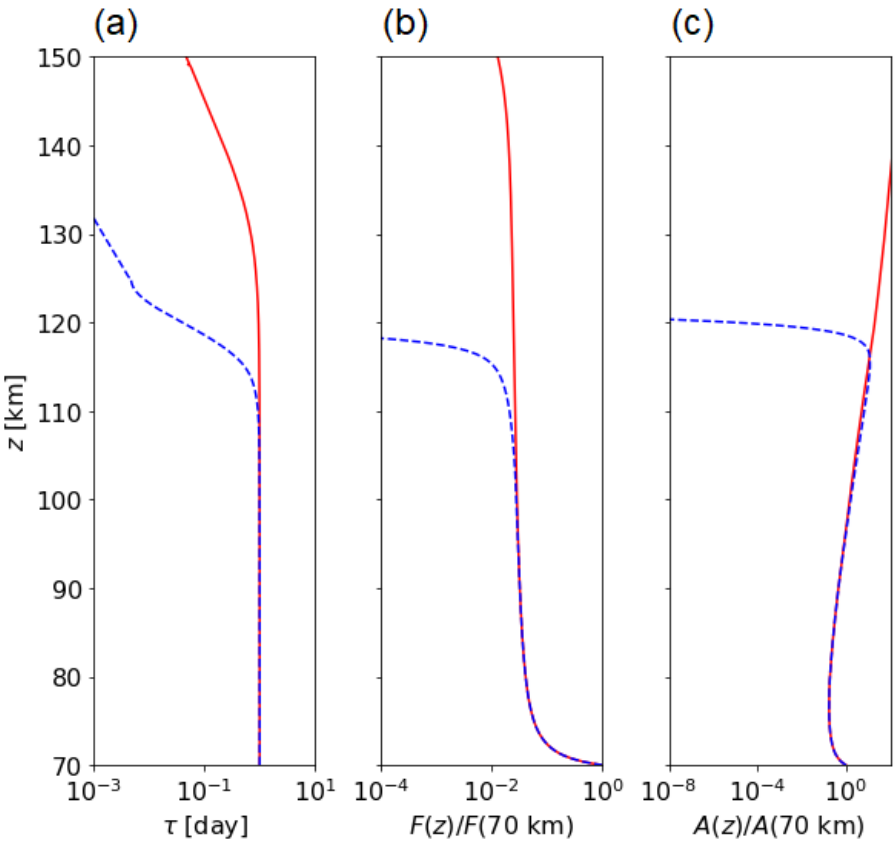

Figure 12. same as Figure 11 but for the small-scale gravity wave. The wavelength and the phase velocity of the wave are 1.0 × 103 km and 115 m s^{-1}, respectively.

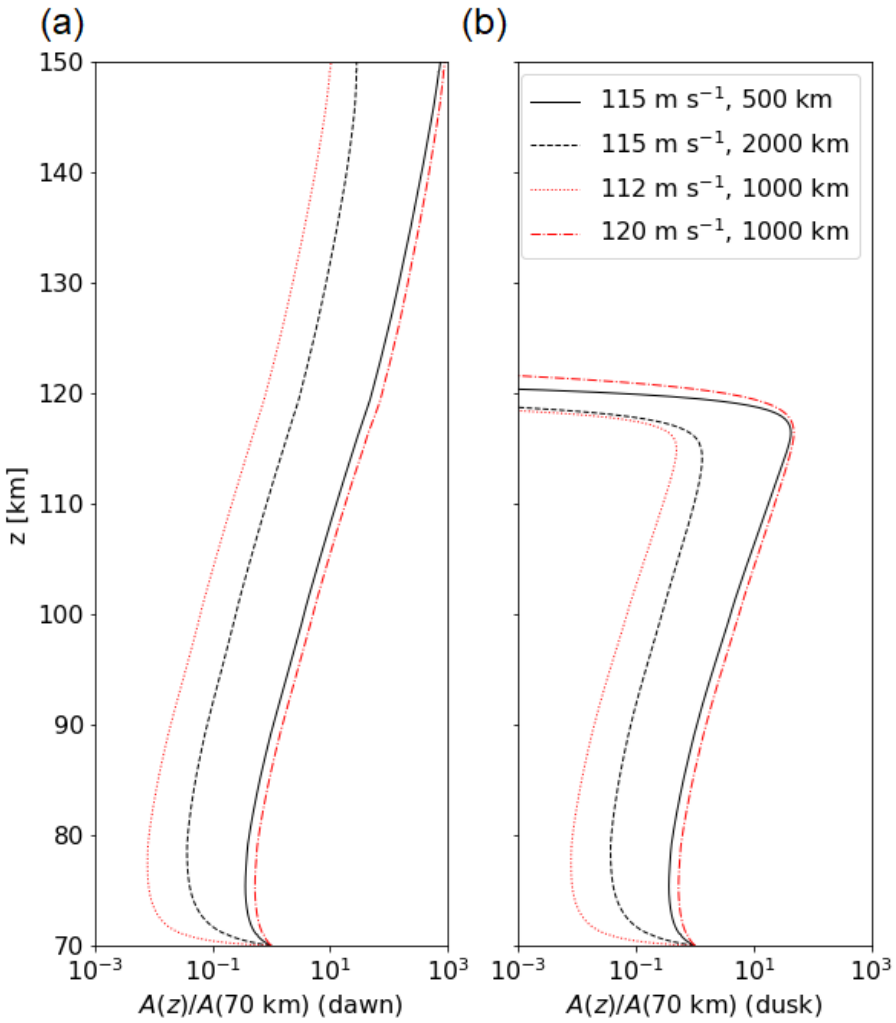

Figure 13. Amplitude profiles of small-scale gravity waves with wavelengths of 500-2000 km and phase velocities of 112-120 m s^{-1} on (a) dawn and (b) dusk sides.

According to the results above, the periodical variation of the airglow intensity cannot be explained by a direct influence of the Kelvin wave. A possible mechanism is the modulation of small-scale gravity wave fluxes by the Kelvin wave. For example, periodical variations of the static stability or the vertical shear caused by the Kelvin wave will change the efficiency of the convective generation of the gravity waves. It is also possible that changes in the zonal velocity induced by the Kelvin wave influence the existence of critical levels for gravity waves. Through these processes, gravity wave fluxes can be modulated at the period of the Kelvin wave. The gravity waves that reach the thermosphere will break to produce turbulence or induce large-scale circulation via momentum deposition. The turbulence or the induced circulation transports O downward, thereby reducing the O density via three-body recombination (eq. 11) as suggested by

Masunaga et al. (2017). Such a change in the O density may be responsible for the variation of airglow intensity. The dawn-dusk difference in the gravity wave propagation shown in Figure 12 is consistent with the observation that the periodicities of several days in the airglow intensity were detected only on the dawn side (Masunaga et al., 2017).

3.4. Modeling of the perturbation of atomic oxygen density

3.4.1. Model description

The O dayglow intensity is expected to be roughly proportional to the column O density above ~130 km altitude, above which the 136 nm radiation can escape to space (Von Zahn et al., 1983). The predominant production and loss processes of O are the photodissociation of CO_2 (eq. 10) and three-body-recombination of O (eq. 11), respectively (Fox & Bougher, 1991). The column density of O is affected by the downward transport of O by turbulence and large-scale circulation, both of which can be driven by gravity waves. To model the response of the O density to vertical transport, I developed a simple one-dimensional photochemical model that extends from 50 km to 200 km altitudes. I consider a binary atmosphere which consists of CO_2 and O. The profiles of the temperature, pressure and CO_2 density are assumed to be invariable. The production and loss processes of O included in the model are

$$\mathrm{CO_2} + h\nu \rightarrow \mathrm{CO} + \mathrm{O}, \tag{10}$$

$$\mathrm{O} + \mathrm{O} + \mathrm{CO_2} \rightarrow \mathrm{O_2} + \mathrm{CO_2}. \tag{11}$$

The continuity equation to be solved is

$$\frac{dn_O}{dt} = P - L - \frac{d\Phi}{dz}, \tag{12}$$

where n_O is the O density, P is the production rate, L is the loss rate, and Φ is the vertical flux expressed as

$$\Phi = -(D + K)\frac{dn_\mathrm{O}}{dz} - \left[D\left(\frac{1}{H} + \frac{1}{T}\frac{dT}{dz}\right) + K\left(\frac{1}{H_a} + \frac{1}{T}\frac{dT}{dz}\right)\right] n_\mathrm{O} \tag{13}$$

where $D = \mu/\rho$ is the binary diffusion coefficient of O against CO_2 with μ being the molecular viscous coefficient given by eq. (5) and ρ being the atmospheric density, K is the eddy diffusion coefficient, $H_a = R_\mathrm{O}T/g$ is the scale height of O with R_O being a gas constant of O, g the acceleration of gravity and T the temperature, and $H_a = R_aT/g$ is the atmospheric scale height with R_a being the gas constant of air (Chaffin et al., 2017). K represents various transport processes including turbulent diffusion and large-scale transport.

The vertical eddy diffusion in a one-dimensional model can represent horizontally-averaged vertical transport including both small-scale turbulence and large-scale circulation because both of them can induce vertical mixing. Gravity waves can induce mean-wind acceleration/deceleration via momentum deposition, thereby driving large-scale vertical transport (e.g., Holton et al., 1995). P and L are expressed as

$$P(z) = n_{CO_2} \int d\lambda \left\{ \sigma(\lambda) \Phi_0(\lambda) \exp\left[-\frac{1}{\cos\theta} \sigma(\lambda) \int_z^\infty n_{CO_2} dz \right] \right\}, \quad (14)$$

$$L = 2kn_O^2 n_{CO_2}, \quad (15)$$

where n_{CO_2} is the CO_2 density, λ is the wavelength of the incoming solar radiation, $\sigma(\lambda)$ is the absorption cross-section of CO_2 (Von Zahn et al., 1983), $\Phi_0(\lambda)$ is the solar spectrum, $\theta = 45°$ is the approximate solar zenith angle at the sub-Earth point, and $k = 5.4 \times 10^{-33} (300/T)^{3.25}$ is the rate coefficient for the recombination of O (Chaffin et al., 2017). The solar spectrum was taken from the American Society for Testing and Materials (ASTM) (https://www.nrel.gov/grid/solar-resource/spectra-astm-e490.html).

To model the periodical variation of the vertical transport at the period of the Kelvin wave, the eddy diffusion coefficient K is changed as:

$$K = K_0 + \hat{K} \frac{1 - \cos\frac{2\pi t}{T_K}}{2}, \quad (16)$$

where t is the time, K_0 is the background diffusivity, $\hat{K}$ is the amplitude of the oscillating component, and $T_K = 3.6$ days is the period of the Kelvin wave. K_0 is assumed to be 100 $m^2 s^{-1}$ so that the basic state with $\hat{K} = 0\ m^2\ s^{-1}$ yields a O profile roughly consistent with VIRA (Keating et al., 1985). I solved the time evolution of the O density profile by integrating (12) with $\hat{K} = 200, 300, \text{and } 400\ m^2\ s^{-1}$. The solution for $\hat{K} = 0\ m^2\ s^{-1}$ is obtained first by running the model until a quasi-equilibrium state is reached, and this state is used as the initial condition for other $\hat{K}$ cases. The vertical grid interval is 5 km.

3.4.2. Results

Figure 14 shows the equilibrium profile with $\hat{K} = 0\ m^2\ s^{-1}$. The production of O is mainly balanced by the downward diffusion of O above ~110 km altitude, while O atoms transported from the upper atmosphere are lost by recombination below ~110 km. A neutral mass spectrometer on board Pioneer Venus orbiter conducted in-situ measurements of the atmospheric composition including O atoms above ~150 km

(Niemann et al., 1980). The O atom density calculated by the photochemical model is roughly consistent with the measured O atom density; at 160 km altitude, the observed O atom density ranged from 1×10^8 cm^{-3} to 2×10^9 cm^{-3} while the model yields 9.4×10^8 cm^{-3} in the equilibrium state. The profile at the phase of the maximum diffusion coefficient with $\hat{K} = 300\ m^2\ s^{-1}$ is also plotted; this phase corresponds to the phase of the minimum column density. The decrease of the O density occurs mostly below ~120 km because of the enhanced downward diffusion and the subsequent loss.

The time development of the column O density above 130 km is shown in Figure 15. The amplitude of the O density variation increases with $\hat{K}$. The run with $\hat{K} = 300\ m^2\ s^{-1}$ yields a peak-to-peak amplitude of the fractional column density variation of ~9%, which is close to the amplitude of the airglow intensity (Figure 3). This result implies that ~300% change in the diffusion coefficient can cause the observed dayglow variation. Verification of this amount of variation in vertical transport is left for future research.

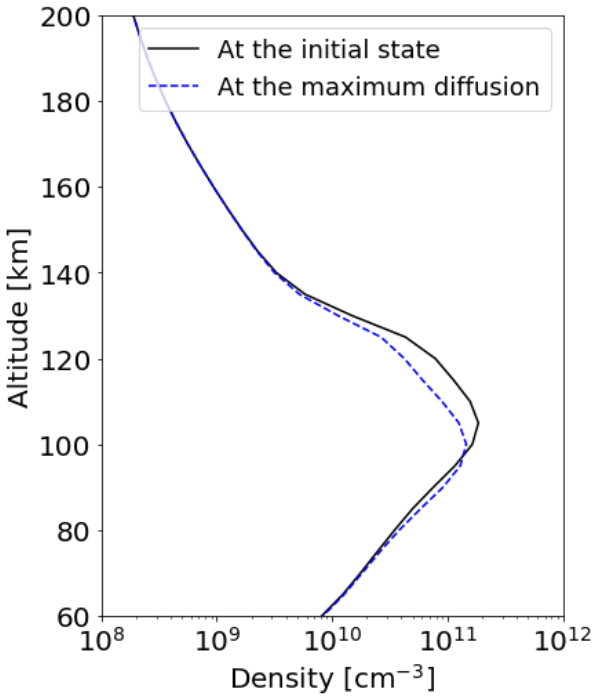

Figure 14. The O density profile (black solid curve) in the background state and that at the phase of the maximum diffusion coefficient (blue dashed curve).

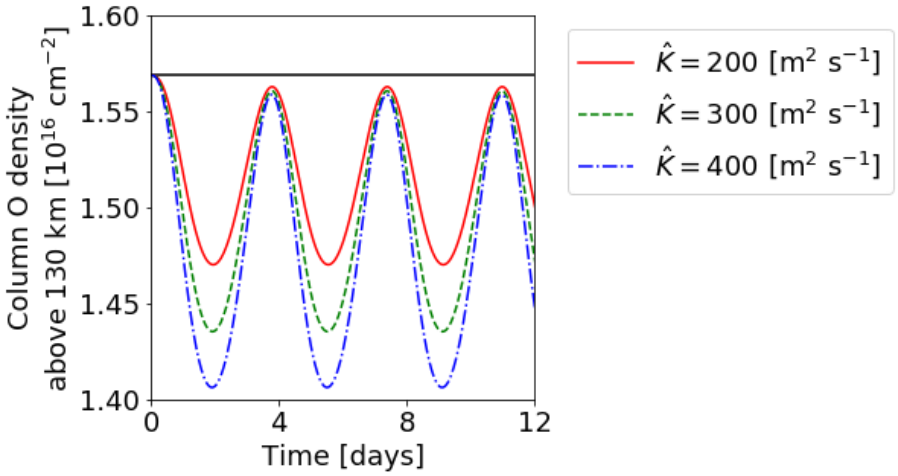

Figure 15. Temporal variations of the column O density above 130 km altitude. Solid black line shows the equilibrium value for the background eddy diffusion coefficient of 100 m^2 s^{-1}. Solid, dashed, and dot-dashed curves show the results of the eddy diffusion coefficient amplitudes of $\hat{K}$ = 200, 300 and 400 m^2 s^{-1}, respectively.

3.5. Time scale of vertical coupling

A common periodicity of ~3.6 days was detected in the thermospheric O atom intensity, the UV brightness, and the equatorial zonal velocity at the cloud level. The wave propagation (Section 3.3) showed that the Kelvin wave cannot reach the thermosphere because of radiative damping while small-scale gravity waves. This result suggests that gravity waves are responsible for the vertical coupling and the Kelvin wave modulates the efficiency of gravity wave generation or propagation. The group velocity of the small-scale gravity wave in the model increases from 0 m s^{-1} at 70 km altitude to 6 m s^{-1} at 130 km, and thus it takes (60 km)/(3 m s^{-1}) ~ 5.6 hours to propagate this altitude range. This suggests that the vertical coupling can occur in a short timescale as compared to the Kelvin wave period, although the typical gravity wave parameter in the Venusian atmosphere is uncertain.

The photochemical model (Section 3.4) showed the amplitude of the eddy diffusion coefficient of ~300 m^2 s^{-1} explains the observed variation of the airglow intensity. The comparison between the timeseries of the column O density and the eddy diffusion coefficient shows that the minimum (maximum) of the O density lags behind the maximum (minimum) of the eddy diffusion coefficient by 2.9 hours, suggesting that the airglow intensity responds quickly to the change of vertical transport. The sum of the propagation time (5.6

hours) and the diffusion time (2.9 hours) exceeds the phase difference (4 hours); this is attributed to the uncertainties in the estimates or suggests that wave filtering occurs at altitudes higher than the cloud top.

Given the estimates above, the observed small phase difference between the maximum (minimum) westward velocity at the cloud top and the maximum (minimum) airglow intensity seems to be consistent with a scenario that an increase of the westward velocity blocks transmission of gravity waves generated below the cloud top if the amplitude of the Kelvin wave peaks at the cloud top. Further studies on wave excitation and filtering would constrain the mechanism of vertical coupling.

3.6. Summary

I investigated the vertical coupling between the cloud level and the thermosphere using 365 nm images obtained by UVI on Akatsuki and the O 135.6 nm dayglow intensities obtained by EXCEED on Hisaki. The simultaneous observation revealed a common periodicity of ~3.6 days, and the oscillation at the cloud-level was attributed to a Kelvin wave because the phase speed is faster than the background zonal wind, the amplitude is large in the low latitude, and the velocity oscillation is predominantly zonal.

A one-dimensional model revealed that the Kelvin wave cannot propagate from the cloud level to the thermosphere because of radiative damping. The modeling also revealed that a small-scale gravity waves having wavelengths of ~1000 km can propagate to the thermosphere on the dawn side and that the waves are strongly attenuated on the dusk side. The dawn-to-dusk asymmetry of gravity wave propagation is consistent with the previous observations by Hisaki (Masunaga et al., 2017) that oscillations in the thermosphere were seen on the dawn side only. According to the results above, the periodical variation of the airglow intensity might be explained by the influence of the Kelvin wave on the generation or transmission of small-scale gravity waves. The gravity waves that reach the thermosphere will break to produce turbulence or induce large-scale circulation via momentum deposition (Figure 16).

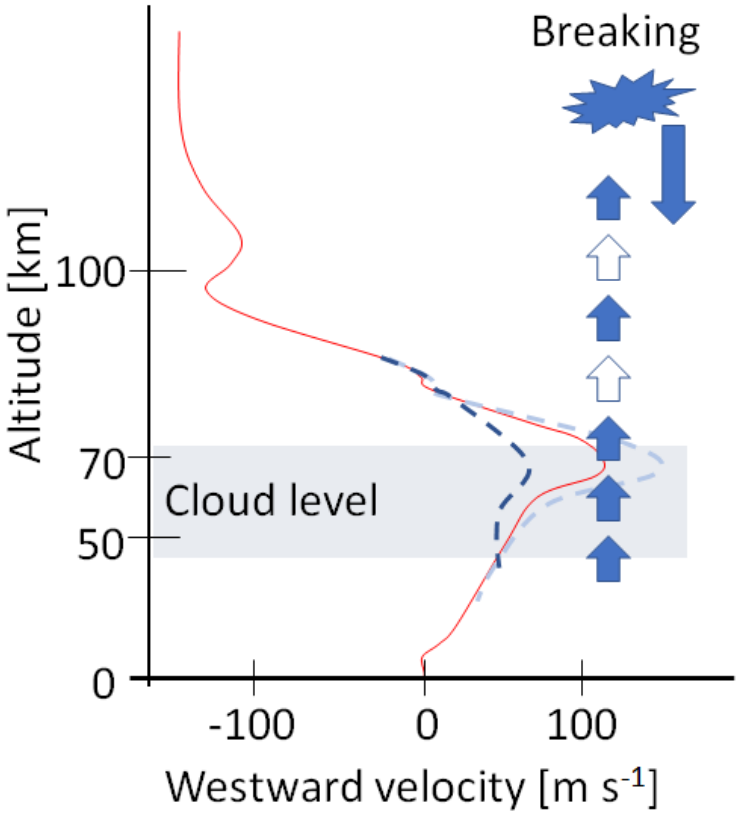

Figure 16. Schematic view of the vertical coupling via a Kelvin wave and small-scale gravity waves. The red curve represents a typical zonal wind profile and this profile is modulated by the Kelvin wave around the cloud top level (the amplitude is exaggerated). Upward arrows indicate the vertical propagation of small-scale gravity waves that are generated below the cloud top. The gravity waves are periodically filtered by the oscillation of the background zonal wind associated with the Kelvin wave. The gravity waves that reach the thermosphere will break and induce downward transport of oxygen atoms (downward arrow).

I further developed a one-dimensional photochemical model to investigate the response of the O density profile to the change of vertical transport caused by gravity waves. The model showed the amplitude of the diffusion coefficient of ~300 m^2 s^{-1} explains the observed airglow intensity. It would also be valuable to analyze additional data from simultaneous observations conducted after the measurements used in this study; Hisaki observed the dusk side of Venus in October 2017, and the dawn side in April-May 2018, and May 2019.

Gravity waves generated in the lower atmosphere and propagate to the thermosphere should affect the planetary-scale circulation via deposition of momentum. The present study suggests that such momentum deposition can change periodically in the course of the propagation of planetary-scale waves. The evaluation of the momentum transport and its variability is left for future study.

Chapter 4: A new cloud tracking method tolerant to streaky regions

4.1. Introduction

Cloud tracking has widely been used to estimate motions of clouds. By calculating cross-correlations between small areas in a pair of images obtained at a short time interval, the displacements within the time interval are estimated. In the studies of Venus' atmosphere, ultraviolet (UV) images which reflect the spatial distributions of unidentified absorbers (e.g. Rossow et al., 1980) have been mainly used for cloud tracking. UV cloud tracking is thought to be sensitive to atmospheric motions at the cloud top altitude of ~70 km. In this altitude region, the atmosphere is rotating ~60 times faster than the solid body. The generation and maintenance mechanism of the superrotation is still unknown.

The accuracy and the reliability of cloud tracking method have been improved over the decades. Kouyama et al. (2012) implemented the relaxation labeling method which allows selection of a reliable peak from multiple candidates on each cross-correlation surface assuming that wind velocities change smoothly in space. Ikegawa & Horinouchi (2016) developed a method to suppress false peaks on cross-correlation surfaces by the superposition of cross-correlation surfaces separated for image pairs with different time intervals.

Momentum transport associated with atmospheric waves is thought to be crucial for the maintenance of the superrotation (Read & Lebonnois, 2018). Rossow et al. (1990) investigated the momentum transport by the mean and eddy components using cloud-tracked velocities and showed that poleward transport of the superrotational angular momentum dominates, although the eddy component is variable. Limaye (2007) reproduced a structure of a thermal tide from dayside cloud-tracked wind velocities using UV images

obtained by Pioneer Venus Orbiter and showed that the equatorward transport of the superrotational momentum by the thermal tide.

Despite a number of studies on atmospheric waves with cloud tracking, they have been limited to low latitudes and thus the momentum transports by planetary-scale waves in the high latitudes has not been well-studied. This is because, in the high latitudes of Venus' cloud top, streaky features are predominant and the movements of clouds in the direction of streaks cannot be identified. Ikegawa & Horinouchi (2016) indicated the errors in the cloud-tracked wind velocities become large in the high latitude and reach 20 m s^{-1}. In the high latitudes of Venus cloud top, a large meridional shear exists associated with mid-latitude jets. Because such jets are dynamically unstable, the instabilities glow and atmospheric waves can be excited. It is thought that such atmospheric waves transport momentum equatorward and contribute to the acceleration of the atmosphere, forming the superrotation (e.g., Gierasch, 1975). However, this kind of instabilities and the atmospheric waves that transport momentum equatorward are yet to be observed. To solve this problem, I developed a new cloud-tracking method which can be applied to cloud images dominated by streaky features like UV images of the high latitudes of Venus. The proposed method enables investigation of the horizontal velocity field over a wide latitudinal range. Section 4.2 presents the details of the dataset and the new cloud-tracking method, Section 4.3 gives the results, Section 4.4 discusses the horizontal structure of a planetary-scale wave using cloud-tracked velocities, and Section 4.5 gives the conclusions.

4.2. Dataset and newly-developed method

4.2.1. Dataset

I used 365-nm channel images of UVI (Yamazaki et al. 2018) onboard Akatsuki (Nakamura et al. 2016), which are sensitive to the absorption by unidentified materials that absorb solar radiation at wavelengths from ultraviolet to violet (Moroz et al., 1985). Akatsuki is orbiting around Venus with the apocenter altitude of 370,000 km, and the pericenter altitude of ~7,000-18,000 km. UVI has the field of view is 12° × 12° and takes images of 1024 × 1024 pixels. The pixel resolution of UVI at the sub-spacecraft point is ~80 km at the pericenter. The images that are projected onto longitude-latitude maps with a grid interval of 0.125° both in latitude and longitude (Ogohara et al., 2017). The data analyzed were taken the period from

June 1, 2017 to August 31, 2017. In the cloud tracking, pairs of 3 images with a time interval of 2 hours were used.

4.2.2. Elimination of streak features

I developed a method to determine the orientation of streaks in a template region and eliminate the streak feature having the determined orientation from the template and a search region. The template is a small area in the first image where the velocity is estimated. The search region is an area in the second image where displacements of the template is searched. The idea is that the spatial differentiation of an image along the streak orientation eliminates streak features because the spatial variation associated with the streaks is small along this direction. The differentiation of the brightness I along a certain direction l is expressed as $\nabla I \cdot l$. The direction l can be determined by finding the minimum of the variance of $\nabla I \cdot l$. Figure 1 shows an example of the procedure of the proposed method. The red line in Figure 1a represents the streak orientation determined by the proposed method. Figures 1d and 1e show the differentiated template and search region along the determined orientation; streak features were successfully eliminated from these images and small-scale patchy features became predominant. Figures 1c and 1f show the cross-correlation surfaces without and with elimination of streak features, respectively, and distinct peaks appeared in Figure 1f.

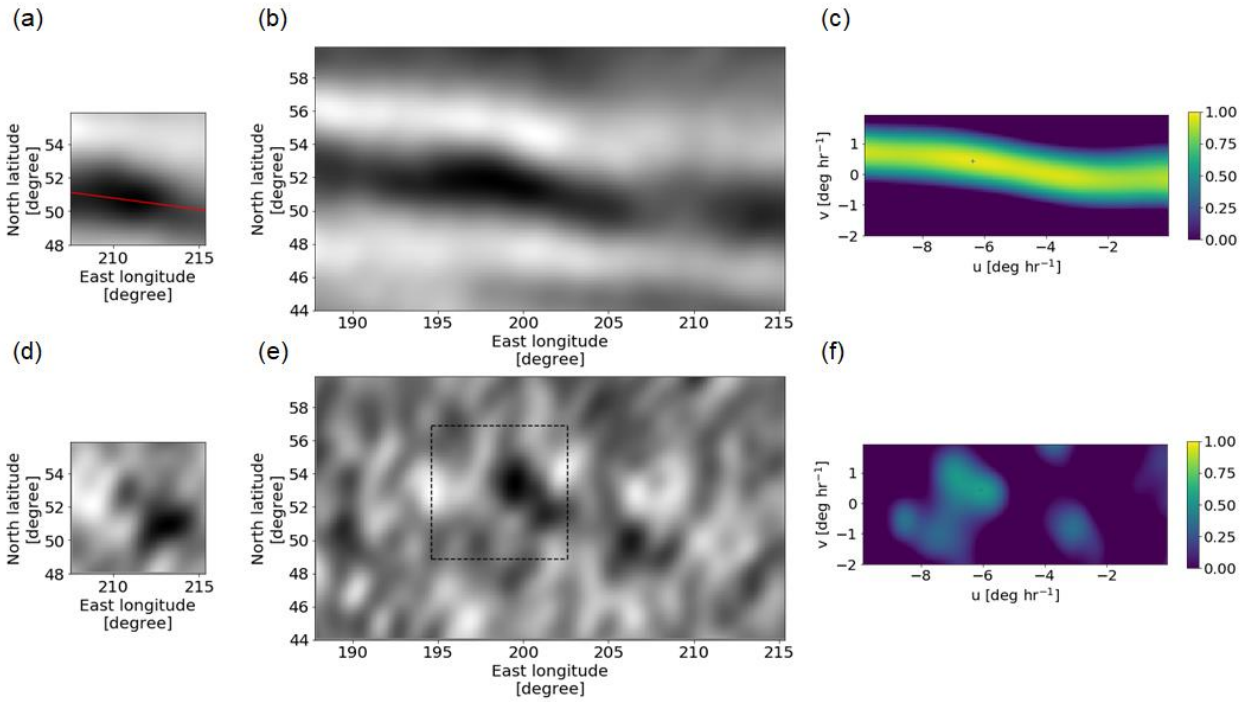

Figure 1. An example of the calculation of cross-correlation surfaces with and without elimination of streak features. Ultraviolet (365 nm) images of Venus taken by UVI on July 29, 2017 were used. A red line in panel (a) shows the orientation of streaks determined by the proposed method. Panels (d) and (e) were derived from (a) and (b), respectively, by differentiating along the determined orientation. Cross-correlation surface (c) is calculated using the template (a) and the search region (b). Cross-correlation surface (f) is calculated using the template (d) and the search region (e).

I applied this method to 365-nm images, combined with superposition of cross-correlation surfaces from different time intervals (Ikegawa & Horinouchi, 2016) and relaxation labeling (Kouyama et al, 2012) that suppress the effect of false peaks. The size of the template was set to 8° × 8° and the search region was determined assuming that the westward velocity is between 50 and 150 m s^{-1} and the meridional velocity is between -50 and 50 m s^{-1}. Velocities were obtained every 4° in both longitude and latitude. To obtain one velocity field, I used three images with a time interval of 2 hours: the cross-correlation surface between the first and the second images and that between the first and the third images were superposed. Figure 2 shows a snapshot of the velocity field superimposed on the high-pass filtered image. In this velocity field, the solid body rotation rate of 3 degrees per hour corresponding to the typical background superrotation speed was subtracted from each vector. Mid-latitude jets are clearly seen in the high latitudes. The wind

velocities whose errors are smaller than 5 m s^{-1} were used and the method of the error estimation is presented in Appendix A1.

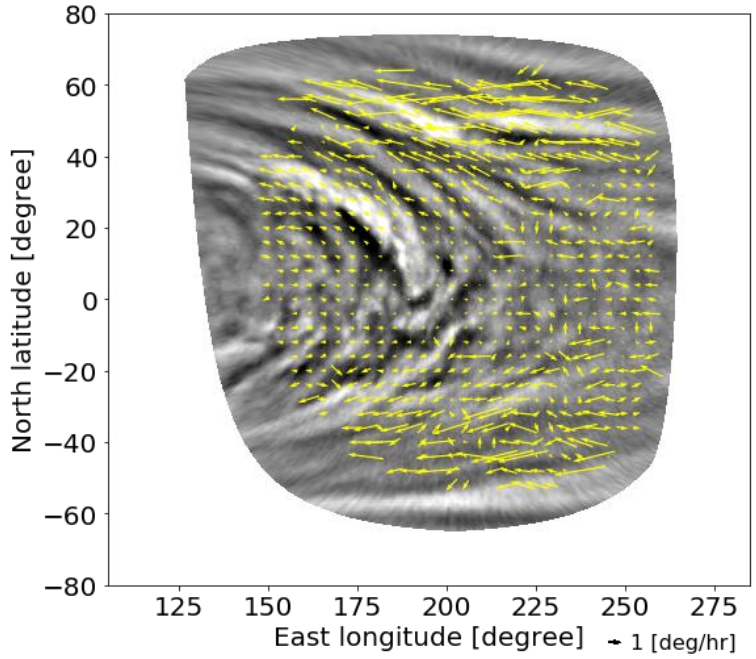

Figure 2. An example of the velocity field obtained from images taken on July 29, 2017 superimposed on the UV image. The zonal velocity in solid body rotation of 3 deg hr^{-1} was subtracted from each vector.

4.3. Results

Figure 3 shows the velocity field averaged in the local solar time and latitude coordinate. The analysis period was June to August 2017. The local solar time dependence is consistent with previous studies (Newman & Leovy, 1992): the zonal velocity is weak around noon and a poleward flow exist around the local solar time of ~14:00. The dayside-averaged zonal velocity corresponds to the atmospheric rotation period of 4.2 days on the equator.

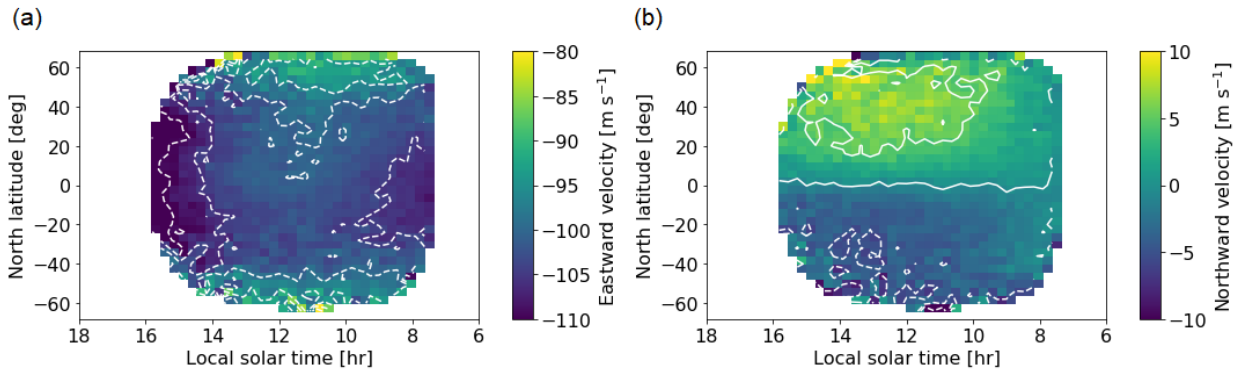

Figure 3. (a) Zonal and (b) meridional velocities averaged in the local solar time and latitude coordinate. Velocity fields are the averages in the period from June 1, 2017 to August 31, 2017.

By subtracting these solar-fixed components from all velocity vectors, the eddy components were extracted. Then I apply periodicity analysis to the time series of the eddy components at the local solar time of 12:00. Similar to Nara et al. (2019), I utilize all velocity measurements including those at local solar times other than 12:00; the time when the atmospheric region corresponding to each velocity vector has passed 12:00 was calculated on the assumption that the velocity field is advected at the dayside-mean zonal velocity. Figure 4 shows the obtained time series of the zonal velocity on the equator and the meridional velocity in the mid-latitude in July 2017. Periodical variations with periods of several days are seen in both of them. Figure 5 shows the latitudinal variations of the Lomb-Scargle periodograms (Scargle, 1982) of the eddy zonal and meridional components. Periodicities of ~4.9 days are predominant in the equatorial zonal velocity the and mid-latitude meridional velocity. Assuming that the zonal wavenumber is unity based on the previous studies on the global-scale brightness oscillation with a period of ~5 days (Del Genio & Rossow, 1990), this periodicity can be attributed to a Rossby wave assuming wavenumber of unity because the phase velocity is slower than the mean zonal velocity whose recurrence period is ~4.2 days on the equator and the meridional velocity has a notable amplitude in the mid-latitude.

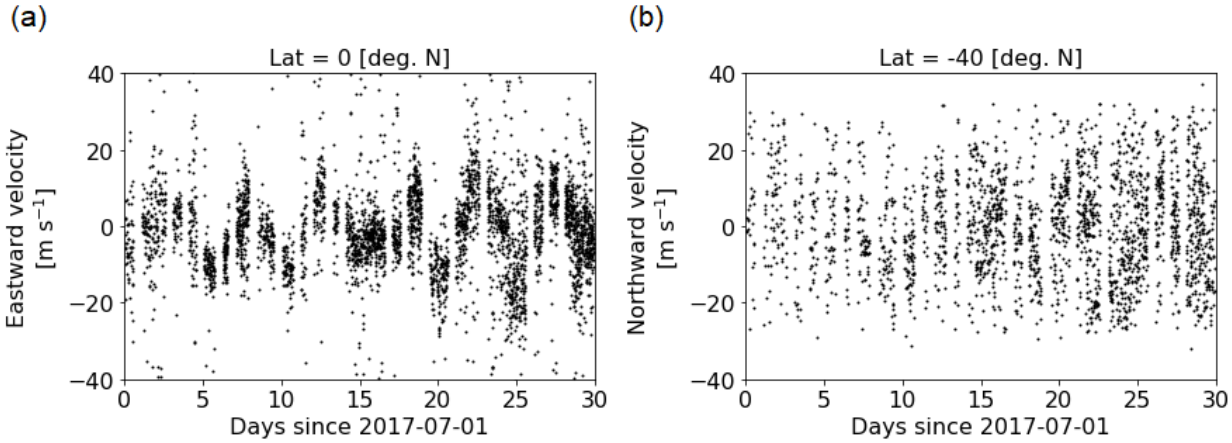

Figure 4. Time series of the eddy components of (a) the equatorial zonal velocity and (b) the meridional velocity at 40°S.

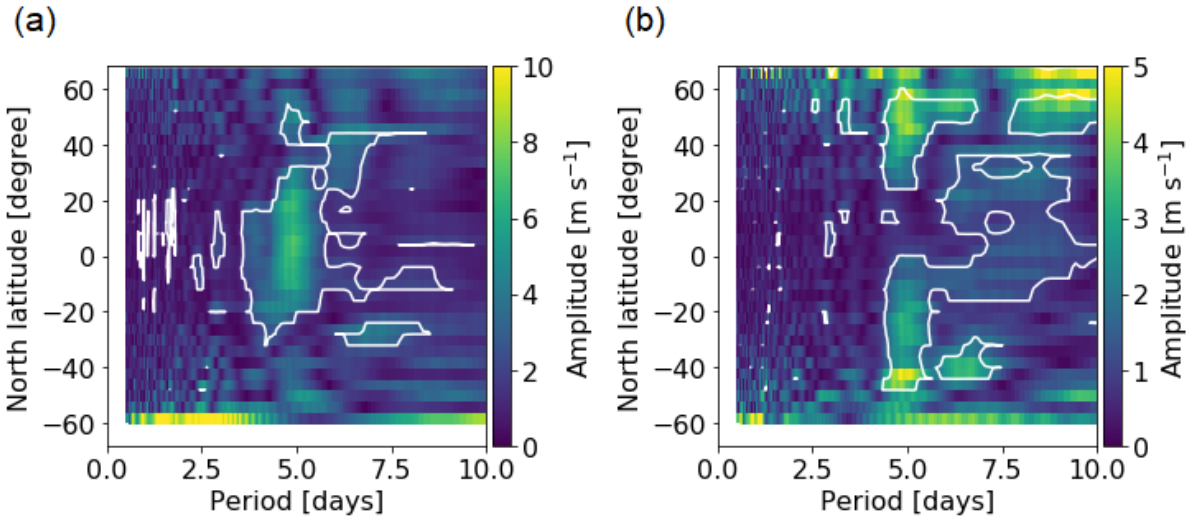

Figure 5. Latitudinal profiles of the periodograms of (a) the zonal and (b) the meridional velocities. White contours show the 99% statistical significance level.

4.4. Horizontal structure of the Rossby wave

Here I focus on the 4.9-day period component identified in the periodogram. By fitting a sinusoidal curve with a period of 4.9 days to the velocity time series at each latitude, the velocity field of the 4.9-day component was reproduced (Figure 6). The equatorially symmetric vortex patterns are highly consistent

with an equatorially-symmetric Rossby wave. Del Genio & Rossow (1990) also detected equatorially-symmetric periodicity in the UV brightness which is slower than the mean zonal velocity using images obtained by Pioneer Venus Orbiter. The meridional transport of the zonal momentum associated with the 4.9-day wave $\overline{u'v'}$, where *u'* and *v'* are the eastward and northward perturbation velocities, respectively, and the overbar denotes zonal average, is shown in Figure 7a. The positive (negative) momentum transport in the northern (southern) mid-latitude indicates convergence of superrotational momentum in the low latitude that can contribute to the maintenance of the superrotation, although the maximum momentum fluxes of ~5 m^2 s^{-2} are ~10 times smaller than the total eddy momentum flux in the opposite direction shown in Figure 7b. It should be noted that the total eddy momentum flux does not include the contribution of thermal tides that were subtracted as the local-time dependent component.

Imai et al. (2019) analyzed the same dataset to obtain velocities without eliminating streak features. The velocity fields they obtained are basically consistent with mine in terms of the mean zonal velocity and the periodicities in the eddy zonal and meridional components in the low and middle latitudes. In the spectral analysis, however, noise-like background component dominates in the zonal wind poleward of ~40° probably because of the difficulty in cloud tracking at high latitudes where streaky features dominate; my method extended the latitudinal coverage to ~60°, thereby revealing the wave structure and the momentum flux including the high latitudes

In the general circulation model by Sugimoto et al. (2014), Rossby waves appear around the cloud top level and transport superrotational momentum poleward, i.e. in the direction opposite to my analysis. On the other hand, Mitchell & Vallis (2010) showed, using idealized Earth-like general circulation models with slow planetary rotation (large Rossby number), that a global hemispherically-symmetric mode of zonal wavenumber one appears in the slow rotation case and transports superrotational momentum equatorward.

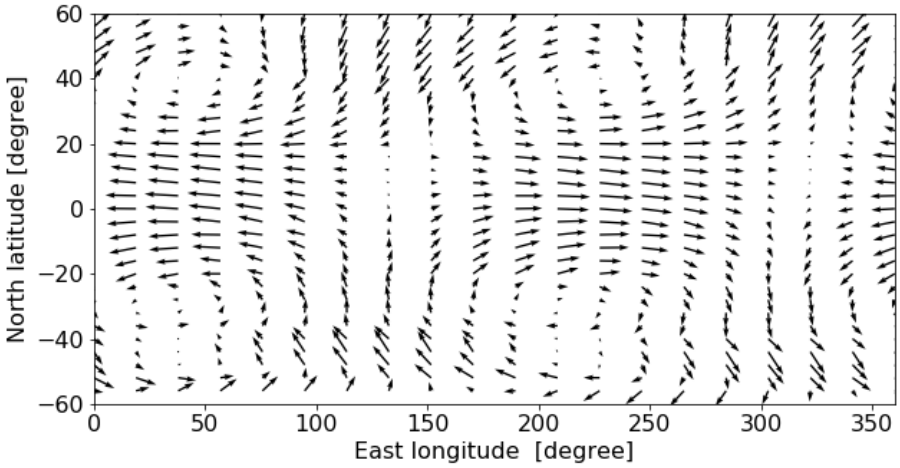

Figure 6. Horizontal structure of the velocity perturbation with a period of 4.9 days.

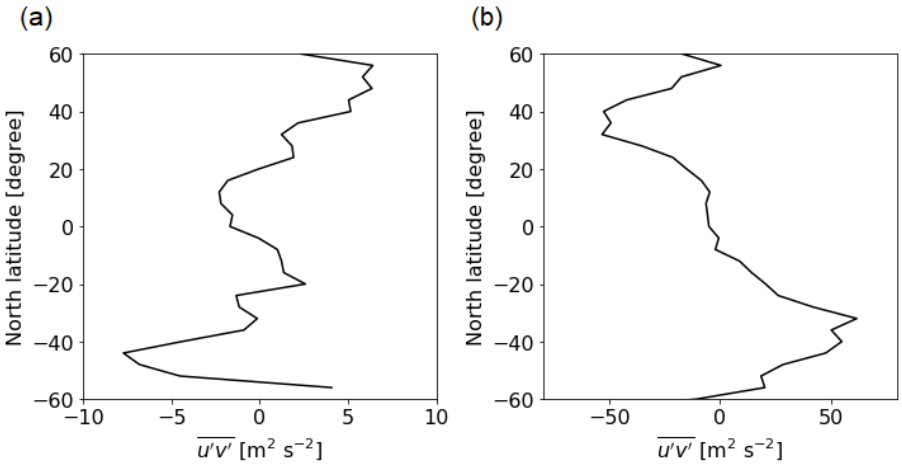

Figure 7. Momentum fluxes associated with (a) the 4.9-day wave and (b) the total eddy component except the solar-fixed (thermal tide) component.

4.5. Summary

I developed a new cloud tracking method which can be applied to cloud images dominated by streaky features such as the high latitudes of Venus. Differentiation of images along the streak orientation successfully removed the streak features and enhanced patchy features. As a result, distinct peaks appeared in the cross-correlation surfaces between image pairs, and velocity vectors were obtained also in the high latitude of Venus where the previous cloud-tracking studies did not cover reliably. Cloud tracking with the elimination of streak features is applicable not only to Venus but also to other planets such as Jupiter and Saturn, whose cloud images exhibit strip features.

The spectral analysis of the obtained velocity time series revealed the existence of a prominent periodicity of 4.9 days which can be attributed to a Rossby wave because the phase speed is slower than the mean zonal velocity and the meridional velocity has a notable amplitude in the mid-latitude. The vortex pattern reproduced by fitting a sinusoidal curve having a period of 4.9 days to the time series at each latitude is consistent with the spatial structure of a hemispherically-symmetric Rossby wave. This is the first time to obtain the entire structure of the planetary-scale Rossby wave.

The positive (negative) momentum transport by the 4.9-day wave in the northern (southern) mid-latitude indicates convergence of superrotational (westward) momentum in the low latitude that can contribute to the maintenance of the superrotation was detected. The opposite results are obtained by a general circulation model (Sugimoto et al., 2014).

Appendix

A1. Error estimation of the velocity vectors

In this section, an error estimation improved from that by Ikegawa & Horinouchi (2016) is presented. To estimate the error in the velocity vector, Ikegawa & Horinouchi (2016) considered the 90% confidence bounds of the correlation coefficient for each peak and determined the range of the displacement where the correlation is within the confidence bounds of the peak correlation; the width of this range is considered as the error in the peak position, which corresponds to the velocity error. In this section, the peak position is determined by fitting a Gaussian function to the cross-correlation. The errors in peak position, which corresponds to the errors in the velocity,

It is known that the inverse hyperbolic tangent of the correlation coefficient follows the normal standard distribution (Fisher, 1915; Thomson & Emery, 2014):

$$Z = \operatorname{arctanh} r \sim N\left(\eta, \frac{1}{M_e - 3}\right), \tag{A1}$$

where r is the correlation coefficient, $\eta = \operatorname{arctanh}\rho$, M_e is the effective degree of freedom of the template used for the calculation of r, and ρ is the population correlation coefficient (Thomson & Emery, 2014). The effective degree of freedom would be the number of pixels in the template if the brightness distribution is completely random and unity if the brightness is homogeneous. I used the same method of estimation of the effective degree of freedom same as Ikegawa & Horinouchi (2016). Figure A1 shows an example of the arctanh r with 1-σ errors.

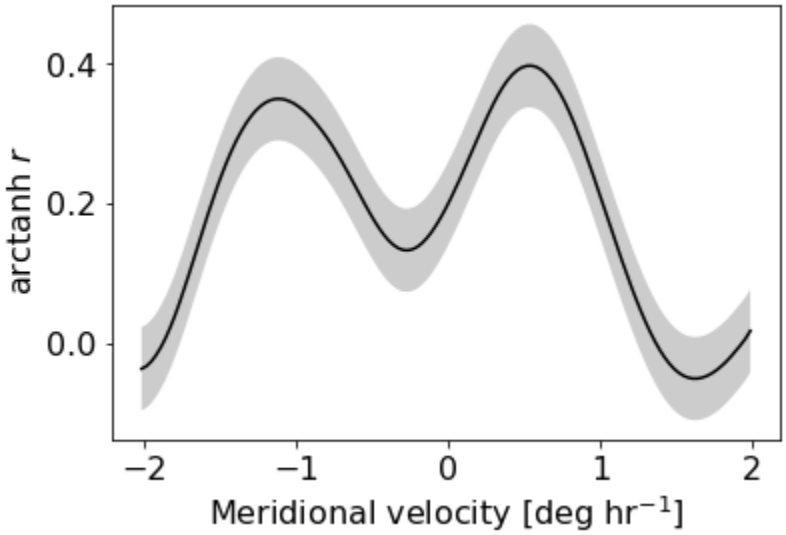

Figure A1. An example of the inverse hyperbolic tangent of the cross-correlation surface (black curve) along meridional displacement. The gray filled area indicates the 1-σ error.

Then, I approximate the converted cross-correlation surface arctanh[$r(x)$], where x is the longitudinal or latitudinal displacement. by a Gaussian function plus a linear function as:

$$Z(x) = a \exp\left(-\frac{1}{2}\frac{(x-b)^2}{c^2}\right) + dx + e, \tag{A4}$$

where a, b, c, d, and e are the fitting parameters to be determined by non-linear least squares fitting. Because the non-linear least square method optimizes the parameters by linearizing the model function at each iteration, the errors of the optimal parameters can be determined in the same way as the linear least square fitting. I can estimate the peak position of the cross-correlation surface b with its error σ_b. Figure A2 shows an example of the fitting of eq. (A2) to the cross-correlation surface. The fitting was conducted at the points in the vicinity of the peak (within 30 grids away from the peak position). The model function seems to be well fitted to the cross-correlation surface. The parameter representing the peak position, b, was estimated to be 0.58±0.09 degree hr^{-1}, which corresponds to a northward velocity of 17±3 m s^{-1}.

In the implementation of the error estimation, the error is assumed to be constant along the displacement and is set to the value at the peak position to reduce the calculation cost. This corresponds to the approximation that the effective degree of freedom of the template does not change with the displacement around the peak position. Actually, Figure A1 shows that the errors almost constant around the peak.

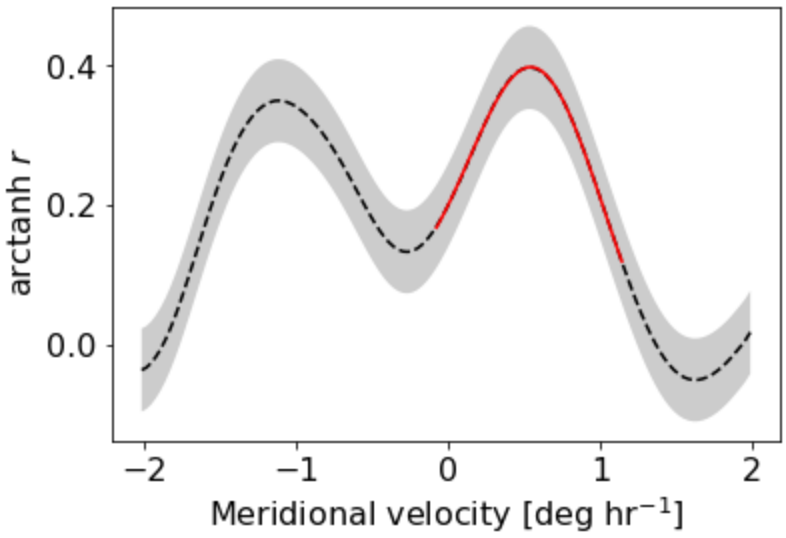

Figure A2. Same as Figure A1, but the red curve shows a function fitted to the black curve around the peak.

Figure A3 shows examples of the velocity error map. The estimated errors are relatively small (a few m s^{-1}) and almost independent of the latitude up to ~60°, implying a successful removal of streak features. The large errors near the eastern and southern edge of the velocity field are attributed to the low resolution of the images; around the edge, images are extended in the course of the projection onto the longitude-latitude coordinate.

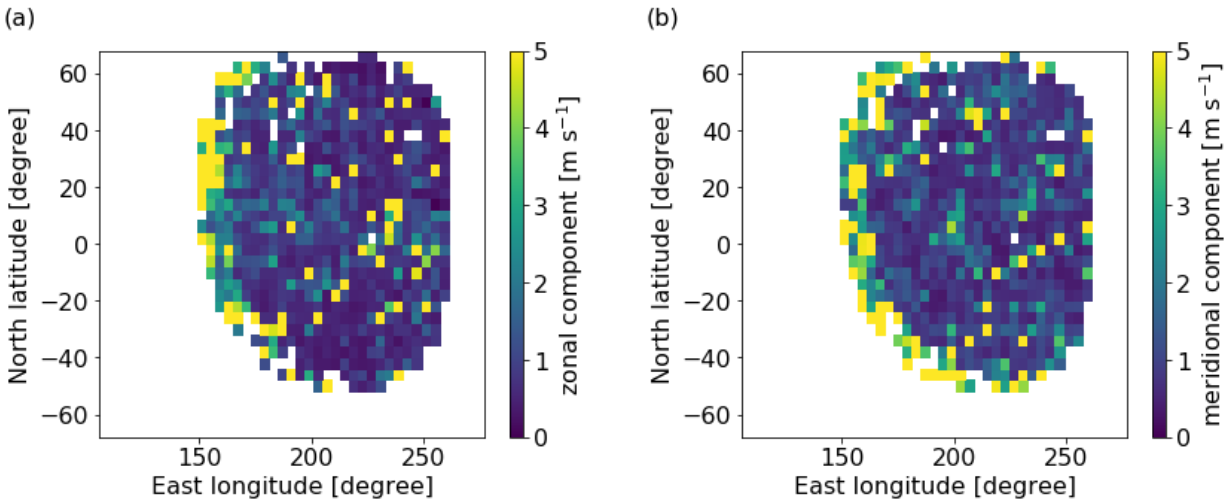

Figure A3. Estimated errors in (a) the zonal velocity filed and (b) the meridional velocity field. Data taken on July 29, 2017 were used.

Chapter 5: Summary

The properties of planetary-scale atmospheric waves at the cloud top of Venus were investigated with cloud tracking in this thesis.

In Chapter 2, by comparing the spatial and temporal variations of the UV brightness and cloud-tracked velocity obtained by VMC on board Venus Express, the formation mechanism of the planetary-scale cloud feature is discussed. It was suggested that the planetary-scale UV contrast is formed by the transport of UV absorbing materials by horizontally-propagating planetary-scale waves. Spectral analyses revealed a coherent periodicity of ~4 Earth days independent of the latitude in the UV brightness and ~4 and ~5 Earth day periodicities in the cloud-tracked velocities. The 4-day oscillation was attributed to a Kelvin wave because the phase speed is faster than the background zonal wind, the amplitude is large in the low latitude, and the velocity oscillation is predominantly zonal. The 5-day oscillation was attributed to a Rossby wave because the phase speed is slower than the background zonal wind and the amplitude of the meridional velocity is large in the middle latitude. Based on the observations above and a numerical experiment, it is suggested that the planetary-scale cloud feature called the horizontal "Y feature" is formed by the transport of the UV absorber by horizontally-propagating planetary-scale waves and the mean meridional circulation.

The UV-dark pattern studied here is related to the planetary albedo. Lee et al. (2019) revealed that the anti-correlation between the westward zonal wind and the planetary albedo at the ultraviolet wavelength by the analysis of the long-term data; when the planetary albedo is low, the equatorial zonal wind is fast. They pointed out that the increased solar heating may cause the acceleration of the zonal wind through cyclostrophic balance, enhanced thermal tide, or enhanced meridional circulation. It is also possible that such a variation of planetary-scale circulation is related to planetary-scale waves, which control the planetary albedo through the formation of planetary-scale Y feature. The long-term variations of the

planetary albedo and the activities of planetary-scale waves should be compared to investigate the coupling between dynamics and solar heating.

In Chapter 3, the vertical coupling between the cloud-level atmosphere and the thermosphere was investigated using the spectral data obtained by EXCEED on board an Earth-orbiting satellite Hisaki and the UV images obtained by UVI on board the Venus orbiter Akatsuki. The former probes airglow emission from the Venusian thermosphere and the latter probes the cloud top. By simultaneous observations of the dawn side of Venus by these instruments, a periodicity of 3.6 days was detected in the thermospheric O atom airglow intensity, the cloud-top UV brightness, and the cloud-top zonal velocity. A one-dimensional model revealed that the Kelvin wave cannot propagate from the cloud level to the thermosphere because of radiative damping. The modeling also revealed that small-scale gravity waves having wavelengths of ~1000 km can propagate to the thermosphere on the dawn side because of the fast vertical group velocity and that the waves are strongly attenuated on the dusk side. It is suggested that the periodical variation of the airglow intensity with a period of ~3.6 days might be caused by the periodical variation of the gravity wave flux that is driven by the influence of the Kelvin wave on the generation or transmission of the gravity waves. The gravity waves that reach the thermosphere will break to produce turbulence or induce large-scale circulation via momentum deposition. I further developed a one-dimensional photochemical model to investigate the response of the airglow intensity to the change of the vertical transport caused by gravity waves. The model showed that the variation of the diffusion coefficient with an amplitude of ~300 $m^2 s^{-1}$ explains the observed amplitude of the airglow intensity.

The momentum deposition by gravity waves in the thermosphere is expected to play crucial roles in the thermospheric circulation. Since the wave momentum deposition is related to the eddy diffusion induced by breaking of gravity waves (Holton, 1982), the analysis of O atom airglow, which is sensitive to the vertical diffusion, combined with a numerical modeling of a vertical wave propagation would confirm the scenario.

Radio occultation measurements can obtain vertical temperature profiles and detect wavy temperature fluctuation associated with gravity waves (Science et al., 2015; Tellmann et al., 2012). The frequencies and phase velocities should also be constrained by such observations and a numerical modeling with high resolution.

In Chapter 4, a new cloud tracking method which is applicable to cloud regions dominated by streaky features was developed and applied to images obtained by UVI on board Akatsuki. Using this method, reliable wind velocities were obtained including the high latitude of Venus where is dominated by streaky features. The spectral analysis of the cloud-tracked velocities obtained by the new method detected the periodicity of 4.9 days in both zonal and meridional components. The vortex pattern in the horizontal structure of the 4.9-day component is consistent with a Rossby wave. The equatorward transport of superrotational momentum by the Rossby wave was detected in the mid-latitude for the first time. The observation of the wind field over the entire cloud top of Venus including the high latitudes enables investigations of various topics, such as the development and decay of the instability of the mid-latitude jets, the excitation of waves by the instability and the associated momentum transport, and the material transport across the jets.

Anti-correlation between mean zonal wind and the planetary albedo was reported by Lee et al., (2019). There is a possibility that planetary-scale waves which control the planetary albedo would also control the mean wind variation. Propagation of small-scale gravity waves from the cloud-level atmosphere and the thermosphere implies the momentum transport between these two altitudes. A newly developed cloud tracking method enabled the estimation of wind velocity in the high latitude of Venus' cloud top. The atmospheric waves excited by shear instability, which have been thought to exist and transport superrotational momentum equatorward, are expected to be detected by the developed method. Combining the studies of spatial variation of solar heating and both horizontal and vertical momentum transports, the acceleration mechanism of the Venus' superrotation will be comprehensively discussed.

Acknowledgement

I would like to express my most gratitude to my supervisor Prof. Takeshi Imamura for taking me the cutting edge of Venus science and giving me plenty of teachings and advises. My five-year graduate student life was highly fulfilling.

Prof. Naomoto Iwagami, Prof. Ichiro Yoshikawa, and Dr. Kazuo Yoshioka gave me fruitful suggestions and comments in seminars of our research group. In addition to above persons, Assoc. Akira Ejiri and Dr. Yuki Izumida closely reviewed my thesis and gave me valuable comments and suggestions. Prof. Takehiko Satoh, Prof. Masato Nakamura, and the other Akatsuki team members for the fruitful discussion and advice during SWT meetings and conferences. The discussions of the latest Venus science encouraged me to study harder. Dr. Shin-ya Murakami, Dr. Toru Kouyama, Dr Yeon Joo Lee, and Dr. Pushkar Kopparla gave me a lot of valuable comments and suggestions on the studies using images of VMC and UVI. Dr. Go Murakami, Dr. Atsushi Yamazaki, Dr. Kei Masunaga also gave me a lot of advises about the data analysis of EXCEED spectra.

I have a lot of memories with Mr. Yushi Suto, Ms. Yumika Sakamoto, Mr. Masayuki Omino, Mr. Masahiro Shimokawa, Mr. Ryo Hasegawa, Mr. Yasuto Hoshi who I spent my master course student days together with. I also had a nice time with Mr. Takehiko Kitahara, Ms. Mayu Miyamoto, Minori Narita, Naoya Kajiwara, Ryota Mori, and Kiichi Fukuya, alumni and current students of Imamura laboratory. I am grateful to Ms. Reina Hikida, Mr. Fumiharu Suzuki, Mr. Kosuke Takami, and Mr. Ryoichi Koga for encouraging each other.

I also appreciate friends met in Monster Hunter Frontier, Mr. Redlimit, Mr. Soya, Mr. Mile, Mr. Kiji, Ms. Shellis, Mr. Exas, Mr. Idaten, Kurogami-san, Kurumi-san, Uranus-san, and Goma-chan. I spent precious times with them. I hope our friendship continues after the end of MHF. Mr. Yujin Tou gave me advises about any kinds of difficulties and spent time together since I was an elementary school student.

Finally, I would like to appreciate my family, who supported me regardless of time and place. My successful results could not be achieved without any of them.

Reference

Alexander, M. J. (1992). A mechanism for the Venus thermospheric superrotation. *Geophysical Research Letters*, *19*(22), 2207–2210. https://doi.org/10.1029/92GL02110

Banks, P. M., & Kockarts, G. (1973). Aeronomy, vol. B, chap. 15.

Boyer, C., & Guérin, P. (1969). Etude de la rotation rétrograde, en 4 jours, de la couche extérieure nuageuse de Vénus. *Icarus*, *11*(3), 338–355. https://doi.org/10.1016/0019-1035(69)90067-0

Chaffin, M. S., Deighan, J., Schneider, N. M., & Stewart, A. I. F. (2017). Elevated atmospheric escape of atomic hydrogen from Mars induced by high-Altitude water. *Nature Geoscience*, *10*(3), 174–178. https://doi.org/10.1038/ngeo2887

Chapman, S., & Cowling, T. G. (1970). *The Mathematical Theory of Non-Uniform Gases, Cambridge Univ*. England: Press, Cambridge.

Clancy, R. T., Sandor, B. J., & Moriarty-Schieven, G. (2012). Circulation of the Venus upper mesosphere/lower thermosphere: Doppler wind measurements from 2001-2009 inferior conjunction, sub-millimeter CO absorption line observations. *Icarus*, *217*(2), 794–812. https://doi.org/10.1016/j.icarus.2011.05.021

Clancy, R. T., Sandor, B. J., & Hoge, J. (2015). Doppler winds mapped around the lower thermospheric terminator of Venus: 2012 solar transit observations from the James Clerk Maxwell Telescope. *Icarus*, *254*, 233–258. https://doi.org/10.1016/j.icarus.2015.03.031

Covey, C., & Schubert, G. (1981). 4-Day waves in the Venus atmosphere. *Icarus*, *47*(1), 130–138. https://doi.org/10.1016/0019-1035(81)90097-X

Crisp, D. (1989). Radiative forcing of the Venus mesosphere. II. Thermal fluxes, cooling rates, and radiative equilibrium temperatures. *Icarus*, *77*(2), 391–413. https://doi.org/10.1016/0019-1035(89)90096-1

Dias Pinto, J. R., & Mitchell, J. L. (2014). Atmospheric superrotation in an idealized GCM: Parameter dependence of the eddy response. *Icarus*, *238*, 93–109. https://doi.org/10.1016/j.icarus.2014.04.036

Eckermann, S. D., Ma, J., & Zhu, X. (2011). Scale-dependent infrared radiative damping rates on Mars and their

role in the deposition of gravity-wave momentum flux. *Icarus*, *211*(1), 429–442. https://doi.org/10.1016/j.icarus.2010.10.029

Esposito, L. W. (1980). Ultraviolet contrasts and the absorbers near the Venus cloud tops. *Journal of Geophysical Research*, *85*(A13), 8151. https://doi.org/10.1029/JA085iA13p08151

Fisher, R. A. (1915). Frequency Distribution of the Values of the Correlation Coefficient in Samples from an Indefinitely Large Population. *Biometrika*, *10*(4), 507. https://doi.org/10.2307/2331838

Fox, J. L., & Bougher, S. W. (1991). Structure, Luminosity, and Dynamics of the Venus Thermosphere. In *Venus Aeronomy* (pp. 357–489). Dordrecht: Springer.

Del Genio, A. D., & Rossow, W. B. (1982). Temporal variability of ultraviolet cloud features in the Venus stratosphere. *Icarus*, *51*(2), 391–415. https://doi.org/10.1016/0019-1035(82)90091-4

Del Genio, A. D., & Rossow, W. B. (1990). Planetary-Scale Waves and the Cyclic Nature of Cloud Top Dynamics on Venus. *Journal of the Atmospheric Sciences*, *47*(3), 293–318. https://doi.org/10.1175/1520-0469(1990)047<0293:PSWATC>2.0.CO;2

Gierasch, P. J. (1975). Meridional Circulation and the Maintenance of the Venus Atmospheric Rotation. *Journal of the Atmospheric Sciences*. https://doi.org/10.1175/1520-0469(1975)032<1038:MCATMO>2.0.CO;2

Gilli, G., Lebonnois, S., González-Galindo, F., López-Valverde, M. A., Stolzenbach, A., Lefèvre, F., et al. (2017). Thermal structure of the upper atmosphere of Venus simulated by a ground-to-thermosphere GCM. *Icarus*, *281*, 55–72. https://doi.org/10.1016/j.icarus.2016.09.016

Hinson, D. P., & Jenkins, J. M. (1995). Magellan radio occultation measurements of atmospheric waves on venus. *Icarus*. https://doi.org/10.1006/icar.1995.1064

Holton, J. R. (1982). The role of gravity wave induced drag and diffusion in the momentum budget of the mesosphere. *Journal of the Atmospheric Sciences*. https://doi.org/10.1175/1520-0469(1982)039<0791:TROGWI>2.0.CO;2

Holton, James R, Haynes, P. H., McIntyre, M. E., Douglass, A. R., Rood, R. B., & Pfister, L. (1995). Stratosphere-troposphere exchange. *Reviews of Geophysics*, *33*(4), 403. https://doi.org/10.1029/95RG02097

Hoshino, N., Fujiwara, H., Takagi, M., Takahashi, Y., & Kasaba, Y. (2012). Characteristics of planetary-scale waves simulated by a new venusian mesosphere and thermosphere general circulation model. *Icarus*, *217*(2), 818–830. https://doi.org/10.1016/j.icarus.2011.06.039

Hueso, R., Peralta, J., Garate-Lopez, I., Bandos, T. V., & Sánchez-Lavega, A. (2015). Six years of Venus winds

at the upper cloud level from UV, visible and near infrared observations from VIRTIS on Venus Express. *Planetary and Space Science*, *113–114*, 78–99. https://doi.org/10.1016/j.pss.2014.12.010

Iga, S., & Matsuda, Y. (2005). Shear Instability in a Shallow Water Model with Implications for the Venus Atmosphere. *Journal of the Atmospheric Sciences*, *62*(7), 2514–2527. https://doi.org/10.1175/jas3484.1

Ikegawa, S., & Horinouchi, T. (2016). Improved automatic estimation of winds at the cloud top of Venus using superposition of cross-correlation surfaces. *Icarus*, *271*, 98–119. https://doi.org/10.1016/j.icarus.2016.01.018

Imai, M., Kouyama, T., Takahashi, Y., Yamazaki, A., Watanabe, S., Yamada, M., et al. (2019). Planetary-Scale Variations in Winds and UV Brightness at the Venusian Cloud Top: Periodicity and Temporal Evolution. *Journal of Geophysical Research: Planets*, (Vmc), 1–25. https://doi.org/10.1029/2019JE006065

Imamura, T. (2006). Meridional propagation of planetary-scale waves in vertical shear: Implication for the Venus atmosphere. *Journal of the Atmospheric Sciences*, *63*(6), 1623–1636. https://doi.org/10.1175/JAS3684.1

Imamura, T., Higuchi, T., Maejima, Y., Takagi, M., Sugimoto, N., Ikeda, K., & Ando, H. (2014). Inverse insolation dependence of Venus' cloud-level convection. *Icarus*, *228*, 181–188. https://doi.org/10.1016/j.icarus.2013.10.012

Keating, G. M., Bertaux, J. L., Bougher, S. W., Cravens, T. E., Dickinson, R. E., Hedin, A. E., et al. (1985). Chapter Iv Models of Venus Neutral Upper Atmosphere : Structure and Composition. *Advances in Space Research*, *5*(11), 117–171.

Khatuntsev, I. V., Patsaeva, M. V., Titov, D. V., Ignatiev, N. I., Turin, A. V., Limaye, S. S., et al. (2013). Cloud level winds from the Venus Express Monitoring Camera imaging. *Icarus*, *226*(1), 140–158. https://doi.org/10.1016/j.icarus.2013.05.018

Kouyama, T., Imamura, T., Nakamura, M., Satoh, T., & Futaana, Y. (2012). Horizontal structure of planetary-scale waves at the cloud top of Venus deduced from Galileo SSI images with an improved cloud-tracking technique. *Planetary and Space Science*, *60*(1), 207–216. https://doi.org/10.1016/j.pss.2011.08.008

Kouyama, T., Yamazaki, A., Yamada, M., & Imamura, T. (2013). A method to estimate optical distortion using planetary images. *Planetary and Space Science*, *86*, 86–90. https://doi.org/10.1016/j.pss.2013.06.027

Kouyama, T., Imamura, T., Nakamura, M., Satoh, T., & Futaana, Y. (2013). Long-term variation in the cloud-tracked zonal velocities at the cloud top of Venus deduced from Venus Express VMC images. *Journal of Geophysical Research E: Planets*, *118*(1), 37–46. https://doi.org/10.1029/2011JE004013

Kouyama, T., Imamura, T., Nakamura, M., Satoh, T., & Futaana, Y. (2015). Vertical propagation of planetary-scale waves in variable background winds in the upper cloud region of Venus. *Icarus, 248*, 560–568. https://doi.org/10.1016/j.icarus.2014.07.011

Lee, Y. J., Imamura, T., Schröder, S. E., & Marcq, E. (2015). Long-term variations of the UV contrast on Venus observed by the Venus Monitoring Camera on board Venus Express. *Icarus, 253*, 1–15. https://doi.org/10.1016/j.icarus.2015.02.015

Lee, Y. J., Yamazaki, A., Imamura, T., Yamada, M., Watanabe, S., Sato, T. M., et al. (2017). Scattering Properties of the Venusian Clouds Observed by the UV Imager on board Akatsuki. *The Astronomical Journal*, *154*(2), 44. https://doi.org/10.3847/1538-3881/aa78a5

Lee, Yeon Joo, Jessup, K.-L., Perez-Hoyos, S., Titov, D. V., Lebonnois, S., Peralta, J., et al. (2019). Long-term Variations of Venus's 365 nm Albedo Observed by Venus Express, Akatsuki, MESSENGER, and the Hubble Space Telescope. *The Astronomical Journal*, *158*(3), 126. https://doi.org/10.3847/1538-3881/ab3120

Lefèvre, M., Spiga, A., & Lebonnois, S. (2017). Three-dimensional turbulence-resolving modeling of the Venusian cloud layer and induced gravity waves. *Journal of Geophysical Research: Planets*, *122*(1), 134–149. https://doi.org/10.1002/2016JE005146

Limaye, S. (1988). Venus : Cloud Cloud during 1982 as Determined Images from Pioneer Photopolarimeter, *226*, 212–226.

Limaye, Sanjay, & Suomi, V. (1977). A Normalized View of Venus. *Journal of the Atmospheric Sciences*, *34*(1), 205–215. https://doi.org/10.1175/1520-0469(1977)034<0205:ANVOV>2.0.CO;2

Limaye, Sanjay S., Markiewicz, W. J., Krauss, R., Ignatiev, N., Roatsch, T., & Matz, K. D. (2015). Focal lengths of Venus Monitoring Camera from limb locations. *Planetary and Space Science*, *113–114*, 169–183. https://doi.org/10.1016/j.pss.2015.01.010

Limaye, Sanjay Shridhar. (2007). Venus atmospheric circulation: Known and unknown. *Journal of Geophysical Research*, *112*(E4), E04S09. https://doi.org/10.1029/2006JE002814

Limaye, Sanjay Shridhar, & Suomi, V. E. (1981). Cloud Motions on Venus: Global Structure and Organization. *Journal of the Atmospheric Sciences*, *38*(6), 1220–1235. https://doi.org/10.1175/1520-0469(1981)038<1220:CMOVGS>2.0.CO;2

Markiewicz, W. J., Titov, D. V., Limaye, S. S., Keller, H. U., Ignatiev, N., Jaumann, R., et al. (2007). Morphology and dynamics of the upper cloud layer of Venus. *Nature*, *450*(7170), 633–636.

https://doi.org/10.1038/nature06320

Markiewicz, W. J., Titov, D. V., Ignatiev, N., Keller, H. U., Crisp, D., Limaye, S. S., et al. (2007). Venus Monitoring Camera for Venus Express. *Planetary and Space Science*, *55*(12), 1701–1711. https://doi.org/10.1016/j.pss.2007.01.004

Markiewicz, W. J., Petrova, E., Shalygina, O., Almeida, M., Titov, D. V., Limaye, S. S., et al. (2014). Glory on Venus cloud tops and the unknown UV absorber. *Icarus*, *234*, 200–203. https://doi.org/10.1016/j.icarus.2014.01.030

Masunaga, K., Seki, K., Terada, N., Tsuchiya, F., Kimura, T., Yoshioka, K., et al. (2015). Periodic variations of oxygen EUV dayglow in the upper atmosphere of Venus: Hisaki/EXCEED observations. *Journal of Geophysical Research: Planets*, *120*(12), 2037–2052. https://doi.org/10.1002/2015JE004849

Masunaga, K., Seki, K., Terada, N., Tsuchiya, F., Kimura, T., Yoshioka, K., et al. (2017). Dawn-dusk difference of periodic oxygen EUV dayglow variations at Venus observed by Hisaki. *Icarus*, *292*, 102–110. https://doi.org/10.1016/j.icarus.2016.12.027

Matsuno, T. (1966). Quasi-Geostrophic Motions in the Equatorial Area. *Journal of the Meteorological Society of Japan. Ser. II*, *44*(1), 25–43. https://doi.org/10.2151/jmsj1965.44.1_25

Mayr, H. G., Harris, I., Stevens-Rayburn, D. R., Niemann, H. B., Taylor, H. A., & Hartle, R. E. (1985). On the diurnal variations in the temperature and composition: a three-dimensional model with superrotation. *Advances in Space Research*, *5*(9), 109–112. https://doi.org/10.1016/0273-1177(85)90277-7

Mills, F. P., Esposito, L. W., & Yung, Y. L. (2007). Atmospheric composition, chemistry, and clouds. *Geophysical Monograph Series*, *176*, 73–100. https://doi.org/10.1029/176GM06

Minnaert, M. (1941). The Reciprocity Principle in Lunar Photometry. *Astrophysical Journal*, *93*, 403–410.

Mitchell, J. L., & Vallis, G. K. (2010). The transition to superrotation in terrestrial atmospheres. *Journal of Geophysical Research E: Planets*, *115*(12), 1–17. https://doi.org/10.1029/2010JE003587

Moroz, V. I., Ekonomov, A. P., Moshkin, B. E., Revercomb, H. E., Sromovsky, L. A., Schofield, J. T., et al. (1985). Solar and thermal radiation in the Venus atmosphere. *Advances in Space Research*, *5*(11), 197–232. https://doi.org/10.1016/0273-1177(85)90202-9

Nakamura, M., Imamura, T., Ueno, M., Iwagami, N., Satoh, T., Watanabe, S., et al. (2007). Planet-C: Venus Climate Orbiter mission of Japan. *Planetary and Space Science*, *55*(12), 1831–1842. https://doi.org/10.1016/j.pss.2007.01.009

Nakamura, M., Imamura, T., Ishii, N., Abe, T., Kawakatsu, Y., Hirose, C., et al. (2016). AKATSUKI returns to

Venus. *Earth, Planets and Space*, *68*(1). https://doi.org/10.1186/s40623-016-0457-6

Nakamura, M., Ishii, N., Imamura, T., Satoh, T., Abe, T., Hirose, C., et al. (2016). The first Japan's planetary orbiter AKATSUKI and its scientific results. In *Proceedings of the International Astronautical Congress, IAC*.

Nara, Y., Yoshikawa, I., Yoshioka, K., Murakami, G., Kimura, T., Yamazaki, A., et al. (2018). Extreme ultraviolet spectra of Venusian airglow observed by EXCEED. *Icarus*, *307*, 207–215. https://doi.org/10.1016/j.icarus.2017.10.028

Nara, Y., Imamura, T., Murakami, S., Kouyama, T., Ogohara, K., Yamada, M., et al. (2019). Formation of the Y Feature at the Venusian Cloud Top by Planetary-Scale Waves and the Mean Circulation: Analysis of Venus Express VMC Images. *Journal of Geophysical Research: Planets*, *124*(5), 1143–1156. https://doi.org/10.1029/2018JE005779

Newman, M., & Leovy, C. (1992). Maintenance of Strong Rotational Winds in Venus' Middle Atmosphere by Thermal Tides. *Science*, *257*(5070), 647–650. https://doi.org/10.1126/science.257.5070.647

Niemann, H. B., Kasprzak, W. T., Hedin, A. E., Hunten, D. M., & Spencer, N. W. (1980). Mass spectrometric measurements of the neutral gas composition of the thermosphere and exosphere of Venus. *Journal of Geophysical Research*, *85*(A13), 7817. https://doi.org/10.1029/ja085ia13p07817

Ogohara, K., Kouyama, T., Yamamoto, H., Sato, N., Takagi, M., & Imamura, T. (2012). Automated cloud tracking system for the Akatsuki Venus Climate Orbiter data. *Icarus*, *217*(2), 661–668. https://doi.org/10.1016/j.icarus.2011.05.017

Ogohara, K., Takagi, M., Murakami, S. ya, Horinouchi, T., Yamada, M., Kouyama, T., et al. (2017). Overview of Akatsuki data products: definition of data levels, method and accuracy of geometric correction. *Earth, Planets and Space*, *69*(1). https://doi.org/10.1186/s40623-017-0749-5

Patsaeva, M. V., Khatuntsev, I. V., Patsaev, D. V., Titov, D. V., Ignatiev, N. I., Markiewicz, W. J., & Rodin, A. V. (2015). The relationship between mesoscale circulation and cloud morphology at the upper cloud level of Venus from VMC/Venus Express. *Planetary and Space Science*, *113–114*, 100–108. https://doi.org/10.1016/j.pss.2015.01.013

Peralta, J., Hueso, R., & Sánchez-Lavega, A. (2007). A reanalysis of Venus winds at two cloud levels from Galileo SSI images. *Icarus*, *190*(2), 469–477. https://doi.org/10.1016/j.icarus.2007.03.028

Peralta, J., Sánchez-Lavega, A., Lõpez-Valverde, M. A., Luz, D., & MacHado, P. (2015). Venus's major cloud feature as an equatorially trapped wave distorted by the wind. *Geophysical Research Letters*, *42*(3), 705–

711. https://doi.org/10.1002/2014GL062280

Petrova, E. V., Shalygina, O. S., & Markiewicz, W. J. (2015). UV contrasts and microphysical properties of the upper clouds of Venus from the UV and NIR VMC/VEx images. *Icarus*, *260*, 190–204. https://doi.org/10.1016/j.icarus.2015.07.015

Read, P. L., & Lebonnois, S. (2018). Superrotation on Venus, on Titan, and Elsewhere. *Annual Review of Earth and Planetary Sciences*, *46*(1), 175–202. https://doi.org/10.1146/annurev-earth-082517-010137

Rossow, W. B., Del Genio, A. D., Limaye, S. S., Travis, L. D., & Stone, P. H. (1980). Cloud morphology and motions from Pioneer Venus images. *Journal of Geophysical Research*, *85*(A13), 8107. https://doi.org/10.1029/JA085iA13p08107

Rossow, W. B., Genio, A. D. Del, & Eichler, T. (1990). Cloud-Tracked Winds from Pioneer Venus OCPP Images. *Journal of the Atmospheric Sciences*, *47*(17), 2053–2084.

Sánchez-Lavega, A., Lebonnois, S., Imamura, T., Read, P., & Luz, D. (2017). The Atmospheric Dynamics of Venus. *Space Science Reviews*, *212*(3–4), 1541–1616. https://doi.org/10.1007/s11214-017-0389-x

Scargle, J. D. (1982). Studies in Astromonomical Tiem Series Analysis. II. Statistical Aspects of Spectral Analysis of Unevenly Spaced Data. *The Astronomical Journal*, *263*, 835–853.

Schubert, G., Covey, C., Genio, A. Del, Elson, L. S., Keating, G., Seiff, A., et al. (1980). Structure and circulation of the Venus atmosphere. *Journal of Geophysical Research*, *85*(A13), 8007. https://doi.org/10.1029/JA085iA13p08007

Science, A., Agency, E., & Planetenforschung, A. (2015). Vertical Wavenumber Spectra of Gravity Waves in the Venus Atmosphere Obtained from Venus Express Radio Occultation Data : Evidence for Saturation, (1987), 2318–2329. https://doi.org/10.1175/JAS-D-14-0315.1

Seiff, A., Schofield, J. T., Kliore, A. J., Taylor, F. W., Limaye, S. S., Revercomb, H. E., et al. (1985). Models of the structure of the atmosphere of Venus from the surface to 100 kilometers altitude. *Advances in Space Research*, *5*(11), 3–58. https://doi.org/10.1016/0273-1177(85)90197-8

Smith, M. D., & Gierasch, P. J. (1996). Global-scale winds at the Venus cloud-top inferred from cloud streak orientations. *Icarus*, *123*(2), 313–323. https://doi.org/10.1006/icar.1996.0160

Smith, M. D., Gierasch, P. J., & Schinder, P. J. (1993). Global-Scale Waves in the Venus Atmosphere. *Journal of the Atmospheric Sciences*, *50*(24), 4080–4096. https://doi.org/10.1175/1520-0469(1993)050<4080:GSWITV>2.0.CO;2

Sugimoto, N., Takagi, M., & Matsuda, Y. (2014). Waves in a Venus general circulation model. *Geophysical*

Research Letters, *41*(21), 7461–7467. https://doi.org/10.1002/2014GL061807

Svedhem, H., Titov, D. V., McCoy, D., Lebreton, J. P., Barabash, S., Bertaux, J. L., et al. (2007). Venus Express-The first European mission to Venus. *Planetary and Space Science*, *55*(12), 1636–1652. https://doi.org/10.1016/j.pss.2007.01.013

Takagi, M., Sugimoto, N., Ando, H., & Matsuda, Y. (2018). Three-Dimensional Structures of Thermal Tides Simulated by a Venus GCM. *Journal of Geophysical Research: Planets*, *123*(2), 335–352. https://doi.org/10.1002/2017JE005449

Tellmann, S., Häusler, B., Hinson, D. P., Tyler, G. L., Andert, T. P., Bird, M. K., et al. (2012). Small-scale temperature fluctuations seen by the VeRa Radio Science Experiment on Venus Express. *Icarus*, *221*(2), 471–480. https://doi.org/10.1016/j.icarus.2012.08.023

Thomson, R. E., & Emery, W. J. (2014). *Data Analysis Methods in Physical Oceanography*. Elsevier. https://doi.org/10.1016/C2010-0-66362-0

Titov, D. V., Markiewicz, W. J., Ignatiev, N. I., Song, L., Limaye, S. S., Sanchez-Lavega, A., et al. (2012). Morphology of the cloud tops as observed by the Venus Express Monitoring Camera. *Icarus*, *217*(2), 682–701. https://doi.org/10.1016/j.icarus.2011.06.020

VMC-MPAE-RP-SS011-001. (2008). *FS Calibration and Performance Report*.

Yamamoto, M., & Tanaka, H. (1997). Formation and maintenance of the 4-day circulation in the venus middle atmosphere. *Journal of the Atmospheric Sciences*, *54*(11), 1472–1489. https://doi.org/10.1175/1520-0469(1997)054<1472:FAMOTD>2.0.CO;2

Yamazaki, A., Tsuchiya, F., Sakanoi, T., Uemizu, K., Yoshioka, K., Murakami, G., et al. (2014). Field-of-View Guiding Camera on the HISAKI (SPRINT-A) Satellite. *Space Science Reviews*, *184*(1–4), 259–274. https://doi.org/10.1007/s11214-014-0106-y

Yamazaki, A., Yamada, M., Lee, Y. J., Watanabe, S., Horinouchi, T., Murakami, S. ya, et al. (2018). Ultraviolet imager on Venus orbiter Akatsuki and its initial results. *Earth, Planets and Space*, *70*(1). https://doi.org/10.1186/s40623-017-0772-6

Yoshikawa, I., Yoshioka, K., Murakami, G., Yamazaki, A., Tsuchiya, F., Kagitani, M., et al. (2014). Extreme Ultraviolet Radiation Measurement for Planetary Atmospheres/Magnetospheres from the Earth-Orbiting Spacecraft (Extreme Ultraviolet Spectroscope for Exospheric Dynamics: EXCEED). *Space Science Reviews*, *184*(1–4), 237–258. https://doi.org/10.1007/s11214-014-0077-z

Yoshioka, K., Murakami, G., Yamazaki, A., Tsuchiya, F., Kagitani, M., Sakanoi, T., et al. (2013). The extreme

ultraviolet spectroscope for planetary science, EXCEED. *Planetary and Space Science*, *85*, 250–260. https://doi.org/10.1016/j.pss.2013.06.021

Von Zahn, U., Fricke, K. H., Hunten, D. M., Krankowsky, D., Mauersberger, K., & Nier, A. O. (1980). The upper atmosphere of Venus during morning conditions. *Journal of Geophysical Research*, *85*(A13), 7829–7840. https://doi.org/10.1029/ja085ia13p07829

Von Zahn, U., Kumar, S., Niemann, H., & Prinn, R. (1983). 13. COMPOSITION OF THE VENUS ATMOSPHERE. In *Venus* (p. 299).

Zhang, S., Bougher, S. W., & Alexander, M. J. (1996). The impact of gravity waves on the Venus thermosphere and O2 IR nightglow. *Journal of Geophysical Research E: Planets*, *101*(E10), 23195–23205. https://doi.org/10.1029/96JE02035